2018

Characterization Of Somatosensation In The Brainstem And The Development Of A Sensory Neuroprosthesis

Srihari Yohan Sritharan
University of Pennsylvania, sri.gradresearch@gmail.com

Characterization Of Somatosensation In The Brainstem And The Development Of A Sensory Neuroprosthesis

Abstract
Innovations in neuroprosthetics have restored sensorimotor function to paralysis patients and amputees. However, to date there is a lack of solutions available to adequately address the needs of spinal cord injury patients (SCI). In this dissertation we develop a novel sensor-brain interface (SBI) that delivers electric microstimulation to the cuneate nucleus (CN) to restore somatosensory feedback in patients with intact limbs. In Chapter II, we develop a fully passive liquid metal antenna using gallium-indium (GaIn) alloy injected in polydimethylsiloxane (PDM) channels to measure forces within the physiological sensitivity of a human fingertip. In Chapter III, we present the first chronic neural interface with the CN in primates to provide access to long-term unit recordings and stimulation. In Chapter IV, we demonstrate that microstimulation to the CN is detectable in a Three Alternative Force Choice Oddity task in awake behaving primates. In Chapter V, we explore the downstream effects of CN stimulation on primary somatosensory cortex, in the context of spontaneous and evoked spindles under sedation. In summary, these findings constitute a proof-of-concept for the sensory half of a bidirectional sensorimotor prosthesis in the CN.

Degree Type
Dissertation

Degree Name
Doctor of Philosophy (PhD)

Graduate Group
Neuroscience

First Advisor
Timothy H. Lucas

Keywords
artificial, brainstem, neuroengineering, prosthetics, somatosensory, touch

Subject Categories
Engineering | Neuroscience and Neurobiology

CHARACTERIZATION OF SOMATOSENSATION IN THE BRAINSTEM AND THE DEVELOPMENT OF A SENSORY NEUROPROSTHESIS

Srihari Y. Sritharan

A DISSERTATION

in

Neuroscience

Presented to the Faculties of the University of Pennsylvania

in

Partial Fulfillment of the Requirements for the
Degree of Doctor of Philosophy

2018

Supervisor of Dissertation

_____

Timothy H. Lucas Jr., M.D., Ph.D.
Assistant Professor of Neurosurgery

Graduate Group Chairperson

_____

Joshua I. Gold, PhD
Professor of Neuroscience

Dissertation Committee:

Steven J. Eliades, M.D., Assistant Professor of Otorhinolaryngology
Joshua I. Gold, Ph.D., Professor of Neuroscience
Brian Litt, M.D., Professor of Neurology and Professor of Bioengineering
Diego Contreras, M.D., Ph.D., Professor of Neuroscience

Acknowledgments

I would like to thank Dr. Timothy Lucas and Dr. Drew Richardson for their invaluable mentorship across the years, as well as Polly Weigand for her dedication to teaching me the intricacies of primate research on a day to day basis. I am thankful for my thesis committee, Dr. Josh Gold, Dr. Brian Litt, Dr. Steven Eliades, and Dr. Diego Contreras, without whom this long journey would have been impossible. I would like to furthermore thank Ivette Planell-Méndez and Enrique Hernandez for being wonderful colleagues, Penn NGG and BGS for giving me the opportunity to develop as a scientist, my parents and sister for their undying support. Lastly, I give my regards to all of the monkeys for keeping me company on the days when I'd see almost no humans, and for giving their livelihood to help us develop a better world for the future.

ABSTRACT

CHARACTERIZATION OF SOMATOSENSATION IN THE BRAINSTEM AND THE DEVELOPMENT OF A SENSORY NEUROPROSTHESIS

Srihari Y. Sritharan

Timothy H. Lucas Jr., M.D., Ph.D.

Innovations in neuroprosthetics have restored sensorimotor function to paralysis patients and amputees. However, to date there is a lack of solutions available to adequately address the needs of spinal cord injury patients (SCI). In this dissertation we develop a novel sensor-brain interface (SBI) that delivers electric microstimulation to the cuneate nucleus (CN) to restore somatosensory feedback in patients with intact limbs. In Chapter II, we develop a fully passive liquid metal antenna using gallium-indium (GaIn) alloy injected in polydimethylsiloxane (PDM) channels to measure forces within the physiological sensitivity of a human fingertip. In Chapter III, we present the first chronic neural interface with the CN in primates to provide access to long-term unit recordings and stimulation. In Chapter IV, we demonstrate that microstimulation to the CN is detectable in a Three Alternative Force Choice Oddity task in awake behaving primates. In Chapter V, we explore the downstream effects of CN stimulation on primary somatosensory cortex, in the context of spontaneous and evoked spindles under sedation. In summary, these findings constitute a proof-of-concept for the sensory half of a bidirectional sensorimotor prosthesis in the CN.

Table of Contents

Chapter I: Introduction

1.1 Overview: General

Recent advances in neuroprosthetics have empowered motor-impaired users to volitionally control computer cursors, robotic arms, and even their own intact arm muscles. These innovations have opened the doors for patients with locked-in syndrome, tetraplegia, amputations and focal paralysis to interact with the external world.

However, those with paralysis typically also exhibit a complete lack of somatosensation or proprioception. Somatosensory perception exerts substantial influence on our interactions with our environment. In the absence of continuous somatosensory feedback, motor prostheses rely on vigilant visual feedback that is both slow and demands high levels of attention. Specifically, while innovations in mechanosensing and reanimation of artificial limbs are under development to aid amputees, there are currently no practical solutions for paralysis patients with intact limbs, such as those with spinal cord injury (SCI).

There is a critical need for the sensory half of a bidirectional sensorimotor prosthesis for paralysis patients with intact limbs.

Since recent motor prosthesis technologies do not alone lead to adequate practical use of a paralyzed hand, the objective of this dissertation project is to develop and test a wireless sensorimotor interface to restore continuous somatosensory feedback from the hand. The long-term goal of this project is to advance neuroprosthetic technology to meet the needs of patients with focal hand paralysis by improving clinical independence of the user [(Kageyama, Hirata et al. 2014),(Anderson 2004),(Blabe, Gilja et al. 2015)], as well as

decreasing the societal burden of their care since the sense of touch is essential to function and coordination.

Lastly, lack of wireless support in current sensory neuroprosthetics is a large reason why these devices have not been commercialized. Future devices must allow the user to operate their prosthesis independently without constant attendance by medical personnel to reduce the financial and operational burden on the user and medical system.

The flow of tactile information in a sensory neuroprosthesis will be broken into four steps and addressed this dissertation across four chapters: (II) wirelessly sensing the somatosensory information from the environment, (III) relaying the information electrically through a brainstem neural interface, (IV) encoding/learning the signal in a behavioral paradigm, and (V) lastly developing an understanding of the neural basis of cortical perception downstream after electrical stimulation.

In the following introduction, I establish the clinical motivation behind this research and review key concepts and essential theoretical considerations in sensor engineering, primate neurosurgery, electrophysiological and behavioral neuroscience that are relevant to this interdisciplinary project, including past and concurrent investigations from the somatosensory literature.

1.2 Overview: Clinical Motivation for Sensory Prosthesis Development

Over 5.6 million people in the United States (1.7% of the population) are paralyzed due to spinal cord injury, stroke, or other causes (Christopher and Dana Reeve Foundation (2009)). Across the years, significant financial and scientific resources have been devoted

to advancing the field of neuroprosthetics to meet the needs of these patients and decrease the societal burden of their care (Miranda, Casebeer et al. 2015). Despite promising proof-of-concept studies (Serruya, Hatsopoulos et al. 2002, Santhanam, Ryu et al. 2006, Moritz, Perlmutter et al. 2008, Velliste, Perel et al. 2008, Ethier, Oby et al. 2012, Hochberg, Bacher et al. 2012), the ultimate goal of reanimating paralyzed limbs has not been realized. However, a primary critical barrier to wide-spread implementation of neuroprosthetic technologies is the absence of somatosensory feedback (Gilja, Chestek et al. 2011, Thakor, Fifer et al. 2014).

Focal hand paralysis is typically accompanied by a total loss of touch, position, and movement sensation. The importance of these sense to volitional movement is exemplified in clinical cases of selective sensory loss; for these individual, routine manual tasks are virtually impossible (Richardson, Attiah et al. 2015), (Rothwell, Traub et al. 1982)).

For people with prosthetic limbs, a lack of sensory feedback to the user can drastically impact the practical use of their prosthesis as well. These users typically rely extensively on visual feedback when interacting with an external object, and therefore cannot reliably use their prosthesis without constant visual focus. (Gilja, Chestek et al. 2011, Bensmaia and Miller 2014) Fast, reliable sensorimotor feedback is essential for low-error, intuitive use of these prostheses [(Shanechi, Orsborn et al. 2017),(Leong and Doyle 2017),(Monzée, Lamarre et al. 2003), (Cunningham, Nuyujukian et al. 2011)].

Thus, even perfect restoration of movement via motor prostheses would not fully restore the desired functionality; somatosensation must be restored as well (Gilja, Chestek et al. 2011, Weber, Friesen et al. 2012, Bensmaia and Miller 2014). A *bidirectional*,

sensorimotor neuroprosthesis is required. In these devices, somatosensory stimuli are detected with artificial sensors and encoded in the brain using electrical microstimulation (Weber, Friesen et al. 2012).

Previous work has shown that microstimulation of somatosensory encoding areas in the brain can lead to discriminable percepts(Romo, Hernandez et al. 1998) and can guide movements(Fitzsimmons, Drake et al. 2007, London, Jordan et al. 2008, O'Doherty, Lebedev et al. 2011, Berg, Dammann et al. 2013). These studies demonstrate proof of-concept for a sensorimotor neuroprosthesis.

1.3 Overview: Previously Explored Sensory Encoding Targets

To create an artificial sensory pathway for a prosthesis, physical stimuli from the environment are detected by a sensor (e.g. robotic arm) and encoded in the brain using electrical stimulation (Weber, Friesen et al. 2012). Peripheral nerve stimulation appears to be highly effective in generating an intuitive sense of touch in amputees (Tan, Schiefer et al. 2014). Previous work from other groups has demonstrated that electrical stimulation of the median and ulnar nerves in the arm is able to induce sensory percepts in the hand with varying degrees of spatial resolution (Dhillon and Horch 2005, Raspopovic, Capogrosso et al. 2014, Davis, Wark et al. 2016).

Unfortunately, this strategy is not feasible for individuals with spinal cord injury (SCI), where signals to the peripheral nervous system cannot access the brain. How and where to encode somatosensory information with brain microstimulation in SCI patients is thus still an open question(Weber, Friesen et al. 2012). A number of target locations have been

explored including the dorsal root ganglia (Gaunt, Hokanson et al. 2009), sensory thalamus (Heming, Choo et al. 2011), and primary somatosensory cortex (S1) (O'Doherty, Lebedev et al. 2011).

Historically, S1 has been targeted based on its surgical ease of access at the surface of the skull. Prior studies have used S1 microstimulation to mimic vibrotactile sensations at the fingertip, which can lead to discriminable percepts (Romo, Hernandez et al. 1998, Kim, Callier et al. 2015) and guide basic movements (O'Doherty, Lebedev et al. 2011, Berg, Dammann et al. 2013, Klaes, Shi et al. 2014). Incurrent literature, the best documented performance to date had monkeys receiving S1 stimulation and required 15 daily sessions to discriminate between only two different stimulus frequencies (O'Doherty, Lebedev et al. 2011). Tactile information from a real-life environment can of course span much broader frequencies and stimulus qualities. *Scaling this performance up to more complex or continuous percepts may require a very different microstimulation target or paradigm.*

As a result, the current the reliance on S1 as an encoding site creates a potential barrier to further progress in sensory prosthetics. S1 has relatively distributed sensory representations. However, S1 microstimulation yields limited percepts (Kim, Callier et al. 2015) and is perceived in people only as vague flutter sensations. This is likely because these cortical representations are too diffuse to mimic the simultaneous activation of multiple afferent modalities and locations experienced during a typical manual task and thus, fails to generate a rich repertoire of independent sensory experiences [cite].

Despite decades of extensive exploration, direct S1 stimulation lacks the encoding fidelity necessary for clinical implementation. In the fields of auditory and visual neuroprostheses,

it has been similarly shown that stimulating cortical sensory areas is generally less effective in evoking intuitive percepts than stimulating upstream stages of the sensory pathway (Weber, Friesen et al. 2012).

These attractive upstream encoding targets, such as the dorsal column nuclei (DCN) in the brainstem, have remained largely unexplored in somatosensory literature. In particular, the cuneate nucleus (CN) within the DCN encodes for the entire upper body above vertebrae T9 (excluding the face, and is of highest interest as it contains the hand representations.

The CN in the brainstem is a logical alternative target because: (1) it is the first central processing stage for somatosensory information, (2) it receives direct input from the primary afferent nerves from the hand, (3) it relays this sensory information to thalamocortical networks and beyond, (4) it is spared following spinal cord injury, and (5) unlike the thalamus whose nuclei are deep in the brain, the CN sensory representations are condensed within highly compact, superficial nuclei along the dorsal surface of the brainstem (Figure 1.1).

1.4 Primary Objective: Develop a CN Sensor Brain Interface for Deafferented Patients

The **primary objective** in this dissertation is to develop and test a wireless sensor-brain interface (SBI) to restore continuous somatosensory feedback from the hand via a chronic CN interface.

Specifically, the SBI will be composed of a stretchable radiofrequency (RF) antenna to serve as passive sensors of mechanical stimuli at the fingertips, custom electronic circuits

to wirelessly acquire and process the sensor output in real-time, and a brainstem implant to encode information where it can be more fully processed by downstream neural circuits. This SBI is envisioned to make up one half of a complete sensorimotor neuroprosthesis that could ultimately restore feeling and function to a paralyzed hand, scaled and translated to the level of human application outside of a laboratory setting.

This device will operate as follows. External tactile stimuli are dynamically sensed by passive liquid-metal antennas at the level of the fingertip. Electronic control of the SBI is accomplished with two, battery-powered, low-power discrete circuits: (1) a sensor controller worn at the wrist and (2) a stimulation controller worn on the head. The sensor controller on the wrist transmits electromagnetic waves into the antenna and measures the amount of energy reflected back as a function of frequency. The frequency of this reflected energy, which represents specific tactile stimuli, is digitized and mapped to CN stimulation parameters. A user interface is developed to allow extensive control over the details of the mapping between sensor output and stimulation parameters. The parameters are then wirelessly sent to the stimulation controller, which then delivers microstimulation directly to the brainstem and provides user with somatosensory feedback (Figure 1.2).

For the development of this prosthesis, we will use male rhesus and cynomolgus macaques (M. mulatta, M. fascicularis). The awake, behaving macaque is the animal model of choice because somatotopic representations in our intended target of study, the cuneate nucleus, are more anatomically congruent between humans and macaques than any other animal model [(Florence, Wall et al. 1989), (Qi and Kaas 2006)].

To demonstrate proof-of-concept for this CN sensor-brain interface, this dissertation will evaluate four hypotheses across their respective chapters (Figure 1.3).

Chapter II begins at the level of the external stimulus, designing wearable, flexible radiofrequency (RF) antennae to serve as biocompatible passive sensors of tactile stimuli within the dynamic range of a human fingertip. This is then transduced from mechanical to electrical information, akin to mechanoreceptors in the human body. *We hypothesize that liquid gallium-indium alloy injected into microfluidic channels in PDMS can operate as a passive force sense that can transduce mechanical forces within the physiological range of a fingertip.*

We then in **Chapter III** address the necessary surgical and electrophysiological considerations to establish a chronic neural interface with the dorsal column nuclei in primates. *We hypothesize that chronic arrays can be implanted in the CN and maintain stable receptive fields to reliably record and stimulate across the lifetime of the array.*

Once an interface was implanted and stable across weeks, we quantified the detectability of CN electrical microstimuli in a behavioral paradigm in **Chapter IV** and specifically test whether the cuneate nucleus of the brainstem is a promising site to encode touch information. *We hypothesize that the CN is a suitable target for encoding somatosensory information in neuroprosthetic applications. We believe microstimulation in the CN will evoke intuitive and discriminable percepts on par with or better performance than previously established targets.*

Lastly, in **Chapter V** we shifted our focus to the downstream effects in cortex from peripheral and DCN electrical stimuli at the local field, multiunit, and single unit level,

which are important considerations for the underlying neural basis of perception of artificial stimulation. *We hypothesize that characterizing the cortical response of thalamocortical loops driven by CN or median nerve stimulation provides a physiological basis for the initial choice of stimulation patterns in a sensory neuroprosthesis, and establishes a mechanistic framework to interpret the influence of different patterns on perceptual performance.*

Due to the breadth of interdisciplinary topics in this thesis, the following subsections of the introduction will dive deeper into fundamental key concepts critical for establishing context central to each of the aforementioned chapters. This is followed by the results of each experiment in Chapters II through V, concluding with a discussion of limiting factors in the study and future directions in the field of sensorimotor neuroprosthetics.

1.5 Key Concepts for Chapter II: Development of a Liquid-Metal Passive Force Sensor

Existing approaches to detecting somatosensory information use robotic fingers equipped with sensors such as strain gauges and accelerometers (Wettels, Santos et al. 2008, Berg, Dammann et al. 2013). These designs are appropriate if the patient is an amputee and has a robotic hand, but not if the effector is the re-animated paralyzed hand. In the latter case, there is a need for wearable or implantable sensors.

In Chapter II, we develop wireless fully passive tactile sensors, which are created by implementing passive tags in a stretchable substrate whose resonant frequency changes with its shape and size.

Our tactile sensors and associated wireless electronics were chosen specifically with near-term clinical application in mind, based on concerns including user-friendliness, invasiveness, and potential benefit. Thus, there were a number of considerations we addressed when developing this technology for the SCI population.

First, these sensors and their associated hardware should have a minimal physical presence (e.g. no wires, no glove), and the entire system needs to be portable. Most existing neuroprosthetic systems, both motor and sensory, are confined to laboratories or hospitals where trained personnel oversee their use. The electronics would need to be developed such that the entire system is wearable or implantable and can be used continuously in daily life (Borton, Yin et al. 2013). Even at the present stage of pre-clinical development there is a compelling need for a portable system. The amount of practice with a neuroprosthetic device is directly related to performance (Ganguly and Carmena 2009, Koralek, Jin et al. 2012). Quantifying the performance levels achievable with distributed practice is critical to properly assessing the risk-benefit ratio of these devices for clinical translation.

Second, we assert that the ideal sensor should be fully passive (i.e. no active power source), rather than power-harvesting or battery-powered. In biomedical applications where wireless sensor nodes are attached or implanted in animal or human subjects, low-power sensing significantly extends the battery life of the wireless sensor nodes, while wireless-powered and passive-responsive sensing offers unlimited operation time, enabling long term monitoring without changing batteries. However, the relatively bulky volume, power hungry and the need for a battery can be impediments for long-term implantable sensors . It is for this reason that we focused on passive tags; these sensors are battery-less, thereby

making the sensors lightweight, compact, easily replaceable, and potentially implantable under the skin. As an additional real-world practical consideration, these sensors are hermetically-sealed in a polymer (i.e. water-tight).

While detection and restoration of tactile and proprioceptive sensing is a longer-term goal, proprioception is outside the scope of this thesis. Visual feedback can more reliably substitute for proprioceptive information than tactile information (Sarlegna, Malfait et al. 2010). The contact forces between the hand and an object is associated with very few visual cues and from a clinical perspective, reliance on these cues would be cumbersome at best. Therefore, this chapter focuses on the development of tactile sensing alone. Tactile information is composed of three major modalities: force/deformation, vibration, and temperature. We are concerned only with mechanical stimuli (force, deformation, vibration) as they are most important for volitional movement.

In this chapter, a wireless passive scattering force sensor node is proposed, designed and tested.

These sensors operate as follows. Compact antenna designs known as space filling curves are etched into a polymer to form hollow, watertight microfluidic channels. These channels are then partially filled by injection with eutectic liquid Gallium-Indium (GaIn) alloy, which constitutes the antenna tag. GaIn is a metal in liquid state at room temperature, but is biocompatible unlike Mercury (Chandler, Messer et al. 1994, W. 2001) Within this device is a well filled with an excess of GaIn, which when pressed by a finger, causes GaIn to flow freely further into the antenna channels and completely fill the remainder of the antenna channel. Upon releasing the finger, the GaIn retracts within the channel to its

previous default length. These dynamic changes in antenna length induce a shift in the resonant frequency of the tag, which can be detected via radiofrequency (RF) backscatter from an external device. This device then uses known material properties of the sensor to recover the tactile parameters of the original physical stimulus, such as orthogonal force at the fingertip or joint angle. These sensors are designed to be unobtrusive and scalable to any number of digits or skin locations.

As previously mentioned, an external device transduces and converts the mechanical information at the level of the sensor to electrical parameters for use in CN microstimulation. The development of this external device is beyond the scope of this thesis, but can be found in the body-area-network literature (Liu, Zhang et al. 2015). The following chapter assumes that this innovation in artificial sensory transduction is established, and turns our focus to the delivery of this microstimulation to the brainstem.

1.6 Key Concepts for Chapter III: Establishing a Chronic Neural Interface with the CN

The CN is the lowest sensory processing stage following the disruption of primary somatosensory afferents in spinal cord injury. Its efferent projections activate divergent sensory networks through cerebellar, thalamic and cortical pathways, thereby maximizing the probability of generating intuitive sensory percepts. The objective is to test our hypothesis that the CN is an effective site for sensory encoding within the confines of current commercial electrode array technology.

However, there are minimal published studies that delve into the neurophysiology of the CN in an awake model system that closely resembles the human condition. The majority of what is known about the function of the CN comes from studies with anesthetized cats that obviously lack an opposable thumb and independent digit control. However, there is sparse data available on primate CN function. The few published studies reveal the presence of descending modulation from sensory and motor cortex (Harris, Jabbur et al. 1965, Biedenbach, Jabbur et al. 1971, Chapman, Jiang et al. 1988), somatotopic organization of tactile inputs from primary afferents (Hummelsheim and Wiesendanger 1985), and high fidelity tactile and proprioceptive information transfer to the thalamus (24-25). Due to the technical challenges repeatedly accessing the CN and the impression that brainstem implants were too risky (Weber, Friesen et al. 2012), these studies were restricted to acute recordings with rigid electrodes in anesthetized monkeys.

The lack of a reliable method to access the CN in an awake primate left an unfilled knowledge gap about the role of CN in sensory perception.

In Chapter III, we present the first chronic array interface with the CN and leverage this methodology to provide the first long-term data on recording and stimulation from the CN of awake, behaving primates. These chronic multielectrode arrays provide stable electrophysiological access to the primate CN without causing significant neurological impairment.

This innovation was possible for two key reasons. First, the nucleus was readily accessible through a posterior fossa craniotomy, a standard neurosurgical approach that Dr. Lucas performs regularly in human subjects. Second, due to anatomical considerations,

commercial floating microwire arrays implanted in the CN undergo less micro-motion at the tissue-electrode interface (and therefore, less degradation) than using coupled electrodes or even potentially floating microelectrodes in cortex.

Previous studies have recorded single units from other nuclei of the pons and medulla in awake monkeys (Fuchs and Luschei 1970, Hoffman, Dubner et al. 1981). The technique involved fusing the upper cervical vertebrae to the occipital bone, stabilizing the head, and recording units acutely with metal microelectrodes through an occipital or parietal chamber. The craniospinal fusion reduced the motion of the brainstem relative to the skull, to which the electrodes were coupled, although this is not always required (Buford and Davidson 2004). At about the same time, a different approach for dealing with the issue of brain motion was developed for chronic unit recording in the cerebral cortex. Microelectrodes were constructed to move, or float, with the brain by using a flexible wire that decoupled them mechanically from a connector mounted on the skull (Salcman and Bak 1973). This idea was scaled up to arrays of floating microelectrodes, which are now commercially available and widely used for chronic recording in the cortex of awake animals (Rousche and Normann 1998).

Unlike the supratentorial cerebrum, the lower brainstem is not susceptible to significant inertial tissue deformations during rapid rotational acceleration and deceleration. The lobar regions of the brain, by contrast, bear the brunt of load forces during rapid head movements, as evidenced by the patterns of diffuse axonal injury (Davceva, Basheska et al. 2015, Jang and Lee 2017). Even in the absence of overt pathology, micro-motion at the tissue-electrode interface is considered a predominant factor in the functional degradation of

chronic electrodes implanted in the cortex (Streit, Xue et al. 2012). This degradation is a critical barrier to clinical implementation of brain-machine interfaces. Electrodes implanted in the CN could reasonably be expected to maintain viability longer than electrodes in other somatosensory targets.

The goal of this chapter is to evaluate the safety of this novel implant and the long-term stability of neural recordings obtained using this interface. Safety is a primary consideration for translational research. Injury to the CN or other brainstem nuclei could cause loss of sensation (touch, pain, temperature) or cranial nerve dysfunction. In addition to neural damage, the implantation surgery itself could lead complications such as stroke, bleeding or infection. Stability of the array is equally important. 'Stability' is operationally defined as consistent sensory representations and detection thresholds over the lifespan of the implanted array. Safety and stability are, by necessity, the first criteria to evaluate the translational potential of any novel implant.

Safety was assessed post-operation by our lab and the veterinary staff, and both monkeys in the study tolerated the surgery well with virtually no long-lasting neurological impairment. Stability was evaluated at the single-cell and cell-cluster level with a novel spike-field stability analysis for CN unit recordings. Chronic electrode arrays are routinely implanted in motor cortex and other cortical areas (Rousche and Normann 1998), and recording stability with these arrays has been documented by several studies with methods similar to those used here (Dickey, Suminski et al. 2009, Fraser and Schwartz 2012). These studies were used as benchmarks to evaluate the array stability in the brainstem, as well as the yield and longevity of the implant.

In the following chapter, we use this novel CN interface beyond electrophysiology studies to provide microstimulation to evoke detectable percepts in a behavioral paradigm.

1.7 Key Concepts for Chapter IV: Detection of CN Microstimulation

In the previous chapter, we have recently shown that chronic CN interfaces are well tolerated by primates over several months duration. This now allows us to characterize, with behavioral experiments, the percepts elicited by CN microstimulation.

Sensory encoding experiments have focused almost exclusively on cortical stimulation for the past decade (Gilja, Chestek et al. 2011, Weber, Friesen et al. 2012). Thus, to assess the suitability of CN as a sensory encoding target there are two logical steps left to address which define the current gap in knowledge between CN and cortical encoding targets. First, the next logical step is to determine the detectability of CN microstimulation. This has been previously explored in the dorsal root ganglia (Gaunt, Hokanson et al. 2009), sensory thalamus (Heming, Choo et al. 2011), and S1 (O'Doherty, Lebedev et al. 2011), but had not yet been explored in CN.

In Chapter IV, we present the first study to critically examine whether awake behaving primates can learn to detect chronic microstimulation of the CN in the paradigm of a decision task.

The second gap in knowledge is the ability to encode multiple discriminable percepts in the CN using microstimulation, to determine the spatial, frequency, and amplitude resolution of the prosthesis. This task is beyond the scope of this thesis but is addressed in detail in the Discussion section later on.

There are some key questions to answer to determine if the CN is a suitable target for detection. First, how long does it take the monkey to learn to detect the stimulus? The best case documented is in S1 (O'Doherty, Lebedev et al. 2011), which required 15 daily sessions to approach criterion levels. Second, at a given stimulation frequency, what is the electric current amplitude necessary to evoke detectable percepts, and are they safe levels? Can you recover chance probability in the task if the current is reduced towards zero? These questions are addressed in the body of Chapter IV and are compared to benchmarks in cortical stimulation literature.

The monkeys were trained on variant of an established Three Alternative Forced Choice Oddity (3AFC) somatosensory task from previous detection theory literature (Macmillan and C Creelman 2004). This task requires that the monkey moves and places their hand from stimulus to stimulus, as opposed to serial presentation of stimuli to a resting hand. This was done to provide the context of possible feedback inhibition of afferent information due to intended actions via descending motor pathways.

At first, our monkeys would be trained to detect vibrotactile stimuli from motor actuators. One out of three motors at random per trial would vibrate silently and the monkey would be rewarded for finding the correct answer. In this task, chance is defined as a probability of 33%, and significant performance above this level indicates that the monkey has learned to detect the stimuli. Once criterion performance was reached, the monkey was implanted and the task would switch to sham motors which trigger a stimulus train to the CN instead. To maximize likelihood of success, we initially performed receptive field mapping in the array to determine channels that had reliable single unit activity upon manual stimulation

of the fingertips. The performance on the CN stimulation task at first dropped back to chance levels, but within a two week time frame returned to criterion performance.

In this chapter, we show that both animals could detect these artificial stimuli. We document the learning curve to switch from detecting natural to artificial stimuli, and the threshold current amplitude necessary for detectable percepts. At plateau performance, both monkeys exhibited detection probabilities that were about twice the chance probability, and the time course was on par with past studies of sensory encoding (Fitzsimmons, Drake et al. 2007, O'Doherty, Lebedev et al. 2009, O'Doherty, Lebedev et al. 2011). Finally, we quantified detection probability as a function of stimulus amplitude. These behavioral data are the first to show that artificial CN activation is sufficient for perception.

Excitability of S1 is known to be correlated with perceptual performance (Haegens, Nacher et al. 2011), and it is furthermore known that peripheral stimulation can evoke S1 responses that last several times longer than the stimulus (Adrian 1941). However, these dynamics have not been previously shown with CN stimuli. With the knowledge that CN microstimulation evokes detectable percepts in S1, it behooves us to next investigate the downstream spatiotemporal dynamics of S1 in response to CN stimuli. In the next chapter, we delve into the dynamics of two cortical oscillations that have been previously investigated for decades in the somatosensory literature and present our findings in the context of dorsal column stimulation and chronic CN/S1 recordings.

1.8 Key Concepts for Chapter V: Spontaneous and Evoked Thalamocortical Oscillations under Sedation

Neural oscillations are present across various systems in the brain and are regarded to facilitate efficient information transfer (Buzsaki and Draguhn 2004), (Singer 2017), (Canolty, Ganguly et al. 2010). Although oscillations in corticothalamic loops are present in nearly every sensory system, these rhythms are purportedly strongest in the somatosensory system (Hsiang-Tung (1950)). In particular, there are two such oscillations we seek to investigate in the context of sensorimotor prosthetics, due to the fact that they involve the same areas of the nervous system targeted in the somatosensory SBI literature (Contreras and Steriade 1996), (Contreras, Destexhe et al. 1996), (Hsiang-Tung 1950).

The first of these rhythms are sleep spindles, defined as rhythmic oscillations (10-16 Hz) that spontaneously generate during early stages of sleep at a rate of 0.1-0.3 Hz beginning in the reticular neurons (RE) of thalamus and reverberating as a corticothalamocortical loop. [(Adrian 1941), (Hsiang-Tung 1950), (Destexhe, Contreras et al. 1994), (Contreras, Destexhe et al. 1996, Contreras and Steriade 1996), (Contreras, Destexhe et al. 1997), (Haegens, Nacher et al. 2011)].

The second oscillation of interest is known as evoked spindles/mu-alpha oscillations (~10Hz) , which occur when stimuli along the medial lemniscus pathway induces a longer-lasting corticothalamic reverberation (Hsiang-Tung 1950). In particular, single pulses delivered to median nerve have been shown evoke spindle times several orders of magnitude longer than the initial pulse, providing potential evidence as a mechanism for somatosensory amplification. It should be noted that previous literature has used the terms evoked spindle and somatosensory alpha rhythm interchangeably to represent the same phenomenon depending the varying philosophies of the authors (Andersen, Andersson et

al. 1968); however evidence to justify deeming these terms perfectly synonymous has remained an open question for 40 years.

It is important to note that these rhythms occur at nearly the same frequency and involve the same regions of the brain, but occur during different brain states (sleep vs. awake). Previous work has hypothesized that sleep spindles mediate consolidation of procedural memories through coordinated activity in striatal, hippocampal, and sensorimotor cortex (Fogel and Smith 2011, Laventure, Fogel et al. 2016). There is a second hypothesis that oscillations in a similar frequency range to mu/alpha coordinate extended sensorimotor networks, with behavioral evidence that perception can be modulated by the phase and power of these oscillations (Ai and Ro 2014, Tomassini and D'Ausilio 2018).

These two lines of work have rarely been connected in previous literature. Are these oscillations directly related? Is there a possibility that sleep spindles are performing sensorimotor replay in S1 in an effort to induce procedural memory consolidation, accounting for the similarity in frequency? These big questions cannot be answered in the scope of this thesis. Indeed, there are a number of physiological differences between the two rhythms (Contreras and Steriade 1996), just as there are similarities.

In this Chapter V, we seek to understand what occurs in somatosensory processing at the level of S1 after CN stimulation, by investigating the dynamics and functional role of these two types of cortical reverberations.

This chapter is broken into two parts: the first part leverages the variable depths of the electrode array to investigate the behavior of the evoked spindle/alpha rhythm in various cortical layers. The second part uses spike-phase analysis to compare spontaneous and

evoked spindles and finds a fundamental difference in the local field potential phase in single units locked to both rhythms. Together, these halves further the understanding of the brain-state dependent excitability of somatosensory cortex and can help inform future stimulation paradigms in the context of sensorimotor SBI.

1.9 Closing Remarks

The development of a sensor-brain interface is an inherently interdisciplinary project that requires innovation across a breadth of topics. These next four chapters investigate experiments that address critical gaps in knowledge in electrical/bioengineering, neurosurgery, electrophysiology, and behavioral neuroscience. These diverse experiments are tied together by their contributions to our overall goal of developing a somatosensory prosthesis that interfaces with the cuneate nucleus to reanimate the hand of deafferented patients.

The concepts reviewed in the introduction provide the reader with the necessary context to establish the critical need in each sector of neuroengineering research which justify the experiments in the chapters that follow.

Afterwards, the dissertation is concluded with an in-depth Discussion tying together results, limiting factors, future directions, and the overall impact to the field of neuroprosthetics.

Chapter II: Development of a Passive Scattering Force Sensor

Adapted from correspondences with Srihari Y. Sritharan, Matt Hongjie Zhu, Dr. Jan Van der Spiegel, Dr. Nader Engheta, Dr. David Issadore

2.1 Introduction

Flexible and stretchable electronics are rapidly gaining popularity in the field of biosensing for their ability to conform seamlessly to the body, enabling applications that were previously impossible with rigid, hard electronics (Rogers and Huang 2009, Park, Brenner et al. 2015, Wang, Huang et al. 2015, Shi, Manco et al. 2018). In particular, microfluidic channels filled with liquid metal are in development for use as tunable circuits to provide continuous biometric feedback in a variety of clinical applications (Masahiro, Xiaofeng et al. 2010, Huang, Wang et al. 2014).

Stretchable liquid metal antennas have been designed with detectable resonant frequency changes for use in dynamic sensing (Masahiro, Xiaofeng et al. 2010). However, many of these devices still require an external connection to an active sensing device to operate. This imposes a ceiling on the clinical translational capacity of the biosensor, as it creates the prerequisite for battery storage and replacement to maintain full function. In addition, while stretchable antennae are useful for measuring stress and strain, sensor antennae to measure pressure within physiological ranges have not been previously developed.

We propose to create a fully passive liquid metal force sensor that can be assessed wirelessly by radiofrequency (RF) backscatter.

This device is pressure sensitive and shifts its resonant frequency in a quasilinear relationship with the force applied. This sensor network is primarily designed for human finger tactile sensing as part of the paralyzed limb sensory restoration project. The proposed sensor node can also be adapted for other applications such as building structure monitoring. To provide proof-of-concept, this paper will choose a practical antenna design for the application of fitting the device on a human hand, and test its frequency response via wireless RF backscatter. Then, the pressure response will be tested to quantify the dynamic range of the device within physiological force levels.

2.2 Methods

Pressure Sensitive Microfluidic Antenna Fabrication

We developed a novel pressure sensitive microfluidic device that dynamically changes antenna length when pressure is applied to a well filled with dilute acid and hydrophobic fluid. The fabrication process was devised as follows:

Copper electrodes were etched from a 25micron thick Pyralux substrate (*3M Company*) using a printed wax resist and a ferric chloride etching solution for 25 minutes. Antenna designs were direct laser micromachined onto acrylic to create a mold. Subsequently, polydimethylsiloxane (PDMS) was prepared in a 20:1 ratio of base to curing agent weight. PDMS was cast onto the acrylic mold to form an antenna channel layer of 2mm thickness, and another batch of PDMS was poured into a flat dish to form a base layer of 2mm thickness. The two layers were thermally cured separately at 80 degrees Celsius for 2.5 hours. A PDMS stamp made from 20:1 ratio mixture was prepared on the base layer and

brought into contact with the antenna channel layer (Figure 2.1). Two copper electrodes were inserted at the interface and aligned with the channels. This closed device was then thermally cured at 80 degrees Celsius for 2.5 hours, and subsequently cut to size with a blade.

A 1mL Eppendorf tube was filled with 0.4mL of hydrochloric acid (HCl) and diluted with 0.4mL water, and 0.2mL of eutectic Gallium Indium (GaIn) alloy (Sigma Aldrich) was added to the tube. Tube was set aside until all bubbling from dissolving oxides halted. A syringe was used to draw up metal, then acid, respectively; this allowed the injection of acid then metal, respectively. All gas bubbles were discharged from the syringe into a proper disposal container.

To inject the fluidic channel, a 30 gauge needle tip was inserted at a 30 degree angle into each end of the channel. Injection began at the needle most distal to the force sensing pad, first injecting hydrophobic Aquapel (**??**) to fill the channel. Injection halted once liquid was exiting the proximal needle due to overflow. Then the syringe containing GaIn and HCl was used to sequentially inject HCl acid and then GaIn metal, until the metal reached the final leg of the antenna design. Upon completion, both needles were carefully removed from the device, and the pressure sensor was manually pressed to check for leaks.

Pressure applied to the well causes dilute HCl to fill the channels, dissolving the oxide skin of the GaIn in the channels, shrinking the total antenna length (Figure 2.2). This in turn, theoretically causes a upward shift in the resonant frequency of the antenna. Thus, frequency monotonically increases with orthogonal pressure. Upon release, the antenna returns to its default length.

Selection of Hilbert Curve Design

In recent years, passive radio-frequency back scattering tags have been successfully used in radio-frequency identification (RFID) technology (McVay, Hoorfar et al. 2006, Murad, Esa et al. 2006, Dau-Chyrh, Bing-Hao et al. 2008, Gibney and Rowe 2011, Aivazis, Siakavara et al. 2012). The space-filling curve, thanks to its compact size and its narrow bandwidth of frequency response, is widely used in the design of passive scattering tags (Sagen 1994). The peak scattering frequency of a space-filling-curve tag is very sensitive to the dimension of the tag. This makes the space-filling-curve tag a good candidate for a force or stretch sensor. With the recent advancements in liquid metal antenna research (Cheng, Rydberg et al. 2009, Ju-Hee, Jacob et al. 2009, Masahiro, Xiaofeng et al. 2010), the implementation of a passive scattering force/stretch sensor is made possible by using a flexible liquid-metal-filled space-filling-curve tag. The sensor node takes advantage of the backscattering frequency response of space-filling-curve tags. In each passive scattering sensor node, a 2nd-order Hilbert-curve tag (Sagen 1994) is used for sensor node identification, while another 2nd-order Hilbert-curve tag is used for force sensing.

The space-filling-curve tags, shown in Figure 2.3, act as microwave backscattering objects. The major advantages are: 1) completely passive response by backscatter microwave energy; 2) compact size compared with other antennas at the same resonant frequency; 3) resonant frequency more sensitive to size change than that of dipole antennas.

A 2nd-order Hilbert curve is used to implement the proposed wireless sensor because of its simple geometry and ease of fabrication. As shown in Figure 2.2, the Hilbert-curve tag

is sensitive to the polarization of the incident microwave because it is symmetrical about a line.

When the incident electric-field polarization is along the axis of symmetry of the Hilbert curve, we define the position of the tag as in the polarization direction, also known as i-polarization. Similarly, when the incident electric-field polarization is perpendicular to the axis of symmetry of the Hilbert curve, we define the position of the tag as quadrature to the polarization direction, also known as q-polarization.

The incident microwave induces current in the segments of the 2nd-order Hilbert-curve tag, which are laid along the polarization of the incident electric-field, as shown in Figure 2.3. The longest path along which the induced current can pass defines the electrical lengths of the tag. The electrical length further determines the resonant frequency of the tag. For tags placed in the i-polarization position, the induced current is always 0 at the symmetry point, so the electrical length is half of the total trace length. On the other hand, for tags in the q-polarization position, the induced current does not have to be 0 except at the physical ends of the tag trace. Therefore, the electrical length is the full trace length. This also indicates that the resonant frequency of a 2nd-order Hilbert-curve tag in i-polarization should be about twice as high as that of a tag with the same size in q-polarization, as illustrated in Figure 2.3.

The prototype force sensitive antennae with the 2nd-order Hilbert-curve shape were constructed in the lab of Dr. David Issadore (Figure 2.6). Various sizes and models were tested, with similar frequency responses but varying ergonomic profiles.

2.3 Results

RF Backscatter Experiment

The simulation and experimental results presented in this section were obtained with the help from Dr. Milin Zhang, a post doctoral research fellow from the Department of Electrical and Systems Engineering at University of Pennsylvania. The experiments were done inside the anechoic chamber of the Antenna Research Lab at Villanova University, with the help from Dr. Christopher Thajudeen and Dr. Ahmad Hoorfar from Villanova University.

Figure 2.6 shows the measured frequency responses of the 2nd-order Hilbert curve tags with segment lengths (L) equal to 6mm, 7mm, and 8mm, respectively, at a distance of 0.3m away from a horn antenna, which is used to radiate the incident waves to the tags and to pick up the reflected waves. The experiments were conducted in a microwave anechoic chamber. In the left-hand plot, the reflection frequency response peaks at 2.6GHz for the tag with L=8mm, at 3.0GHz for the 68 tag with L=7mm, and at 3.5GHz for the tag with L=6mm. The right-hand plot in Figure 2.6 shows the responses of 2 by 2 arrays with the 2nd-order Hilbert-curve tags where in each array the 4 tags have the same size. It is clear that the array shows stronger response in magnitude than a single tag, but the resonant frequency of each tag and its corresponding array with the same segment length stays the same. The figure also shows that the results with the single 2nd-order Hilbert-curve tags exhibit a signal-to-noise ratio large enough to distinguish the reflected frequency response of each tag. Therefore, our use of 2nd-order Hilbert-curve tags is justified for designing and building passive backscattering wireless sensor nodes.

Quantifying Pressure-Length Relationship

We next tested the frequency response of the liquid metal prototypes. As shown in Figure 2.7, frequency responses are measured with the liquid metal sensing tags placed in q-polarization position. When 1 segment of the liquid metal is suppressed into the channel, the resonant frequency of the sensing tag is at 2.9GHz. When 2 segments of the liquid metal is suppressed in to the channel, the resonant frequency of the sensing tag is at 3.2GHz. When 3 segments of the liquid metal is suppressed in to the channel, the resonant frequency of the sensing tag is at 3.5GHz. These results prove the change of the length of the liquid metal trace results in the resonant frequency change of the sensing tag.

Lastly, we measured the relationship of the microfluidic antenna length to the pressure applied to the device. Using incremental standardized weights and an optical micrometer (*Keyence*)**,** we were able to characterize the response and found that within the range of 2 to 12 Newtons of force, the response was linear. This range is within the realm of reasonable values for fingertip forces (Birznieks, Jenmalm et al. 2001, Fortier-Poisson, Langlais et al. 2015).

2.4 Conclusion and Future Work

A wireless passive scattering force sensor node is described and tested. The sensor node takes advantage of the back-scattering frequency response of the space-filling curve tags. In each sensor node, a 2nd-order Hilbert-curve tag is used for sensor node identification, while another 2nd-order Hilbert-curve tag is used for force sensing. Experimental results successfully demonstrated the feasibility to wirelessly and selectively turn on a sensor node

by radiating the corresponding resonant frequency of its ID tag. The resonant frequency of the sensing tag on the selected sensor node is detected by a frequency sweep within the sensing spectrum. The resonant frequency of the sensing tag is then matched to the amount of force applied. The future work on the passive scattering wireless sensor node design includes 1) implementation of multiple sensor nodes, with the goal of utilizing all ten fingers in concert 2) complete wireless sensor node and wireless sensor network experiments; 3) further optimization of the geometry; 4) detailed characterization.

Chapter III: A Chronic Neural Interface to the Macaque Dorsal Column Nuclei

Adapted from Journal of Neurophysiology, May 2016

Andrew G. Richardson, Pauline K. Weigand, Srihari Y. Sritharan, and Timothy H. Lucas

3.1 Introduction

The dorsal column nuclei (DCN) receive tactile and proprioceptive signals directly and indirectly from primary afferents and convey this information predominantly to the thalamus. From studies in cats, it is clear that substantial processing of ascending information occurs in these nuclei (Aguilar, Rivadulla et al. 2003, Leiras, Velo et al. 2010). Parallel studies have rarely been conducted in monkeys, despite some clear differences in their anatomy (Boivie and Boman 1981, Cheema, Rustioni et al. 1985, Bentivoglio and Rustioni 1986). The relatively few studies of monkey DCN function have shown the nuclei to receive somatotopically-organized tactile inputs (Xu and Wall 1999), to transmit both tactile and proprioceptive signals with high fidelity (Hummelsheim and Wiesendanger 1985, Witham and Baker 2011), and to be modulated by descending input from sensorimotor cortex (Harris, Jabbur et al. 1965, Biedenbach, Jabbur et al. 1971, Chapman, Jiang et al. 1988). However, these studies were all conducted with anesthetized monkeys. Correlating DCN neuronal activity with sensorimotor behavior in awake monkeys is an important next step to understanding the role of this critical node in the somatosensory pathway.

Prior studies have recorded single units from other nuclei of the pons and medulla in awake monkeys (Fuchs and Luschei 1970, Hoffman, Dubner et al. 1981). The technique

involved fusing the upper cervical vertebrae to the occipital bone, stabilizing the head, and recording units acutely with metal microelectrodes through an occipital or parietal chamber. The craniospinal fusion reduced the motion of the brainstem relative to the skull, to which the electrodes were coupled, although this is not always required (Buford and Davidson 2004). At about the same time, a different approach for dealing with the issue of brain motion was developed for chronic unit recording in the cerebral cortex. Microelectrodes were constructed to move, or float, with the brain by using a flexible wire that decoupled them mechanically from the array connector mounted on the skull (Salcman and Bak 1973). This idea was scaled up to arrays of floating microelectrodes, which are now commercially available and widely used for chronic recording in the cortex of awake animals (Rousche and Normann 1998).

The goal of the present work was to assess whether chronic floating arrays provide a viable method for recording units from the macaque DCN. We hypothesized that the floating design would compensate for the relative motion between the brainstem and skull and provide stable unit recording. Since the electrodes in these arrays are not movable after implantation, this new approach lacks the ability of the earlier technique to search for neurons. However, the potential advantages including recording from freely-behaving (i.e. not head-fixed) monkeys and stably recording from the same DCN units for many days.

We implanted two different types of commercial electrode arrays into the DCN of two macaques. We characterized the access to DCN sensory representations afforded by the array designs. We further assessed the stability of the unit recordings. We demonstrate that chronic arrays targeting the macaque DCN can be safe and can provide months of access

to single units. An abstract of this work was presented previously (Richardson, Weigand et al. 2014).

3.2 Materials and Methods

Two untrained male rhesus macaques (*Macaca mulatta*), monkeys B and C (12-14 kg), were used in this study. All procedures were approved by the University of Pennsylvania Institutional Animal Care and Use Committee and adhered to National Institutes of Health guidelines on the use of laboratory animals.

Brainstem implant

The animals were anesthetized with 1-2% isoflurane and positioned in a stereotactic frame. The frame was inclined approximately 20° above horizontal so that the suboccipital region was more accessible. Through a midline skin incision, neck musculature was dissected to expose the upper cervical vertebrae and the occipital bone. A 1.5-cm^2 craniotomy was performed adjacent to the foramen magnum. The posterior atlantooccipital membrane and dura were incised and the dorsal brainstem was visually identified. The DCN were targeted at the level of the obex. A Utah electrode array (monkey C; 96 electrodes, 400-µm spacing, 1.5-mm electrode length, Blackrock Microsystems) or high-density floating microelectrode array (monkey B; 32 electrodes, 250-µm spacing, 1.5, 2.0, 2.5, and 3.0-mm lengths, MicroProbes for Life Science) was positioned over the DCN with a stereotactic carrier. The former was inserted rapidly with a pneumatic actuator while the latter was inserted slowly at a rate of approximately 0.2 mm/min until fully seated. In the latter case, transient bradycardia was observed which ceased once the insertion pressure

subsided. The array wire bundle was tunneled under the skin to a separate scalp incision at the vertex of the skull, where the array connector was anchored with screws and dental acrylic. Finally the dura, neck musculature, and skin were approximated and closed.

Peripheral stimulation

Experimental sessions were conducted with the animals sedated (4 mg/kg ketamine, 0.05 mg/kg dexmedetomidine). To electrically stimulate peripheral nerves transcutaneously, two disposable skin electrodes (1.1-cm diameter) were placed approximately 5 cm apart on the flexor surface of the forearm at the wrist (median nerve) or posterior to the medial malleolus (tibial nerve). Monophasic square pulses of 200 μs duration were delivered at 1 Hz (DigiStim III, Neuro Technology Inc.). Stimulus amplitude was adjusted to achieve small, visible flexion movements of the fingers or toes.

To mechanically stimulate the skin, a 4-mm diameter circular plastic rod was used. The rod was threaded into a 2 kg-capacity load cell (REB7, Loadstar Sensors) to quantify the force profile of each stimulus. Other methods, including manually brushing the skin and rotating joints were also used to identify receptive fields, although these stimuli were not quantified.

Neural recording

During the mapping sessions, the wide-band (0.35-7500 Hz) neural signals were recorded at 25 kS/s/ch and saved for offline processing (ZC32/96 headstage, PZ2 preamplifier, RZ2 processor, RS4 data streamer, Tucker-Davis Technologies). The analog output of the load cell used for mechanical stimulation was digitized and saved by the same

system. The system performed online spike detection (300-6000 Hz bandpass filter, threshold set at 5 standard deviations) to provide real-time auditory and visual feedback for identifying neuronal receptive fields. The spike times were saved for offline sorting.

Data analysis

Detected spikes were sorted into single units using a semi-automated algorithm to cluster the scores of the first three principal components of the spike waveforms (OpenSorter, Tucker-Davis Technologies). Then for each unit, we computed the spike-triggered average of the wide-band neural signal recorded on each electrode in a 6-ms window centered on the spike times. The resulting average waveform for the electrode on which the unit was recorded was the mean spike waveform (MSW). The set of average waveforms for every other electrode was called the spike-triggered field (Radunovic, Annane et al.), which was composed of M-1 waveforms where M was the number of electrodes on the array. Separate averages were computed for every 500 spikes, resulting in floor(N/500) sequential observations of the MSW and STF during a session where N was the total number of spikes.

The MSW and STF were used to determine whether each pair of units came from the same or different neurons. For this analysis, each MSW and STF was categorized by four attributes: the *session* in which it was recorded, the *electrode* on which the triggering unit was recorded, the triggering *unit* identify, and the *time* (i.e. order in the sequence) of the block of 500 spikes from which the average waveform was computed. These four attributes were used to group each pair of units into one of three groups: *true positives* (same session, same electrode, same unit, different times), *true negatives* (same session, same electrode,

different units, all times), and *unknowns* (different session, same electrode, all units, all times). By grouping pairs of units in this way, we could evaluate the stability of units across sessions (unknown group) using a statistical classifier trained on unit pairs assumed to be from the same neuron (true positives group) and unit pairs assumed to be from different neurons (true negatives group).

The true positives group contained pairs of features from the same unit recorded at different times within a session (Dickey, Suminski et al. 2009). We assumed units recorded within a session were stable. The true negatives group was composed of pairs of units recorded in the same session and on the same electrode but identified in the sorting analysis as different units. This is a different definition of true negatives from past neuronal stability analysis, which used pairs of units recorded on different electrodes (Dickey, Suminski et al. 2009, Fraser and Schwartz 2012). However unlike the MSW and other previously proposed identifying features of units, the STF is spatially specific such that two STFs can be compared only if the triggering electrode is the same. Thus all groups, including the true negatives, involved comparisons of units recorded on the same electrode.

For all pairs, feature similarity scores were computed, both for the MSW and STF, as the average Pearson's correlation coefficient between the waveforms. The average was taken over all the pairwise combinations of the feature observations. For the STF, the average was also taken over the M-1 waveforms. However, we found that the STF was most informative for classification when we eliminated those STF waveforms that contained no peaks. We computed the signal-to-noise ratio (SNR) of each STF waveform (maximum / standard deviation) and excluded the correlation coefficient from the average

when both waveforms had an SNR below 3 (see Results). The Fisher transformation was applied before averaging correlation coefficients to reduce bias and normalize the distributions of the resulting similarity scores (Corey, Dunlap et al. 1998).

Linear discriminant analysis classifiers were trained to determine the optimal decision boundary between the similarity scores of the true positive and true negative groups. Linear classifiers were trained using only MSW, using only STF, and using both features to evaluate the relative importance of each feature. Quadratic classifiers yielded nearly identical performance. Performance of the classifiers was quantified by the area under the receiver operating characteristic curve. The classifier using both MSW and STF features was then used to label each unit pair in the unknown group as being from the same or different neuron. Finally, pairs labeled the same in adjacent sessions were tabulated to come up with the final number of sessions that each stable neuron was recorded.

Spike train irregularity was evaluated by computing the quantity $m_i = |\log(I_i/I_{i+1})|$ for each pair of adjacent interspike intervals I_i and I_{i+1} (Davies, Gerstein et al. 2006). For robustness to outlier intervals, the irregularity value, IR, for each unit was defined as IR = median(m).

Histology

With the monkeys still in good health, the experiments concluded when no further unit activity was detected. At that time, the monkeys were deeply anesthetized with pentobarbital, perfused transcardially with 0.1 M phosphate buffer (PB), fixed with 3% paraformaldehyde with 0.1% glutaraldehyde and 0.2% picric acid, and rinsed with 30% sucrose-PB. Brainstems were photographed *in situ* prior to blocking to aid in

reconstruction. The microelectrode arrays were carefully removed with fine forceps. Tissue blocks were post-fixed overnight in 20-30% sucrose-PB to cryoprotect before sectioning. Sequential, 50-µm thick frozen sections were cut. To visualize electrode tracks and identify nuclei, cytochrome oxidase staining was used. For this staining, sections were incubated until sufficiently differentiated at 40ºC in 0.02% diaminobenzidine (Sigma-Aldrich), 0.03% cytochrome C (Calbiochem), 0.015% catalase (Sigma-Aldrich), 2% sucrose, 0.03% nickel-ammonium-sulfate, and 0.03% cobalt chloride in 0.05 M PB of pH 7.4 (Li, Patel et al. 2013).

3.3 Results

Microelectrode arrays were implanted chronically into the dorsal surface of the brainstem of two rhesus macaques. A 96-electrode Utah electrode array (UEA) was implanted in Monkey C for 148 days. A 32-electrode floating microelectrode array (FMA) was implanted in Monkey B for 64 days. Both animal tolerated the chronic implants well and were in good health through the end of the study. Histology confirmed the placement of the electrodes in the dorsal column nuclei (DCN). Individual electrode tracks were identified in cytochrome oxidase-stained sections (Fig. 3.1A) and were used to reconstruct the placement of the arrays relative to the underlying nuclei (Fig. 3.1B). The UEA in monkey C spanned the entire mediolateral extent of the right cuneate nucleus (CN) and right gracile nucleus (GN) and partially overlapped with the left GN. The UEA electrodes had a uniform recording depth of 1.5 mm, but the array was incompletely inserted such that electrodes with a more rostral position were progressively shallower. The FMA in monkey B spanned portions of the right CN and GN near the level of the obex. The

staggered lengths of the FMA electrodes (1.5, 2.0, 2.5, and 3.0 mm) permitted recordings along the dorsoventral axis of the nuclei.

Receptive field mapping

Initial electrophysiological characterization of the DCN interface was obtained by recording field potentials evoked by transcutaneous electrical stimulation of peripheral nerves (Moller, Sekiya et al. 1989). For this and the subsequent mapping procedure, the monkeys were lightly sedated. Figure 3.2 shows the results from monkey C but similar results were obtained from monkey B. Single pulses delivered to the right median nerve at the wrist evoked a triphasic response with 5.1-ms average latency to the first peak (Fig. 3.2A left). The amplitude of the stimulus-evoked response varied considerably across the 96 electrodes. The spatial distribution of response amplitude across the UEA (Fig. 3.2A right) corresponded with the approximate location of the CN (Fig. 3.1B). Single pulses delivered to the right tibial nerve at the ankle evoked a largely monophasic response with 11.3-ms onset latency (Fig. 3.2B left). The largest response amplitudes were more medial, corresponding with the location of the GN (Fig. 3.2B right). The gradual decrease in response amplitudes rostrally was likely due to the incomplete UEA insertion described above.

Next, we mapped the receptive fields (RFs) of single units recorded on the DCN arrays using mechanical stimulation of peripheral mechanoreceptors. A hand-held, force-sensing probe was used to deliver punctate cutaneous stimulation while recording neuronal activity (Fig. 3.3A). Light brushing of the hairy skin and passive joint rotation were also used at times to identify the location of the maximum neuronal response. Typical stimulus-

response results are shown in Figure 3.3B. The majority of recorded units in the sedated animals (76%) had little baseline activity. These units only fired action potentials when a stimulus was delivered in their RF. Several response profiles were observed. Tonic responses were typical of RFs on the hairy skin of the body (Fig. 3.3B left). Transient responses to the probe making and breaking contact with the skin, similar to rapidly adapting primary afferents, were typical of RFs on the glabrous skin of the hand (Fig. 3.3B right).

In addition to spike rate profile differences, these examples demonstrate differences in spike train irregularity (i.e. variability of interspike intervals). We quantified irregularity with a metric, termed IR, that is independent of spike rate (Davies, Gerstein et al. 2006). In these examples, spike trains in response to stimulation of the skin of the back (Fig. 3.3B left) were more regular (IR = 0.58) than spike trains in response to digit stimulation (IR = 0.97) (Fig. 3.3B right). In mapping sessions conducted over several months, 629 single units were recorded (468 in monkey C and 161 in monkey B). The distribution of IR values for these units is shown in Figure 3.4A. The multimodal distribution highlights the heterogeneity of this spike train statistic for the sampled neuronal population. Units with very regular spike trains (IR < 0.6) had a well-defined spike frequency, as determined by the peak of their narrow interspike interval histogram (ISIH). Spike frequencies for this subset of regular-spiking units were most often within the alpha band (8-14 Hz) (Fig. 3.4B), an important rhythm in somatosensory information processing (Haegens, Nacher et al. 2011, Ai and Ro 2014).

Of the 629 recorded single units, RFs were identified for a total of 315 units: 230 units in monkey C (recorded on 47 of 96 UEA electrodes) and 85 units in monkey B (20 of 32 FMA electrodes). For the summary presentation in Figure 3.5, each RF was placed into one of 16 body-segment categories, from shoulder to tail. Only unique RF categories found at each electrode are shown. The resulting maps had several interesting features. First, the overall pattern of RFs was consistent with the histological and evoked potential findings. Right upper body RFs, attributable to CN neurons, were found laterally and right lower body RFs, attributable to GN neurons, were found medially. RFs on the left side of the lower body were also recorded on the medial-most column of the UEA (Fig. 3.5A), in agreement with the array location reconstruction (Fig. 3.1B). Second, there was a noticeable diversity of RFs recorded at individual electrodes, perhaps as a result of convergent afferent input to the DCN (Witham and Baker 2011). This was particularly true of the middle columns of the UEA near the putative boundary of the GN and CN (Fig. 3.5A). Three or more RF categories were observed on 21 of the electrodes across both arrays.

Finally, we examined whether there was a relationship between the RF and the irregularity of the evoked spike trains. We found a significant effect of RF category on the mean IR value, as assessed by a one-way ANOVA ($F_{13,299} = 3.28$, $p = .00011$) (Fig. 3.5C). With the exception of the leg category, the overall pattern was for units with RFs on the torso (e.g. abdomen, ribs, chest, back) to produce more regular spike trains than units with RFs on the extremities (e.g. tail, foot, fingers, arm).

In summary, the whole-body mapping results confirm the proper placement of the arrays. Furthermore, they provide insight into the preferred frequency and RF-dependence of DCN spiking patterns. Most importantly, they demonstrate the long-term functionality of the chronically-implanted arrays, which yielded high-quality neuronal recordings for almost five months in monkey C and over two months in monkey B.

Neuronal stability analysis

An advantage of chronic recording is the potential to track the same neurons over multiple days. If the recordings are stable, one can study neuronal correlates of processes that evolve over timescales longer than a typical daily recording session (e.g. injury recovery, perceptual learning and memory) (Richardson, Borghi et al. 2012). To evaluate this possibility for our chronic DCN implants, we performed a stability analysis of the units recorded during the mapping sessions.

The first step was to compute identifying features of each unit. A prior neuronal stability analysis used two features: the mean spike waveform (MSW) and the interspike interval histogram (ISIH) (Dickey, Suminski et al. 2009). The latter was not a good feature for these data. The intrinsic baseline spike rate was typically low, the stimulus-driven spike rate was often dependent of the details of the stimulus (e.g. higher force led to a higher rate), and the stimulus varied between sessions (Fig. 3.3B). As an alternative to the ISIH, we considered features that reflect each unit's unique position within the neural network sampled by the multielectrode array. For example, a recent neuronal stability analysis used a feature based on cross-correlation of the spike trains of all pairs of units simultaneously recorded on the array (Fraser and Schwartz 2012). This feature presumably captured some

stable aspect of network connectivity, such as common inputs to groups of neurons. However, again due to the general lack of baseline spiking and thus simultaneous spiking activity in pairs of units, this feature was not generally useful for the DCN dataset.

Instead, we used a feature based on the spike-triggered average of the wide-band neural activity recorded throughout the array (Fig. 3.6). This feature, which we called the spike-triggered field (Radunovic, Annane et al.), captured any activity (e.g. spikes, postsynaptic potentials) on other electrodes that was sufficiently time-locked to the triggering spikes and sufficiently close to the triggering electrode. We interpreted peaks in the STF to reflect local network connectivity or activity propagated along neuronal processes (Li, Gauthier et al. 2015). And we hypothesized that these peaks would be a stable feature that, along with MSW, could identify units across sessions. In Figure 3.6A, the MSW is shown in gray for three sessions with monkey B spanning 5 days. This unit was recorded on the electrode shaded gray in the array diagram on the right. For each session, the STFs of the other 31 electrodes on the FMA were computed in a 6-ms window centered on the spike times. A qualitatively consistent pattern in the STFs was seen across the three sessions. There was a large (25-μV), triphasic peak in one STF that preceded the triggering spike by 0.4 ms (Fig. 3.6A pink trace). This STF came from an electrode two away from the triggering electrode in the array (Fig. 3.6A right). However, such large peaks in the STFs were relatively uncommon. A more representative example is shown in Figure 3.6B. Two units were recorded on an electrode for three sessions with monkey C. The STFs of the other 95 electrodes on the UEA were computed in a 2-ms window centered on the spike times for each unit. Again, a qualitatively consistent pattern was seen in the STFs across sessions

and, importantly, the STFs for each unit appeared to be distinct. The STF peaks were small (most < 5 μV) and only resolvable due to the enhanced signal-to-noise ratio of the triggered average. The largest STF peaks occurred on electrodes immediately surrounding the triggering electrode (Fig. 3.6B right). Thus the STF could, at least in some cases, provide a unique signature of a single unit across sessions.

Pearson's correlation coefficient was used to quantify the similarity of both the MSW and the STF for pairs of units. Subsequently, a linear discriminant analysis classifier found the optimal decision boundary (black line, Fig. 3.7A,B) between the similarity scores of unit pairs assumed to be from the same neuron (red circles) and unit pairs assumed to be from different neurons (black circles; see Methods for group definitions). A receiver operating characteristic (ROC) curve was used to evaluate the classifier's ability to distinguish between these two groups. For monkey C, classification using both the MSW and STF performed better than classification using the MSW or the STF alone (Fig. 3.7C). The area under the ROC curve (Hoofnagle, Whiteaker et al.) for the MSW + STF classifier was .983, which was significantly greater than that of the MSW classifier (AUC = .963, p = .005) and the STF classifier (AUC = .952, p = .002) (Vergara, Norambuena et al. 2008). For monkey B, the MSW + STF classifier performance was statistically equal to the MSW classifier performance (AUC = .976 vs. .960, p = .096, Fig. 3.7D). The area under the ROC curve was significantly lower for the STF classifier (AUC = .912, p = .012). These results demonstrate that, across the population of recorded units, the STF was a useful predictor of unit identify for the UEA but not for the FMA.

The difference in predictive power of the STF was explained by the array interelectrode distance (IED). The UEA had a consistent IED of 0.4 mm. The FMA had a variable IED (due to the variable electrode lengths), which was on average 0.87 mm. Peaks in the STF, as quantified by the signal-to-noise ratio (SNR), occurred mostly on electrodes neighboring the triggering electrode (Fig. 3.7E). The SNR reached a floor value of about 3 at distances of 1 mm and greater. Thus we suggest that more information regarding the local function connectivity was captured by the higher-density UEA than the FMA, resulting in superior performance of the STF for the former.

Finally, using the decision boundary from the MSW + STA classifier, unit pairs that were recorded on the same electrode but different sessions (gray circles, Fig. 3.7A,B) were classified as belonging to the same or different neurons. For monkey C, 158 of 468 sorted units were found to belong to 40 stable neurons (i.e. neurons observed for two or more days). For monkey B, 33 of 161 sorted units were found to belong to 16 stable neurons. The timespan over which these 56 neurons were stably recorded by the chronic arrays is summarized in the survival curves in Figure 3.7F. Most neurons were stable for less than 10 days, although the UEA recorded a few neurons for about a month. Unit recording on the UEA was, overall, more stable than on the FMA.

Receptive field stability

The mapping sessions identified RFs of 315 single units. The stability analysis identified a set of 56 DCN neurons each of which was observed over two or more mapping sessions. Next, we asked whether the RFs of the stable neurons were consistent across sessions.

The analysis was restricted to the 23 of 56 stable neurons in which RFs were observed over multiple sessions. The stimulus-response characteristics for one of these 23 neurons is shown in Figure 3.8A. In mapping sessions spaced 5 days apart, the two units attributed to the same neuron both responded maximally to skin pressure over the 5^{th} intercostal space. To summarize the RFs of the stable neurons, we again placed each RF into one of 16 body-segment categories, from shoulder to tail. Qualitatively, the category was very consistent over repeated RF observations of the same neuron (Fig. 3.8B). To quantify this effect, we identified the modal (i.e. most frequently observed) category for each of the 23 stable neurons. The modal categories were observed in 85.2% of the RFs for units attributed to these neurons. The same categories were only observed in 44.4% of the RFs for all units recorded on the corresponding electrodes, since multiple RF categories were typically seen on the same electrode (Fig. 3.5). The difference in proportions was significant ($\chi^2(1) = 30.2$, $p < .0001$). The result suggests that, at least at this coarse level of description, the RFs of DCN neurons are stable.

Further confirmation of the identity of the example neuron in Figure 3.8A was seen in the consistently regular spiking pattern, in which a spike was discharged approximately every 100 ms. The difference in IR value between the two sessions was 0.16. In our final analysis, we computed the IR difference for all unit pairs and grouped them in the same manner as in the stability analysis. The IR difference distributions of the true positive pairs and true negative pairs were significantly different (Kolmogorov-Smirnov test, $D = .201$, $p = .008$) and had mean absolute values (MAV) of 0.21 and 0.42, respectively (Fig. 3.8C). Thus spike train irregularity was an additional identifying feature of DCN units and, since

not used as such in the stability analysis, could evaluate the performance of the MSW+STF classifier. The IR difference distributions of classified positive pairs (MAV = 0.24) and classified negative pairs (MAV = 0.40) did not significantly differ from true positive and true negative distributions, respectively (D = .128, p = 0.281 and D = .082, p = .397) but did differ from each other (D = .179, p = .004) (Fig. 3.8C). The results confirm the classification based on MSW+STF features. Classified positive unit pairs had a narrow distribution of IR differences, just as true positives. Together, these final analyses demonstrate the stability of both the afferent input to and temporal response of DCN neurons.

3.4 Discussion

We have demonstrated a technique to chronically record from the DCN of non-human primates. Following a procedure to implant commercially-available electrode arrays, neuronal recordings were obtained for 2-5 months. We reproduced the known somatotopic organization of the constituent nuclei at the level of both field potentials and single units. A subset of units with RFs predominantly on the torso were found to produce regular spike trains with alpha-band frequencies. A novel neuronal stability analysis was developed that was specifically tailored to aspects of these recordings. We demonstrated that single DCN neurons could be tracked over multiple days. Finally, we quantified the stability of RFs and spiking regularity across sessions.

Prior studies of monkey DCN physiology have used acute recording techniques in conjunction with terminal experiments (Harris, Jabbur et al. 1965, Biedenbach, Jabbur et al. 1971, Hummelsheim and Wiesendanger 1985, Xu and Wall 1999, Witham and Baker

2011). Thus much of what is currently known about these nuclei in the primate is derived from anesthetized animals. This is surprising given that chronic recording techniques are not new and that the shallow depth of the DCN from the pial surface make them accessible by commercial electrode arrays (Rousche and Normann 1998). The only barrier to implanting these arrays in the DCN has, presumably, been the impression that surgical access was too difficult and that a chronic brainstem implant was too dangerous (Weber, Friesen et al. 2012). Despite the inherent risks, the monkeys, who were the first two from our laboratory to receive these implants, did remarkably well and the implants provided high-quality neural recordings.

We found that monkey DCN neurons have characteristic spiking patterns in response to stimuli within their RFs. The majority responded with a relatively irregular pattern (IR $\approx$ 1.0). A smaller group, revealed by a distinct second peak in the IR distribution, produced rhythmic responses with consistent ISIs (IR $\approx$ 0.3). Nonrhythmic and rhythmic firing patterns have been observed in similar proportions of DCN neurons in anesthetized rats (Sanchez, Reboreda et al. 2006). This and other studies found that the rhythmic DCN activity in rats occurred in the alpha/beta (8-30 Hz) frequency range (Panetsos, Nunez et al. 1998, Nunez, Panetsos et al. 2000), similar to what was observed here in monkeys. There is evidence that this rhythmic activity is not imposed by descending cortico-DCN projections or by ascending input but is instead due to intrinsic properties of DCN neurons. Regular, 11-Hz spiking by cuneate neurons has been observed in a rat *in vitro* slice preparation (Nunez and Buno 1999). Similar alpha-frequency spiking and subthreshold membrane potential oscillations have been observed in isolated, cultured DCN neurons

(Reboreda, Sanchez et al. 2003). This frequency-specific rhythmic activity may play an important role in readout by downstream circuits. In a prior study, we observed that a single electrical stimulus pulse delivered to the DCN can evoke a long-lasting, alpha-frequency rhythm in primary somatosensory cortex (Richardson, Weigand et al. 2015). How this intrinsically- or electrically-driven, bottom-up alpha rhythm interacts with top-down controlled alpha (Haegens, Handel et al. 2011) and how both impact perceptual performance (Haegens, Nacher et al. 2011, Ai and Ro 2014) are intriguing questions for future work.

In the neuronal stability analysis, we found that our novel feature, STF, was informative of unit identity when the IED was small (< 0.5 mm). Similarly, *in vitro* studies using high-density, multielectrodes arrays (IED = 60 μm) have used the STF (called the "electrical image" by these studies) to reveal structural patterns of axons and dendrites (Litke, Bezayiff et al. 2004, Li, Gauthier et al. 2015). In addition to propagation of activity along neurites, peaks in the STF in our study could arise from intranuclear connections or common extranuclear inputs. For example, single Pacinian corpuscle afferent fibers can divergently excite multiple DCN neurons (Ferrington, Rowe et al. 1986). The required spatial resolution to detect these peaks is likely dictated by the small size of neuronal processes and sparseness of connectivity. To the best of our knowledge, the present work is the first to use the STF/electrical image to quantify stability of chronic neuronal recordings. While plasticity could change this feature, the present work shows that it can be stable enough to provide a useful metric of neuronal identity when combined with other

metrics such as MSW. Provided electrode arrays of sufficient density are used, the analysis developed here could assess the stability of neuronal recordings anywhere in the brain.

Our technique is limited by a reliance on commercial electrode arrays that are, at present, suboptimal for interfacing with the macaque DCN. In particular, the IEDs of the arrays used in this study were not sufficient to access all five digit representations of the hand or foot, even if array placement was perfect. These representations have a total mediolateral extent of about 1 mm (Florence, Wall et al. 1989, Qi and Kaas 2006). Tight bundles of ultra-thin microwires may be a better choice for these compact nuclei. Another limitation is in neuronal recording stability. Over 50% of the neurons classified as stable (which were themselves a minority) were recorded for less than a week with the UEA and less than four days with the FMA. Thus both the neuronal yield and time horizon would be limited for studies of single-cell correlates of long-term processes such as learning- or lesion-induced neural plasticity. In gross dissection and histology in monkey B, there was evidence that the FMA slowly rotated about the rostrocaudal axis over time. We speculate that torque was produced by the wire bundle's nominal stiffness and its manipulation during implantation. Both of these factors could be refined to potentially improve recording stability.

By necessity, the neuronal recordings in this study were made with the untrained animals sedated. However, it is important to emphasize that our technique can provide chronic access to the DCN in awake, behaving monkeys. This creates the opportunity to vastly improve our understanding of the role of these nuclei in primate sensorimotor behavior. A number of new hypotheses regarding functional organization and information

processing in the DCN have been put forward recently using anesthetized or decerebrated animals (Witham and Baker 2011, Bengtsson, Brasselet et al. 2013, Niu, Ding et al. 2013, Jorntell, Bengtsson et al. 2014). With appropriate behavioral tasks, including active touch paradigms, these hypotheses can now be tested in awake monkeys. In addition, the implant enables chronic DCN microstimulation. We have begun testing whether the DCN would be a suitable target for encoding sensory information with microstimulation after spinal cord injury severs natural ascending input (Richardson, Weigand et al. 2015). This and future studies of awake monkeys detecting and discriminating electrical stimuli delivered through a chronic DCN implant should help elucidate the causal role of the DCN in perception.

Chapter IV: Somatosensory Encoding in Cuneate Nucleus Microstimulation: Detection of Artificial Stimuli

Adapted from IEEE Engineering in Medicine and Biology Society Conference 2016

Srihari Y. Sritharan, Andrew G. Richardson, Pauline K. Weigang, Ivette Planell-Mendez, Xilin Liu, Hongjie Zhu, Milin Zhang, Jan Van der Spiegel, and Timothy H. Lucas

4.1 Introduction

Somatosensation is critically lacking in demonstrations of neurally-controlled prosthetic arms in paralyzed individuals (Collinger, Wodlinger et al. 2012, Hochberg, Bacher et al. 2012). The result is motor performance well below what is needed for widespread clinical adoption of this technology (Bensmaia and Miller 2014). Prior work on providing artificial sensation through electrical stimulation of the brain has almost exclusively targeted primary somatosensory cortex (S1) (Fitzsimmons, Drake et al. 2007, O'Doherty, Lebedev et al. 2009, O'Doherty, Lebedev et al. 2012, Johnson, Wander et al. 2013, Tabot, Dammann et al. 2013, Zaaimi, Ruiz-Torres et al. 2013, Klaes, Shi et al. 2014, Dadarlat, O'Doherty et al. 2015, Kim, Callier et al. 2015). However, this may not be the optimal target due to an

inability of electrical stimulation to appropriately activate its distributed representations (Weber, Friesen et al. 2012). Alternative, up-stream sensory targets remain largely unexplored.

The cuneate nucleus (CN) in the dorsal brainstem is upstream of S1 in the somatosensory pathway, receiving primary afferent input from the upper body and projecting predominantly to the thalamus. Its supraspinal location makes it a suitable sensory encoding site for individuals with spinal cord injury. Furthermore, its compact representations may be more reliably activated artificially. Due to technical challenges, the primate CN has previously been accessed only acutely in anesthetized animals. Recently, our lab demonstrated the first successful chronic interface to the CN of macaques (Richardson, Weigand et al. 2015, Richardson, Weigand et al. 2016). This technique allows us to now characterize, with behavioral experiments, the percepts elicited by CN microstimulation.

In particular, the present study quantified the detectability of CN microstimuli in two rhesus macaques. We show that both animals could detect these artificial stimuli. We further document the learning curve to switch from detecting natural to artificial stimuli and the threshold current amplitude.

4.2 Methods

All procedures were approved by the University of Pennsylvania Institutional Animal Care and Use Committee. Two male rhesus macaques (*Macaca mulatta*), monkeys A and E, were trained on an active touch oddity task (ATOT) to quantify detection of vibrotactile

stimuli. On each trial, the monkeys moved their left hand to determine which of three actuators (Haptuator Mark II, Tactile Labs Inc.) was vibrating and responded by pressing the corresponding capacitive touch sensor behind the chosen actuator (Fig. 4.1). Only one actuator (i.e. the oddity), chosen pseudorandomly, was active on each trial and the monkeys had up to 10 s to make their choice. Additional capacitive touch sensors were integrated with the actuators both to record the sequence in which the motors were explored and to gate the vibration. The oddity actuator was only on when the sensor indicated the monkey was touching it. Correct responses were rewarded with food and all trials were followed by a 5-s intertrial interval.

Following initial training on this task, the monkeys underwent a sterile surgical procedure to implant a headpost to stabilize the head during the experimental sessions. The animals were then re-trained to perform the ATOT under head-fixed conditions. Next, a second sterile surgical procedure was performed to implant a 32-channel floating microelectrode array (FMA, Microprobes for Life Science) into the left CN, using a technique developed previously (Richardson, Weigand et al. 2016). The array had a 250-µm inter-electrode spacing and had platinum-iridium electrodes of four different lengths interspersed throughout the array (1.5, 2.0, 2.5, and 3.0 mm).

After implantation, electrophysiological sessions were conducted to verify the placement of the array in the CN. Punctate mechanical stimuli were delivered to the skin with a hand-held, force-sensing probe (REB7, Loadstar Sensors) while recording neuronal responses on the FMA (ZC32, PZ2, RZ2, Tucker-Davis Technologies). The site of maximal response for each recorded unit (i.e. the unit's receptive field) was identified. Finally, behavioral sessions

were conducted over several weeks. In these daily sessions, the monkeys performed the ATOT but with the vibrotactile stimulation replaced by CN microstimulation (0.2-ms/phase biphasic pulses, 100-Hz pulse frequency, 80-μA pulse amplitude unless noted otherwise; IZ2 stimulator, Tucker-Davis Technologies). Bipolar stimulation was delivered between pairs of electrodes with confirmed placement in hand or arm representations of the CN. As in training, the CN microstimuli were only delivered when the touch sensor signaled that the monkey was touching the pseudorandomly-chosen oddity location. The stimulus train lasted for as long as the touch was maintained, resulting in variable stimulus durations. Catch trials, in which no microstimulation was delivered, were included at random times in each session to evaluate chance performance on the task.

The location of the FMA in monkey A was confirmed to be in portions of the CN and the more medial gracile nucleus in a gross anatomical examination following euthanasia. No analysis of array location has been performed to date in monkey E as experiments are ongoing.

4.3 Results

Monkeys A and E were implanted chronically with a FMA in the left CN. To assess the location of the electrodes, receptive fields (RFs) of recorded units were identified. An example is shown in Figure 4.2. This unit responded maximally to force pulses delivered on the extensor surface of the left forearm. The response, with spike bursts at the onset and offset of the stimulus, was similar to that of rapidly adapting primary afferents. RFs were compiled across several sessions to identify a subset of the 32-electrodes in each monkey

that were in hand and arm representations of the CN. Microstimulation was restricted to these electrodes in the subsequent behavioral experiments.

The monkeys were trained on the vibrotactile version of the detection task: the ATOT. Following implantation and RF mapping, vibrotactile stimuli were replaced with microstimulation delivered to the CN. In the first few sessions following this switch in stimulus modality, the monkeys' detection performance in the ATOT was at chance levels. This suggests that CN microstimulation did not match the sensation of the vibrotactile input on which the monkeys were trained. In subsequent sessions, the animals' performance improved as they learned, through operant conditioning, to detect the artificial sensations produced by CN microstimulation. Monkey A had interruptions in the testing sessions making it difficult to assess the transition in performance from natural to artificial stimuli. However, monkey E showed a clear learning curve after the first introduction of CN microstimuli (Fig. 4.3). The first significant improvement in detection probability over chance occurred on the eighth daily session ($X^2(1) = .0156$). Plateau performance was seen by the tenth session.

After the initial learning phase, both monkeys performed the CN stimulus detection task consistently above chance (Fig. 4.4). Monkey A had an average post-learning detection probability of 0.56, a 68% increase over chance performance. Monkey E had an average post-learning detection probability of 0.59, an 80% increase. These probabilities were significantly higher than on catch trials (chi-squared tests, $p<0.05$), in which no stimulation was delivered and the monkey had to simply choose a random response.

Finally, in monkey E, an experiment was performed to identify the threshold amplitude for detection. On each trial, the amplitude of the oddity stimulus was chosen at random from eight values ranging from 10 μA to 80 μA. In addition, 10% of the trials were catch trials in which stimulus amplitude was 0 μA. The results indicate a clear threshold at about 45 μA (Fig. 4.5). Detection probabilities at current amplitudes of 50 μA and above were significantly different from the detection probabilities on catch trials.

4.4 Discussion

As we found in three previous macaques (Richardson, Weigand et al. 2015, Richardson, Weigand et al. 2016), the chronic brainstem implants in the two monkeys of this study provided long-term electrophysiological access to the CN without causing adverse neurological effects. The novelty of this study was in showing that both monkeys learned to detect microstimulation delivered to the CN.

Learning is not always required to detect artificial stimuli. Perceptions arising from natural vibrotactile stimulation of the fingers and artificial electrical stimulation of S1 can be indistinguishable when properly calibrated (Romo, Hernandez et al. 1998, Tabot, Dammann et al. 2013). Here, we made no attempt to calibrate the CN stimuli. The resulting detection learning curve matched those of similar, non-biomimetic approaches targeting S1. In particular, macaques have required 5-15 sessions for perceptual performance with S1 stimuli to significantly exceed chance (Fitzsimmons, Drake et al. 2007, O'Doherty, Lebedev

et al. 2009, O'Doherty, Lebedev et al. 2012). With CN stimuli, it took 8 sessions for monkey E.

Detectability of S1 stimuli is known to be dependent on stimulus parameters, including the amplitude, width, and frequency of the stimulus pulses (Kim, Callier et al. 2015). Here we explored the effect of stimulus amplitude on detection and found a threshold of 45 µA for 100 Hz stimulus trains. At this same pulse frequency and same 0.2-ms pulse width, a recent study found an average detection threshold of ~ 38 µA for S1 microstimulation (Kim, Callier et al. 2015). The difference may be accounted for by differences in pulse train duration, which also impacts detection thresholds in S1.

The present study provides the first assessment of percepts evoked by microstimulation of the CN. However, additional work will be needed to determine whether the CN is a viable encoding site for sensorimotor prostheses. First, it will be critical to assess the discriminability of CN microstimuli, not just the detectability. Second, it will be important to directly compare, in the same subjects, the perceptual performance of encoding in the CN versus downstream targets such as the ventral posterolateral nucleus of the thalamus (Heming, Choo et al. 2011, Song and Semework 2015) or S1. Does activation of the compact, simpler representations of the CN lead to more intuitive percepts than S1? Does electrical current spread make it difficult to independently activate the closely spaced CN representations? Ultimately, are the increased risks associated with a brainstem implant offset by superior perceptual performance relative to a cortical target? The results presented here suggest it is both possible and imperative to pursue these questions.

Chapter V.I: Somatosensory Encoding with Cuneate Nucleus Microstimulation: Effects on Downstream Cortical Activity

Adapted from IEEE Conference on Neural Engineering 2015

Andrew G. Richardson, Pauline K. Weigand, Srihari Y. Sritharan, and Timothy H. Lucas

5.1.1 Introduction

Continuous somatosensory feedback from the mechanoreceptors of the skin, muscles, and joints is necessary to guide accurate finger movements (Johansson and Flanagan 2009). In the absence of sensation, dexterous hand movements are lost. Similarly, motor neuroprostheses engineered to restore hand movements in paralyzed individuals provide only limited benefit when somatosensory feedback remains unavailable (Gilja, Chestek et al. 2011). In light of this issue, there is interest in replacing lost sensory pathways by

encoding sensory information directly in the brain with electrical stimulation (Weber, Friesen et al. 2012).

In the case of paralysis due to spinal cord injury (SCI), potential sensory encoding targets include the cuneate nucleus (CN) of the brainstem, ventral posterior lateral nucleus of the thalamus, and primary somatosensory cortex (S1). The latter site has been the preferred location for sensory encoding to date, due to its surgical accessibility and well-studied physiology (O'Doherty, Lebedev et al. 2011, Johnson, Wander et al. 2013, Tabot, Dammann et al. 2013, Zaaimi, Ruiz-Torres et al. 2013). However, work toward auditory and visual neuroprostheses has shown that stimulating cortical sensory areas is generally less effective in evoking intelligible percepts than stimulating more peripherally along the sensory neuraxis (Weber, Friesen et al. 2012). Therefore, our group is focused on microstimulation of the CN to restore sensation after SCI. Towards this goal, we have recently demonstrated the first successful chronic implant of a microelectrode array into the primate CN, providing months of stable access to this brainstem nucleus (Richardson, Weigand et al. 2014).

In this paper, we characterize the downstream neural activity evoked by CN microstimulation. In particular, we quantified the temporal dynamics of S1 excitation and inhibition in response to single and paired stimulus pulses in the CN. Excitability of S1 is known to be correlated with perceptual performance (Haegens, Nacher et al. 2011). Thus, the results should inform the design of CN stimulus patterns for evoking salient percepts.

5.1.2 Methods

A sterile surgical procedure was performed in one male rhesus macaque (*Macaca mulatta*) to implant two, 32-channel floating microelectrode arrays (FMAs, Microprobes for Life Sciences). The first FMA was implanted in the brainstem, just lateral to the obex, to access the right CN. The second FMA targeted the finger representations of left S1. The CN and S1 FMAs had interelectrode spacings of 250 and 400 µm, respectively. Both arrays had electrodes of four different lengths (2.0, 2.5, 3.0, and 3.5 mm), interleaved throughout the arrays.

The monkey was untrained and thus each experimental session was conducted with the animal under light sedation (4 mg/kg ketamine and 0.05 mg/kg dexdomitor). Beginning three days after the implant surgery, the sedated sessions were conducted twice a week for six weeks. Initial sessions were devoted to identifying neuronal receptive fields with the goal of finding sites on both arrays with homologous finger representations. In these mapping sessions, mechanical stimuli were delivered to the periphery with a hand-held, force-sensing probe (REB7, Loadstar Sensors) while recording neuronal responses on both FMAs (ZC32 headstages, PZ2 preamplifier, RZ2 processor, Tucker-Davis Technologies). The probe was moved to the patch of skin for which the neuronal response was maximal. That patch was designated as the neuron's receptive field. In subsequent sessions, bipolar electrical pulses (monophasic, 0.2-ms pulse width) were delivered to pairs of electrodes on the CN FMA (IZ2 stimulator, TDT) while recording the response from S1.

At the conclusion of the experiments, the animal was transcardially perfused with paraformaldehyde and a histological analysis was performed to identify the electrode locations. The S1 FMA was shown to be in area 3b. Due to the insertion angle, there was

some variability in the laminar location of each of the four electrode lengths. The laminar designations for these four lengths account for this variability. The surgery, electrophysiological experiments, and perfusion were approved under protocol no. 804540 by the University of Pennsylvania Institute for Animal Care and Use Committee.

5.1.3 Results

Two FMAs were implanted chronically in the right CN and left S1 of a macaque for six weeks. In initial recording sessions, receptive fields (RFs) of single unit activity (SUA) were mapped. On the S1 FMA, all SUA was responsive to mechanical stimulation of the fingers. Digit 3 RFs were found medially and digit 2 RFs were found laterally (Fig. 5.1.1, top). This corresponds with the known somatotopic organization of S1. On the brainstem array, lower and upper body RFs were found medially and laterally, respectively (Fig. 5.1.1, bottom). This corresponds with the known relative brainstem location and sensory afferent distribution of the gracile and cuneate nuclei. Units responsive to mechanical stimulation of digits 2 and 3 were found on one of the most lateral electrodes of the CN FMA. Thus homologous finger representations were present on the two arrays.

Next, single-pulse electrical stimuli were delivered to the brainstem array while recording the wide-band (0.35 Hz to 7.5 kHz) neural response in S1. When stimulating the CN finger representation, large evoked potentials (Canolty, Ganguly et al.) were observed throughout the S1 FMA (Fig. 5.1.2A). The EPs varied systematically across the four different length electrodes present on the FMA (Fig. 5.1.2B), which corresponded to different cortical laminae. The peak response, occurring at 6.5 ms (dashed line in Fig. 5.1.2B), exhibited a polarity inversion across the recording depth (Peterson, Schroeder et al.

1995). A nearly identical distribution of S1 EPs, but with peak at 10.5 ms, was found when stimulating the median nerve transcutaneously at the wrist (data not shown). The EPs were sensitive to alignment of the brainstem and S1 representations. Stimulating 0.5 mm medial, in an area with torso RFs, yielded no evoked response in the S1 finger area (Fig. 5.1.2C). All following results were obtained from stimulating the digit CN site.

In addition to the EPs, we analyzed S1 multiunit activity (MUA) and SUA evoked by CN microstimulation. A representative response recorded on one S1 electrode (lamina 3) is shown in Figure 5.1.3. The initial negative peak in the EP corresponded with increased MUA and SUA. This initial cortical excitation was followed by an inhibitory phase lasting from about 12 to 50 ms. Both MUA and SUA were suppressed below pre-stimulus levels during this phase. After the inhibition, the MUA and SUA response rebounded to a more prolonged, gradually-decreasing excitation lasting beyond 250 ms. Within this excitatory phase were small rhythmic peaks of increased excitation at about 60, 155, and 240 ms. Interestingly, the frequency of these peaks is within the alpha band (8-14 Hz), a prominent rhythm found in spontaneous cortical field potentials and thought to be part of a mechanism by which sensory information is attended or ignored (Haegens, Nacher et al. 2011).

A closer look at this stimulus-induced, rhythmic excitation revealed two features. First, it was laminar specific. The long-lasting excitation reflected in the MUA was most prominent in the peri-granular laminae (3/4 and 4/5) (Fig. 5.1.4, left column). Second, the rhythmic peaks of excitation were stimulus-amplitude dependent. The rhythm grew progressively more pronounced as the stimulus intensity was increased from 25 µA (Fig. 5.1.4, top row), to 50 µA (middle row), to 75 µA (bottom row).

The frequency content of the rhythm can be seen in the scaleograms (Fig. 5.1.4, right column). The first few cycles were at around 10Hz (as in Fig. 5.1.3). After 0.3 s, the rhythm had a slightly higher frequency (13 Hz). Note that while the rhythmic excitation was stimulus-amplitude dependent, the duration of the long-lasting increase in MUA was not; it lasted until 0.8 s for all intensities.

Finally, the CN-evoked excitability changes in S1 were further explored with pairs of CN stimuli. No EP was seen in response to a second pulse when it followed the first pulse by 20 ms (Fig. 5.1.5A, blue). When the interpulse interval (IPI) was 35 ms, an EP following the second pulse was seen but it was less than half its normal amplitude (Fig. 5.1.5A, cyan). With a 50-ms IPI, the second-pulse EP was a similar amplitude to the first and broader (Fig. 5.1.5A, green). These results demonstrate an inhibitory period following the first pulse, which matched the time course of the inhibitory phase seen in the MUA and SUA in Figure 5.1.3.

The late, prolonged increase in MUA seen in Figure 5.1.4 was largely unaffected by a second pulse provided the IPI was 50 ms or less (Fig. 5.1.5B). However when a second pulse occurred at 100 ms, when the MUA was elevated due to the first pulse, it provoked the same type of rhythmic excitation seen earlier (Fig. 5.1.5B, bottom). Thus this rhythmic activity could be evoked either with high intensity of a single pulse or appropriate timing of multiple pulses.

5.1.4 Discussion

The results show that a single stimulus pulse to the CN has a complex and long-lasting effect on S1. There were three main phases of this effect: fast excitation (6-12 ms relative to stimulus onset), inhibition (12-50 ms), and rebound excitation (50-800 ms). The fast excitation phase likely reflects the disynaptic, lemniscal thalamic activation of excitatory interneurons of the S1 granular layer (lamina 4). The subsequent rapid depolarization of the peri-granular pyramidal neurons (laminae 3 and 5), and corresponding hyperpolarization of their superficial dendrites (lamina 1), accounts for the depth-dependent polarity inversion of the ~7ms EP peak (Kulics and Cauller 1986, Peterson, Schroeder et al. 1995).

The inhibition phase could be attributed to disynaptic, lemniscal thalamic activation of inhibitory interneurons of the S1 granular layer, which then inhibit the peri-granular pyramidal neurons. This type of feedforward inhibition is a common feature of cortical circuits receiving sensory thalamic input (Swadlow 2003). A similar sequence of fast excitation and subsequent inhibition due to somatosensory stimuli has been see in rabbit S1 (Swadlow and Gusev 2000), monkey S1 (Gardner, Hamalainen et al. 1984), and even human motor cortex (Tokimura, Di Lazzaro et al. 2000). However, inhibition at the level of the thalamus rather than, or in addition to, S1 cannot be ruled out (Poggio and Mountcastle 1963).

The rebound excitation phase can be attributed to intrinsic, postinhibitory rebound properties of thalamo-cortical, cortical, and corticothalamic neurons and recurrent excitation within this network (Grenier, Timofeev et al. 1998). There is evidence that the rebound is initiated by the intrinsic properties of thalamocortical neurons but the sustained S1 excitation, lasting 750 ms in the present work, is due to intracortical circuits (Grenier,

Timofeev et al. 1998). The alpha-band, rhythmic peaks riding on top of the sustained excitation are likely a network-level effect of the thalamocortical loops.

A limitation of the present study is that the effects of CN microstimulation on S1 were documented in a sedated, rather than awake, monkey. Anesthesia is known to affect, for example, the duration of post-stimulus inhibition (Poggio and Mountcastle 1963). However, the time course of the effects was similar to peripherally-evoked (Gardner, Hamalainen et al. 1984) and thalamic spike-driven (Swadlow and Gusev 2000) S1 activity in awake animals.

The implications for a sensory neuroprosthesis using CN microstimulation are two-fold. First, feedforward inhibition may limit the effective stimulus frequency to about 20 Hz. Second, postinhibitory rebound excitation may alter the perceptual threshold for stimulus frequencies in the range of about 1 to 10 Hz. Of course the transformation from S1 activation to perception almost certainly has its own dynamics that may or may not dominate those reported here. The ultimate test of the strategy requires awake, behaving animals detecting and discriminating CN stimulation patterns. However, the present work provides a physiological basis for the initial choice of those patterns and a mechanistic framework with which to interpret how different patterns influence perceptual performance.

Chapter V.II: Entrainment of Primate Somatosensory Cortical Neurons to Spontaneous and Evoked Spindle Oscillations

5.2.1 Introduction

Oscillatory activity in neural networks and its role in sensory mechanisms have been of increasing interest in recent years. The intrinsic ability for single neurons to form both self-governed and externally driven oscillator networks with multiple resonant frequencies suggests that these neural oscillations can encode temporal and sensory information and have direct causal impact on cortical computations [(Buzsaki and Draguhn 2004), *(Singer 2017), (Canolty, Ganguly et al. 2010)*]. Under various scenarios, prolonged periods of hyperpolarization in the thalamus and cortex lead to periodic rebound spiking in both regions, due to the inherent property of inhibitory corticothalamocortical feedback loops. As these rhythms are preserved across mammalian species [(Buzsaki, Logothetis et al. 2013), *(Singer 2017)*], a variety of explanations have been suggested for their functional role, ranging from sensory amplification and gating [*Grenier, Timofeev et al. (1998)*] to being a marker of executive control disengagement [*Haegens, Nacher et al. (2011)*]. Corticothalamocortical loops are present in nearly every sensory system in cortex, but the associated rhythms are reported to be strongest in the somatosensory system [*Hsiang-Tung (1950)*], even though there is no bodily physiological sign associated with the presence of the rhythm in the CNS. The experiments in this paper are thus directed towards two such network-wide rhythms present in the primary somatosensory cortex: sleep spindles and somatosensory evoked spindles. These two rhythms are often studied in tandem in sensory

cortex [(Contreras and Steriade 1996), (Contreras, Destexhe et al. 1996), (Hsiang-Tung 1950)], due to the ability of single somatosensory stimuli to evoke prolonged oscillations that are observably similar to their spontaneous, sleep spindle counterpart.

Sleep spindles have been thoroughly studied during the last several decades [(Adrian 1941), (Hsiang-Tung 1950), (Destexhe, Contreras et al. 1994), (Contreras, Destexhe et al. 1996, Contreras and Steriade 1996), (Contreras, Destexhe et al. 1997), (Haegens, Nacher et al. 2011)]. The depth of literature can be attributed to fact that some anesthetics intensify spindle activity, allowing for prolonged study *in vivo*. Spindles are defined as rhythmic waves (10-16 Hz) that occur spontaneously during early stages of sleep which originate in the thalamus and are further potentiated by input from the cortex. These sleep spindles have a marked waxing and waning envelope, which is the result of gradual recruitment of units after a release from prolonged hyperpolarization under slow-wave cortical depression, followed by a gradual dropout of the units as the network reverberation returns to a resting state [(Contreras and Steriade 1996)].

Somatosensory evoked spindles in contrast are generated following a peripheral or thalamic stimulus along the medial lemniscal pathway. In some literature, this has been documented under the name 'alpha rhythm', but describes the same phenomenon [(Andersen, Andersson et al. 1968)]. A single electrical stimulus to the median nerve elicits primary 'fast' responses in S1 from monosynaptic potentials from thalamus and secondary somatosensory regions, documented as p10 and p20/25 in some literature [*(Peterson, Schroeder et al. 1995), (Gardner, Hamalainen et al. 1984)*]. This is immediately followed by strong feedforward inhibition from the thalamus onto S1 [(Andersen, Andersson et al. 1968)]. The eventual release from this inhibition causes periodic 'slow' rebound excitation

in the S1 local field potential oscillating between 10 and 16 Hz, until gradual unit dropout returns the potential to a resting state. This rhythm is of particular interest due to the fact that the resulting thalamocortical reverberation lasts several thousands of times longer than duration of the single pulse to the median nerve itself, providing potential evidence as a mechanism for sensory amplification.

In the experiments that follow in this paper, we find in two sedated, chronically implanted monkeys that the same single units in S1 would fire during both spontaneous spindles and evoked spindles at similar but differing LFP frequencies and unit firing rates; this begs the question if their network role in each scenario is related or similar in some way. Previous focus in the literature has delved into the origin and behavior of the late components in the evoked potential [(Adrian 1941), (Hsiang-Tung 1950), (Gardner, Hamalainen et al. 1984), (Jones, Allison et al. 1992), (Steriade, Gloor et al. 1990)]; however spike phase information elucidating the network role of local single unit activity in S1 in both types of spindles has not been previously explored in high detail.

The spike phase within a spindle is under the influence of both the underlying network dynamics and any external inputs to the single unit, thus forming a representation of encoded information and network role [(Buzsaki and Draguhn 2004)]. Phase encoding was first explored in depth in the hippocampal place cell literature [(O'Keefe and Recce 1993)], but has not been previously investigated in spontaneous or evoked spindles.

In this study, we aim to characterize the frequency and phase relationships between the local field potential, multiunit and single unit activity during spindles in primates with chronic electrode implants under ketamine anesthesia.

5.2.2 Methods

General surgical methods

A sterile surgical procedure was performed in two male rhesus macaque (Monkey G - Macaca mulatta, Monkey M - Macaca cynamologus) to implant 32-channel floating microelectrode arrays (FMAs, Microprobes for Life Sciences), one array in Monkey M and two arrays in Monkey G. In both Monkey G and Monkey M, the first FMA targeted the finger representations of primary somatosensory cortex (S1), in the left hemisphere in Monkey G, and in the right hemisphere in Monkey M. In Monkey G, the second FMA was implanted in the brainstem, just lateral to the obex, to access the right cuneate nucleus (CN). The CN and S1 FMAs had interelectrode spacings of 250 and 400 μm, respectively. All three arrays had electrodes of four different lengths (2.0, 2.5, 3.0, and 3.5 mm), interleaved throughout the arrays. At the conclusion of the experiments, Monkey G was transcardially perfused with paraformaldehyde and a histological analysis was performed to identify the electrode locations. The S1 FMA was shown to be in area 3b. Due to the insertion angle, there was some variability in the laminar location of each of the four electrode lengths. The laminar designations for these four lengths account for this variability.

Experimental procedures

These monkeys were untrained and thus each experimental sessions were either conducted with the animals under light sedation (4 mg/kg ketamine and 0.05 mg/kg dexdomitor) or conducted overnight across full 24+ hour sessions using custom, wearable neural recording devices developed by Penn Electrical Engineering collaborators [(Liu, Zhang et al. 2015)],

sampling at 1kHz. Beginning three days after the implant surgery, the sedated sessions were conducted twice a week for six weeks in Monkey G and conducted between once and twice a week for thirty one weeks in Monkey M. These time periods were selected to maximize total number of sedated recordings during the lifetime of the electrode arrays.

Initial sessions were devoted to identifying neuronal receptive fields with the goal of finding sites on all three arrays with homologous finger representations. In these mapping sessions, mechanical stimuli were delivered to the periphery with a hand-held, force-sensing probe (REB7, Loadstar Sensors) while recording neuronal responses on all three FMAs (ZC32 headstages, PZ2 preamplifier, RZ2 processor, Tucker-Davis Technologies) sampling at 24.4kHz. The probe was moved to the patch of skin for which the neuronal response was maximal. That patch was designated as the neuron's receptive field.

Cortical recordings from transcutaneous nerve stimulation

In subsequent sessions in both animals, bipolar electrical pulses (parameters?) were delivered transcutaneously to the contralateral and ipsilateral median nerve (DigiStim stimulator) while recording the responses from S1 and CN. In Monkey G, additional CN stimulation sessions were performed by delivering bipolar electrical pulses (monophasic, 0.2-ms pulse width) to pairs of electrodes on the CN FMA (IZ2 stimulator, Tucker-Davis Technologies) while recording the response from S1.

Data analysis

The local field potentials (LFP) and/or evoked potentials (EP) in sedated sessions were extracted as the wideband signal from the array recordings from each electrode channel.

For coherence calculations, the LFP and EP were second-order lowpass filtered under 300 Hz to eliminate contributions from single and multiunit activity.

Multiunit activity (M) was calculated from the wideband signal by 4^{th} order bandpass filtering for the spikeband between 300 and 6000 Hz, clipping potential values beyond two standard deviations [(Kreiman, Hung et al. 2006)], rectifying the signal and lastly 2^{nd} order lowpass filtering below 100 Hertz.

Single unit activity (SUA) was spike sorted offline using automatic PCA analysis and K-means clustering (OpenSorter, Tucker-Davis Technologies). Clusters were subsequently curated manually to excise outlier spikes and resolve false positives and false negatives in the detected clusters. Single-unit isolation quality was determined by estimating false-positive rates, false-negative rates and absolute refractory period violations [(Hill, Mehta et al. 2011)] (see Supp. Figure 5.2.1).

LFP spindles were detected using $P_{episode}$ analysis [(Caplan, Madsen et al. 2001)], which uses a one-dimensional continuous wavelet transform to find bouts of high-power oscillatory activity in the spindle band (10-20 Hz) with a minimum of three consecutive cycles.

Spike field coherence (SFC) was evaluated using LFP or EP windows of -500 to 500ms centered on every spike in the SUA. Median nerve stimulus artifacts in the EP contained in these windows were blanked between -50 to 50ms centered on each stimulus. Coherence was then calculated as the ratio of the power spectrum of the spike-triggered LFP average over the spike-triggered LFP power spectrum [(Fries, Roelfsema et al. 1997)].

Multiunit field coherence (MFC) was evaluated in the evoked case by considering post-stimulus windows of 20 to 800ms in the MUA and EP for every stimulus instance. Due to the temporally sparse nature of spindle activity in the spontaneous spindle experiments, MFC in the spontaneous case used local windows of 20 to 800ms in the MUA following every spike in the SUA. This was equivalent to using single unit spikes as a pseudo-trigger instead, as opposed to the median nerve stimuli in the aforementioned evoked case. In both cases, the MFC was calculated for all windows using Welch's Magnitude Squared Coherence Estimate to find the coherence for frequency values between 5 and 25Hz.

LFP and EP phase was calculated by bandpass filtering the signal in the relevant frequency range, performing a Hilbert transform on the filtered signal, and then taking the complex angle of the transform. Preferred phase angle and magnitude for a set of spike phases was calculated by finding the resultant vector of the entire set. Each individual spike phase was considered to have a magnitude of one. Significantly unimodal single units were determined by performing a Rayleigh test on the set of all spike phases for that unit and retaining single units whose *p*-values were less than 0.05.

LFP and EP cycle indexes were determined by finding all locations in the Hilbert phase where the angle would abruptly transition from $+\pi$ to $-\pi$, indicating the beginning of a new cycle. Individual cycle frequency was calculated by inverting the time length of each 2π cycle in seconds.

Ethical Considerations of Animal Care

The surgery, electrophysiological experiments, and perfusion were approved under protocol no. 804540 by the University of Pennsylvania Institute for Animal Care and Use Committee.

5.2.3 Results

Chronic microelectrode arrays were implanted in left S1 in two monkeys (G and M). The 2- to 3.5-mm length electrodes targeted neural activity in area 3b [(Kim, Callier et al. 2015)]. Correspondingly, receptive field (RF) mapping found that the isolated neurons were most responsive to tactile inputs from the proximal and distal glabrous skin of digits 1, 2, and 3.

Spontaneous spindles during sleep and sedation

We began by identifying natural S1 spindle activity and comparing it to spindle-like activity during sedation. For the former, we recorded S1 local field potential (LFP) activity during free behavior in the animal's home cage using a custom battery-powered, head-mounted recording device [(Liu, Zhang et al. 2015)]. Spontaneous spindles were detected using $P_{episode}$ analysis [(Caplan, Madsen et al. 2001)] as bouts of high-power oscillatory activity in the 10-20 Hz band with a minimum of three consecutive cycles. A representative S1 spindle is shown in Fig. 5.2.1A, exhibiting a well-characterized waxing and waning envelope [(Contreras and Steriade 1996)]. Across a typical free-behavior recording, spindle activity was highest during putative sleep from the hours of 7:00PM to 7:00AM during the mandated lights-off period (Fig. 5.2.1B). 65% of the total spindle episodes occurred during the lights-off hours. Natural sleep spindles had a frequency of about 14 Hz, as indicated by the peak at that frequency in the power spectrum of the overnight recording (Fig. 5.2.1C, black). Measuring the power spectrum of the spindle episodes in isolation demonstrated an even more pronounced peak at 14 Hz (Fig. 5.2.1C, green). To quantify the prominence of

these peaks, the fold-over-baseline was calculated by dividing out the baseline, modeled as fitted pink noise, from the power spectra. A 1.25-fold and 2.6-fold increase over baseline was observed at 14 Hz for the entire LFP and spindle episodes, respectively.

The limited sampling rate (1 kHz) of our wearable recording device prevented acquisition of unit activity. To study S1 neuronal activity during spindles with conventional tethered recordings, we relied on the sleep-like state provided by ketamine-dexmedetomidine sedation, regarded as an optimal anesthetic for replicating sleep spindles characteristics [(Timofeev, Contreras et al. 1996)]. During sedation, spontaneous spindles were periodically seen in the LFP (Fig. 5.2.1D). Again a peak in the LFP power spectrum was seen at 14 Hz with an additional peak at 30 Hz in the gamma band (Fig 5.2.1E). The prominence of the 14 Hz peaks were 1.75-fold and 2.4-fold over baseline for the LFP and spindle episodes, respectively. The presence of the additional gamma-band peak in the LFP (2.0-fold over baseline) is a known effect of ketamine in sensorimotor cortex [(Shaw, Saxena et al. 2015)].

To quantify the similarity between spindles recorded during sleep and sedation, we computed the peak frequency, duration, and peak power for approximately 13,000 sleep episodes and 4,000 sedation episodes. Due to the large difference in sample sizes, Hedges' g for corrected effect size was used to quantify the difference between the probability distributions [*(Hedges 1981)*]. Spindle frequency was moderately effected by brain state ($g = 0.66$), with the frequency during sedation having a wider distribution and lower mean (Fig. 5.2.1F). Brain state had only a small effect on spindle duration ($g = 0.27$), with slightly smaller durations on average during sedation (Fig. 5.2.1G). Finally, brain state had a large effect on spindle peak power ($g = 1.44$), with higher power seen in sedation. Indeed,

dexmedetomidine is known to induce strong cortical spindle oscillations [*(Purdon, Sampson et al. 2015)*]. The results demonstrate that the S1 spindles observed during sedation are not identical to those during natural sleep particularly with regard to amplitude, but they are relatively similar in frequency and duration.

Entrainment of S1 neurons to spontaneous spindles

Having characterized the sedation model of S1 spindle activity, we next analyzed the extent to which S1 neurons were entrained to this spontaneous LFP rhythm. Qualitatively, we found that each spindle oscillation was accompanied by an increase in multiunit activity (MUA) (Fig. 5.2.2A, top and middle). The same was generally true at the level of single unit activity (SUA), although there was greater variability in the activity increase across spindle cycles (Fig. 5.2.2A, bottom). To quantify entrainment, we calculated coherence between neuronal activity and the LFP. In the case of MUA, the magnitude squared coherence was estimated and averaged across all S1 channels in the array. In the case of SUA, spike-field coherence was calculated as the ratio of the power spectrum of the spike-triggered LFP average over the spike-triggered LFP power spectrum [(Fries, Roelfsema et al. 1997)]. In both cases, the coherence spectrum typically showed a peak between 15 Hz, with the population mean coherence and 95% confidence intervals plotted in Fig. 5.2.2B, C.

As evident from Figure 5.2.2C, S1 neurons could be differentially recruited across cycles of a spindle episode, resulting in relatively low coherence values (< 0.15). As an alternative analysis we assessed the explicit relationship between spike times and the phase of spindle cycles. The latter was estimated using the Hilbert transform. We found that the distribution of spindle phases at spike times was typically not uniform (Fig. 5.2.2D),

suggesting that the S1 neuronal activity was entrained by the rhythm. Across the population, the spike-phase distribution was found to be significantly unimodal for 87% of S1 units (Rayleigh test, $p < .05$). The preferred spindle phase of SUA was concentrated in a range from about -60 to 30 deg relative to the negative peak of the spindle cycle (Fig. 5.2.2E). Unimodality (i.e. depth of tuning) was greatest for units that tended to fire prior to the peak (Fig. 5.2.2E). The population mean preferred phase, weighted by tuning depth, was –11 deg prior to the spindle peak. Thus cortical neuronal activity was strongly modulated by the spontaneous spindle rhythm and, with spiking activity leading the cycle peak, a subset of the network may in fact be involved in its generation [(Singer 2017)].

Entrainment of S1 neurons to evoked spindles

In addition to occurring spontaneously, spindle-like activity can be evoked by natural tactile or artificial electrical activation of peripheral nerves and subcortical somatosensory nuclei [(Adrian 1941), (Hsiang-Tung 1950), (Contreras and Steriade 1996)]. Therefore, using transcutaneous median nerve stimulation at the level of the wrist in the sedated monkeys, we analyzed evoked spindles and compared the entrainment of S1 unit activity to that found previously for the spontaneous rhythm. Contralateral median nerve stimulation produced a short-latency evoked potential (EP) in S1 followed by a rhythmic series of long-latency deflections in the stimulus-triggered LFP average (Fig. 5.2.3A-C, top). The initial negative peak in the EP occurred at about 10.5 ms [*(Peterson, Schroeder et al. 1995)]* and corresponded with a large phasic increase in MUA and SUA (Fig. 5.2.3A-C, middle and bottom). This excitatory phase was likely produced by the direct, trisynaptic activation of S1 via the dorsal column-medial lemniscus pathway. Similarly, the series of rhythmic long-latency negative peaks in the

EP corresponded with increases in MUA and SUA. This evoked rhythmic neuronal activity has been previously described as the product of reverberating cortico-thalamic circuits [(Adrian 1941), (Hsiang-Tung 1950)], similar to the mechanism underlying spontaneous spindles although with a peripheral rather than cortical genesis [(Contreras and Steriade 1996)]. In the population of all evoked oscillations, we find that the mean power spectrum (Fig 5.2.3D) shows a peak at a lower frequency (~ 10 Hz) than the spontaneous case. This is further evidenced in Figure 5.2.3E where the fold-over-baseline from fitted pink noise demonstrates a downward shift in the peak frequency in the evoked case.

Next, we analyzed entrainment of SUA to these evoked spindles using the same set of neurons as in the spontaneous analysis. Following the previous procedure, we calculated the MUA-LFP (Fig. 5.2.4A) and SUA-LFP (Fig. 5.2.4B) coherences for the evoked data from both monkeys. These population analyses showed bimodal peaks in maximal coherence around 10 and 14 Hz across all units and channel in both the MUA and SUA coherence, with the peak at 10 Hz having higher coherence. Thus the entrainment frequency was similar to the spontaneous rhythms but lower in the evoked case. Finally, we analyzed the relationship between spikes times and the evoked spindle phase. Again, the distribution of spindle phase at spike times was typically unimodal (Fig. 5.2.4C). However, in contrast to the spontaneous case, the majority of units with significantly unimodal phase distributions had a preferred phase after the spindle peak, with 76.5% of units in monkey M and 96% of units in monkey G entrained to a phase between 0 and +90 deg (Fig. 5.2.4D). The population mean preferred phase was 25 and 34 deg after the spindle peak for monkey M and G, respectively.

Comparison of S1 spike phase dynamics

To further highlight the contrast in entrainment to the spontaneous and evoked rhythm, the preferred phase in each case was plotted for each single unit (Fig. 5.2.5A). The lagging spiking activity of S1 neurons suggests that the cortical neurons were being driven by the evoked rhythm rather than playing a causal role in its genesis. By comparing the two directly, we see that the difference in population preferred phase is a shift of +40 degrees. If we consider a restricted set of the top 10% of neurons (selected by ranking their depth of entrainment in both spindles types), the phase shift is seen to be as large as +60 degrees.

This phase difference can be seen in a time domain analysis as well. The spike triggered averages of the spontaneous and evoked spindle spikes in Figure 5.2.5B show a peak-to-peak difference of approximately 10 milliseconds. This is numerically consistent with the phase difference between +40 to +60 degrees seen in Figure 5.2.5A if we assume a fundamental frequency of 14Hz.

Next, we addressed the possible underlying causal variables of this phase difference. In hippocampal literature [(O'Keefe and Recce 1993), (Hafting, Fyhn et al. 2008)], firing rate is known to modulate LFP spike phase in place cells, causing the well-described phase precession phenomenon. To address the possibility that firing rate is controlling the spike phase, we plotted the difference in mean firing rate between spontaneous and evoked sessions against the difference in phase, for each single unit individually (Fig. 5.2.5D). We found that the means of both the difference in spindle phase and the difference in spikes per second were each individually significantly greater than zero (t-test, $p<.05$). To elucidate this further, we performed linear regression analysis to explore the correlation of firing rate and phase, however there was no significant linear

correlation, with an R^2 value of 0.002. Thus, while the phase and firing rate are both independently higher in the evoked case, the data indicates it is unlikely that the cortical spindles are operating in a firing-rate modulated fashion as previously seen in hippocampus.

This motivated us to consider other potential modulating factors behind the phase difference seen between these spindle types. With the knowledge that spontaneous and evoked spindles have differing waxing and waning amplitude envelopes that evolve intraspindle [(Contreras and Steriade 1996)], we explored the possibility of differing intraspindle phase phenomena that also evolve throughout its duration. Due to the fact that spindles frequency and cycle count varied considerably across episodes and sessions, we opted to do use spike phase per spindle cycle instead of per absolute or relative time in seconds.

First, spindle regions were detected within the field potential, which were then subdivided further into individual spindle cycles. In the spontaneous case, we used $P_{Episode}$ detection to find the initial spindle episodes. In the evoked case, we considered post-stimulus windows of 80 to 900 milliseconds, which were dynamically downsized to find the exact initial spindle length for each individual stimulus, by using an offline preliminary Hilbert Transform. The lower end of this range was chosen to avoid interactions with p25 deflections in the evoked potential, which source from secondary somatosensory regions in cortex and are not commonly considered to be part of evoked spindles [(Gardner, Hamalainen et al. 1984)]. Lastly, stim trials that did not evoke a spindle (power spectrum peak outside the range between 5 and 20 Hz) were eliminated from the dataset. In both cases, these spindle regions were then bandpass filtered from 5 to 20 hertz and underwent

a Hilbert transform to determine and number the individual cycles from *1* to *N* for each spindle.

Single unit spikes were then assigned to their respective cycle number, and preferred spike phase for each cycle was plotted to visualize the evolution of phase across subsequent cycles (Fig. 5.2.5C). Spindles have varying numbers of total spindles, and thus high cycle numbers beyond which spike counts were too low or hit zero were eliminated from the study. The preferred phase for all cycles in the spontaneous case (Fig 5.2.5C, blue) was negative and consistently between -30 and 0 degrees. There is additionally no evolving phase change seen across cycles in spontaneous spindles. In contrast, the evoked spindles had positive preferred phases for all cycles (Fig 5.2.5C, red). While the jitter in preferred phase in the evoked cycles is higher than its spontaneous counterpart, this likely due to the greater amount of spontaneous spindle data, resulting in a more stable average than the evoked case.

These results indicate a number of time-domain and frequency-domain differences between spontaneous and evoked spindles that extend beyond the observations seen in previous literature, and point to a potential anatomical or functional difference in the underlying network.

5.2.4 Discussion

The experiments presented in this paper were aimed to analyze spontaneous spindles and evoked spindles under sedation as a model for thalamocortical loops involved in somatosensory processing.

In this study, the same single units in the array were seen entrained to similar central frequencies between 10 to 16 Hz in both spontaneous spindles and evoked spindles, which may implicate the existence of a common underlying neural network between sleep spindles and evoked sensorimotor alpha rhythms. Such a common network could provide confidence for the further study of the role of spontaneous spindles in somatosensory processing, such as sensory gating or amplification during sleep. The results show however, that the differing phase and frequency relationships between the two scenarios reflect a higher likelihood that these single units are either occupying different roles in the same feedback network or are participating in different networks entirely.

LFP Frequency and Coherence Differences

The single unit and multiunit activity remained locked in phase and coherent with the field potential, regardless of the underlying LFP frequency differences between the spontaneous and evoked cases. This points to network size as a possible modulating factor. In a recent study [(Lea-Carnall, Montemurro et al. 2016)], the network resonant frequency was inversely proportional to the size of the network in terms of total units. Since median nerve stimulation can cause large volleys to the thalamus, potentially even unnatural in terms of afferent recruitment [(Gardner, Hamalainen et al. 1984)], it is not unreasonable to predict that the resultant network activation is larger and more engaged than that of a spontaneous spindle. This provides a potential explanation for the consistently lower frequency value in the evoked spindle case than the spontaneous case.

LFP-Spike Phase Dynamics

The preferred phase for the strongly entrained units in the spontaneous spindles was net negative while the preferred phase of the evoked case was net positive, with no intraspindle evolving process to demonstrate any propagation from one phase direction to the other. It is known that not every cell participates in every spindle sequence, else an absolute network refractory period would result after sufficient cycles [(Contreras, Destexhe et al. 1997)]. However, the phase behavior per unit was preserved in each case across stimulation trials, sessions, and channels. LFP-phase interactions have been shown in previous literature to be utilized in neural coding in hippocampal place cells [(O'Keefe and Recce 1993)]. Given that the firing rate modulated phase precession in pyramidal place cells are known to be due to a cellular mechanism [(O'Keefe and Recce 1993), (Singer 2017)], it is not unreasonable to postulate that it could occur elsewhere in the brain in a location independent of hippocampus, such as S1 in this study. However, the results show that there is no firing rate dependence to account for the phase difference between spontaneous and evoked spindles, and other network dynamics are instead likely at play.

Driven Damped Harmonic Oscillator Model for Spike Phase Lag

One such potential explanation for the aforementioned phase lag is derived from observations in harmonic motion in Newtonian Mechanics. The premise is that we consider a damped harmonic oscillator that resonates at some frequency. According to the characteristics of this physical system, driving this oscillator at a frequency that difference from its natural resonance induces a positive phase lag, due to friction in the system. We propose that we can model the spiking activity of each single neuron as the intrinsic oscillator, and consider the LFP of the region to be the external driving force. This is

illustrated in Discussion Figure 5.2.6, which displays the classical equation for harmonic motion rewritten in neural terms – the variable *S* denotes the single unit spiking activity, the ω represents the angular frequency of the spontaneous and evoked rhythms, and ζ represents the biological damping in the system. In the "resting state," which we are denoting as the spontaneous spindle case, these neurons prefer to spike at a rate of 14 Hz without exogenous input. In the evoked case however, the frequency of the LFP is lowered to about 10 Hz, potentially due to a higher recruited network size and/or other factors. According to the driven damped oscillator model, driving the system at 10 Hz results in a positive phase lag from its spontaneous/resting state. This points to a potential biophysical reason for the phase shift that we see persist across almost all units and spindle cycles. To test the validity of this model, future work would need to modulate stimulation amplitudes to evoke a range of LFP frequencies between 10 and 14 Hz, and determine if the phase lag can be modulated by the frequency of the evoked spindle.

Differences in Underlying Network between Spontaneous and Evoked Spindles

In the experiments described above, the analyses performed do not fully elucidate the underlying origin of the difference in spike phase seen in the LFP of the spontaneous and evoked spindles. It remains to be seen if there are two anatomically/structurally different networks at play, or if this is the same network structure with the condition that the starting process of the thalamocortical ringing is essential in controlling the functional behavior of the circuit. Given the results presented in this paper, further research will need to be done to determine the worth of spontaneous spindles under sedation as a proxy for exploring somatosensory processing. The greater likelihood may be that spontaneous spindle activity

are generated by a brain in a resting state, while evoked spindles from afferent stimulation exhibit thalamocortical ringing for the purpose of sensory amplification, lasting long beyond the length of the initial stimulus. Upon completion of this extended cortical echo, the steady-state response returns to that seen in spontaneous spindles.

Phase Continuity between Spontaneous and Evoked Spindles

The above brings up the question of whether one should expect to see a unit reset from the positive phase of an evoked spindle to the negative phase behavior of a spontaneous spindle after sufficient time has passed. By inverting the cycle frequencies we observed for the evoked spindle, we arrive at a rough time of 900ms necessary to return to the steady-state frequency. Observing the phase behavior after this period could allow us to follow the steady-state transition of a single unit. However, unfortunately our experimental paradigm delivered median nerve stimuli at 1 Hz (i.e every 1000ms), and subsequent stimuli would be delivered within 100ms after, obstructing any extended observations of this transition. Since it is unlikely that spontaneous spindles would reliably generate immediately following an evoked spindle, a future experiment to visualize this phase transition would be to stimulate instead at say 0.1 Hz, which provides adequate time for the evoked spindle frequency envelope to reach steady-state and for a single unit to transition roles and phase behaviors.

Differences in Underlying Network Dynamics between Sedated and Awake Studies

A limitation of the present study is that the comparisons between spontaneous spindles and evoked spindles dynamics were conducted in sedated monkeys, rather than awake. Recent work has shown that median nerve stimulation can periodically modulate visual sensitivity in the context of a behavioral task in awake subjects [(Tomassini and D'Ausilio 2018)], which raises the question of whether the effects of thalamocortical rhythms extend much further than previously understood, including into other sensory systems while awake, but the role of single unit activity and local neural coding in awake experiments have yet to be explored. Periodic cortical rhythms are known to be amplified in sedated studies [(Timofeev, Contreras et al. 1996)] and the relative cortical quiescence may uncover single unit activity that are otherwise not as visible. Indeed, in previous awake studies [(Gardner, Hamalainen et al. 1984)], single units entrained to the LFP were seen for the 'fast' initial response 0-80ms post-stimulus but single unit activity was not seen in that study during the 'slow' latent spindle response; in the present sedated study, single unit activity was seen for both the 'fast' and 'slow' potentials. The similarity in the timecourse of peripherally-evoked S1 activity between the two studies informs that it is less likely that single units would alter LFP phase polarity under awake conditions. However given the effect of anesthesia on post-stimulus inhibition [(Poggio and Mountcastle 1963)], such network alterations cannot be ruled out completely without further study in awake animals.

Chapter VI: Discussion and Future Directions

6.1 Overview

In this summary, the work presented in this thesis seeks to better characterize somatosensation in the brainstem and develop a sensory prosthesis for spinal cord injury (SCI) patients. The structure of the thesis followed the flow of somatosensory information from mechanosensing through cortical perception.

First in Chapter II we began by designing a sensor to convert mechanical stimuli from the environment into electrical signals, akin to how mechanoreceptors in the periphery operate. We devised a new fabrication process to create compact, tunable antenna that were pressure sensitive in the range of forces usually felt at a fingertip.

There was a need to interface with the medial lemniscal pathway at a suitable target for somatosensory encoding in SCI patients. To this end, in Chapter III we presented the first chronic neural interface with the cuneate nucleus (CN) and demonstrated stability of long-term unit recordings using a novel spike-field metric.

Once an interface was established, these electrical signals were then encoded and delivered to the CN in Chapter IV in the context of a behavioral task, where they were detected at a rate significantly higher than chance by two monkeys.

Lastly, from previous literature we knew that that single stimuli to the periphery or brainstem evokes extended thalamocortical ringing, lasting many-fold longer than the initial stimulus. Thus in Chapter V, we sought to characterize downstream processing and neural oscillations in S1 in response to CN or median nerve stimulation. We found that the

amplitude of the evoked spindle oscillations were laminar-specific, and that the spike-phase of evoked spindles were fundamentally different from that of spontaneous spindles, pointing to two potentially different network roles for the same single units.

In this discussion, I explore the implications of these studies and limiting factors, as well as future directions to address open questions in the field.

6.2 Realistic Next Steps in Mechanosensing: Implantable MEMS

The novel fabrication process was successful and produced finely-tunable pressure sensors; however this technology in the context of SBI encountered two issues. First, fully passive technology is ideal because it obviates the need for a battery and its maintenance. However, such low-power sensing comes at a cost, and jumping directly to fully-passive sensing may have been premature for the technology at hand. In our experiments the signal-to-noise ratio (SNR) was too for practical use, especially when considering electrical noise from everyday objects.

Furthermore, while external noninvasive sensors are at first-glance the ideal option for implementation, trivial issues such as waterproofing, interference with grasping, and repetitive replacement for sensor degradation become a burden on the user in the long-term. Lastly, our designed sensors can currently only measure force in one direction, orthogonal to the surface, whereas the human finger is capable of multidimensional sensing.

We considered several alternatives, and as a next step we will develop an implantable, subcutaneous system for sensing forces, which uses near-field energy harvesting to power

the device and amplify the signal. An implantable force sensor would resolve many of the limitations of the aforementioned strategies.

First, it would not interfere mechanically with grasping and would be entirely transparent to the user. In addition, the artificial sensor can be designed to sense multiple force vectors (normal and shear forces) acting on the skin in the sensing range of 0 to 100 N (Birznieks, Jenmalm et al. 2001, Fortier-Poisson, Langlais et al. 2015), which typical of physiological grasping forces . We will use advanced MEMS and integrated circuit designs to produce a minimum-volume device that can be inserted into the fatty tissue below the skin. Lastly, we will fabricate a novel hermetic encapsulation for the device to ensure biocompatibility and device integrity while remaining compact.

6.3 CN Discrimination

Being the first lab to demonstrate CN detection in a behavioral paradigm opens the door for further behavioral studies in CN. However, with the knowledge that detection has been shown in nearly all other somatosensory targets, this result is not unexpected (Gaunt, Hokanson et al. 2009, Heming, Choo et al. 2011, O'Doherty, Lebedev et al. 2011). The next logical step is to determine the encoding capacity of the CN array in a discrimination task, which has not been shown previously and is necessary to catch up the CN literature to the established work in S1.

The 3AFC task we used in Chapter IV was originally designed to scale up to discrimination from detection. However, we found that the open trial format of the task led to diminishing

attention spans in the monkeys and, in some cases, overtraining, and was ill-suited for the more cognitively demanding task of discrimination.

We will next compare the psychometric properties of both CN and S1 microstimulation in a 2AFC task, akin to previously established discrimination studies in S1 (Tabot, Dammann et al. 2013). The key question to answer is whether sensory feedback to a user of an invasive neuroprosthesis might be improved by targeting microstimulation to CN rather than to S1. To answer this question we need to compare the percepts evoked from the two areas or, in other words, compare their psychometric properties.

Sensitivity to S1 stimulus intensity changes has been shown to be quite low. Less than 5 distinct intensity levels could be perceived with S1 microstimulation (Kim, Callier et al. 2015, Flesher, Collinger et al. 2016) (Figure 6.1). In contrast, in a study of peripheral nerve stimulation in two humans, approximately 20 distinct intensity levels could be perceived (Graczyk, Schiefer et al. 2016). These data suggest it may be beneficial to stimulate as far upstream as CN could yield a greater number of discriminable percepts than S1.

6.4 Mapping Mechanical to Electrical: LIDES and MDS

While mechanosensing and signal encoding have been discussed in this thesis, one missing component is the mapping of physical stimuli to CN microstimulation parameters. In a biomimetic strategy, one would perform an initial receptive field mapping to determine the electrodes with single units responsive to peripheral stimulation. Unfortunately in SCI patients, it is typically not possible to acquire this native map, as they are already deafferented. Instead in an arbitrary paradigm, the philosophy is that evoking perfectly

natural stimuli is near-impossible and the goal instead is to deliver discriminable stimuli that can be learned via operant conditioning. This can be done by uniquely mapping mechanical stimuli to a set of electrical stimuli for delivery to the CN, using a multidimensional scaling algorithm to preserve the discriminability determined in behavioral training.

We will develop a novel method for mapping measured sensations to nerve stimulation that ensures the resulting percepts are intuitive and discriminable. The method draws principally on the machine learning algorithms of multidimensional scaling (MDS) and manifold alignment (MA). We refer to our encoding strategy as *LIDES: Learning Intuitive and Discriminable Encoding Stimuli*.

There is usually no guarantee that each mechanical sensation is mapped to a unique perception (i.e. stimulus-induced percepts mapped to different sensors may not be discriminable). The LIDES algorithm seeks to provide a systematic way of ensuring unique sensation-perception maps. It will do this by (1) identifying stimuli that provide intuitive perceptions and (2) maximizing discriminability of stimuli in cases where no intuitive relationships exist.

The algorithm will have two stages. First, the monkey will make same-different judgments about pairs of electrical stimuli delivered sequentially to the CN. These pairwise judgments are input to the MDS algorithm that embeds the stimuli in a low-dimensional latent space, referred to as the perception space, in which the distance between stimuli corresponds to the perceived dissimilarity.

In the second stage of the algorithm, representative stimuli from discriminable clusters in perception space are presented to the monkey, who will now make absolute judgments regarding the modality (e.g. pressure) and location (e.g. thumb) of the percept (Figure 6.2). Corresponding sensation-perception data points are used in a semi-supervised MA algorithm to generate an encoding transformation from sensor space to perception space. The final output of LIDES is a subject-specific encoding transformation, *T*, which will be implemented by the full SBI device.

6.5 State-Dependent Alpha Modulation of CN Detection in Awake Primates

Our studies in spontaneous and evoked spindles and the differences in their underlying networks provide insight in the context of sensorimotor prosthetics, which by design activate these same networks. However, the extent of this is limited by the fact that these studies were done in anesthetized monkeys, where the brain is in a state of relative inactivity. Neural oscillations are amplified under anesthesia and activation of thalamocortical loops can rouse other cortical regions across hemispheres that may not be readily possible under awake circumstances (Adrian 1941, Destexhe, Contreras et al. 1999, Steriade 1999). Thus, corroborating this evidence in awake studies is critical to understanding the role of these reverberant networks in sensory processing.

There is considerable evidence for the brain-state dependence of sensory percepts. In particular, the amplitude and phase of alpha oscillations recorded in sensorimotor cortex are correlated with perceptual performance with natural tactile stimuli (Haegens, Handel

et al. 2011, Haegens, Nacher et al. 2011, Ai and Ro 2014). It has been suggested that alpha gating of S1 activity is a mechanism for top-down selective attention to behaviorally-relevant sensory information (Jensen and Mazaheri 2010). However, are artificial stimuli similarly gated? This is not a question that has been addressed previously in the somatosensory encoding literature, but could be critical to the sensory experience provided by a neuroprosthesis. Oscillatory gating has been shown to involve the sensory thalamus as well as cortex (Haegens, Vazquez et al. 2014). The ability to leave physiological sensory gating intact by encoding upstream of this mechanism may be another important advantage of choosing the CN as the encoding site, as opposed to S1. We will test the hypothesis that perceptions of CN stimuli are modulated by pre-stimulus S1 alpha (8-14 Hz) oscillations, namely that detection thresholds are inversely correlated with pre-stimulus S1 alpha power. Dual high-density chronic implants of the DCN and S1 would allow us to explore the dynamics of ascending somatosensory information. These experiments would be among the first to address the brain-state dependence of artificial percepts.

Closing Remarks

In summary the broader impact of this dissertation and future work will provide, in combination with motor prostheses currently under development, innovations toward a therapy that could improve the quality of life of millions of people with hand paralysis due to spinal cord injury. An even broader impact could be realized by supra-physiological sensory augmentation.

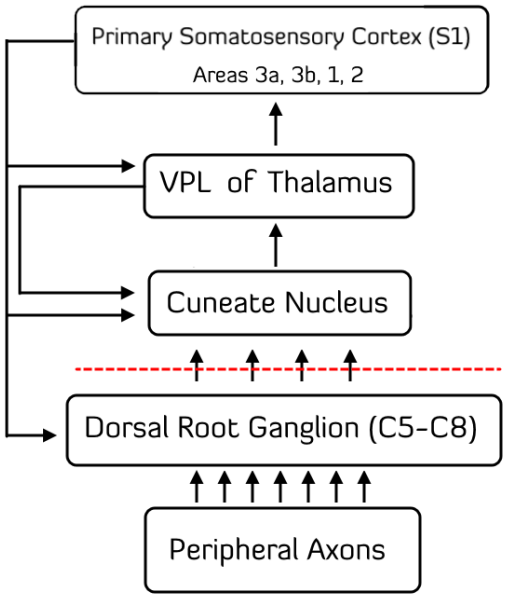

Figure 1.1. Schematic representing the medial lemniscal pathway, which displays the primary flow of tactile information in the body. Red dotted line dictates the site of injury in the pathway in the SCI patient, highlighting the cuneate nucleus (CN) as the first available somatosensory target in this patient population.

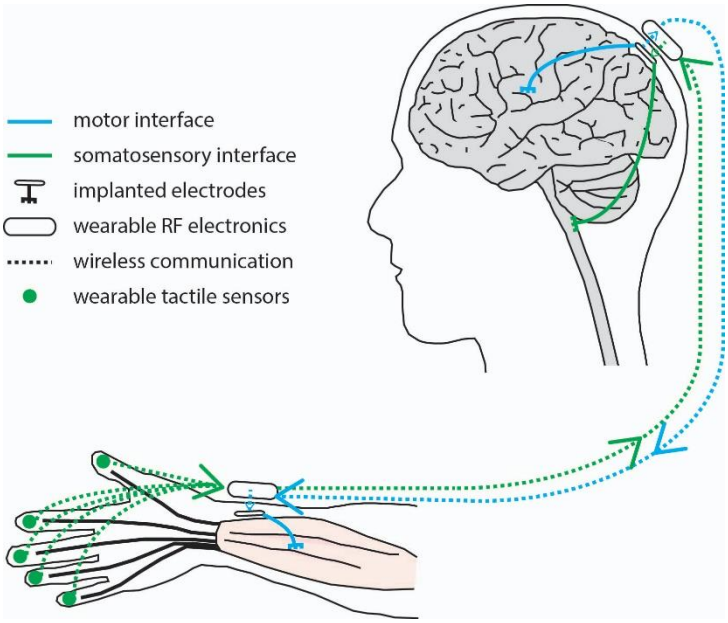

Figure 1.2. Envisioned bidirectional clinical hand neuroprosthesis. Motor function is restored through brain-controlled electrical stimulation of hand muscles. Somatosensation is restored through sensor-controlled electrical stimulation of the brain. Radiofrequency (RF) electronics worn at the head and wrist wirelessly communicate information between the brain and arm.

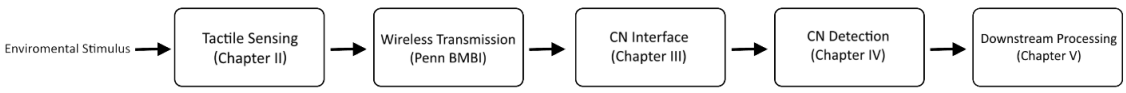

Figure 1.3. Roadmap for thesis chapters, which decisively follows the path of information in our proposed SBI device, starting from the physical stimulus from the environment. This is transduced from mechanical energy to electrical energy - Chapter II. The signal is then converted from physical properties of the stimulus to electrical stimulation parameters and sent to the brainstem stimulator (Penn BMBI, out-of-scope for this dissertation). Microstimulation is then delivered to a chronic interface with the CN within safe electrical thresholds and detected within a behavioral paradigm

(Chapter III and IV). Lastly, the downstream effects of this stimulation are explored in S1 cortex in an electrophysiological context (Chapter V).

Figure 2.1: Schematic demonstrating cementing process for the two PDMS halves

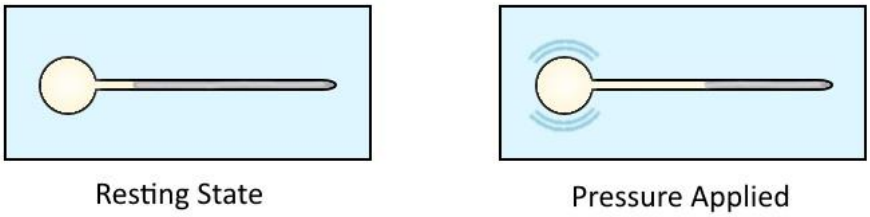

Figure 2.2: Schematic demonstrating dynamic shrinking of antenna length with applied pressure

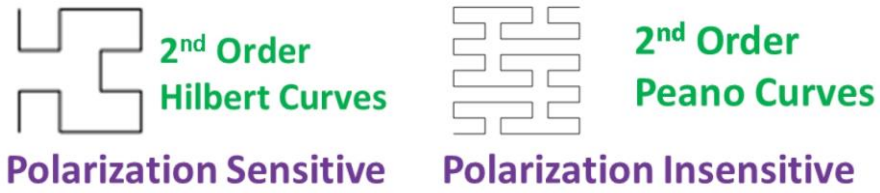

Figure 2.3: Space filling curves: 2nd-order Hilbert curve (left), 2nd-order Peano curve (right)

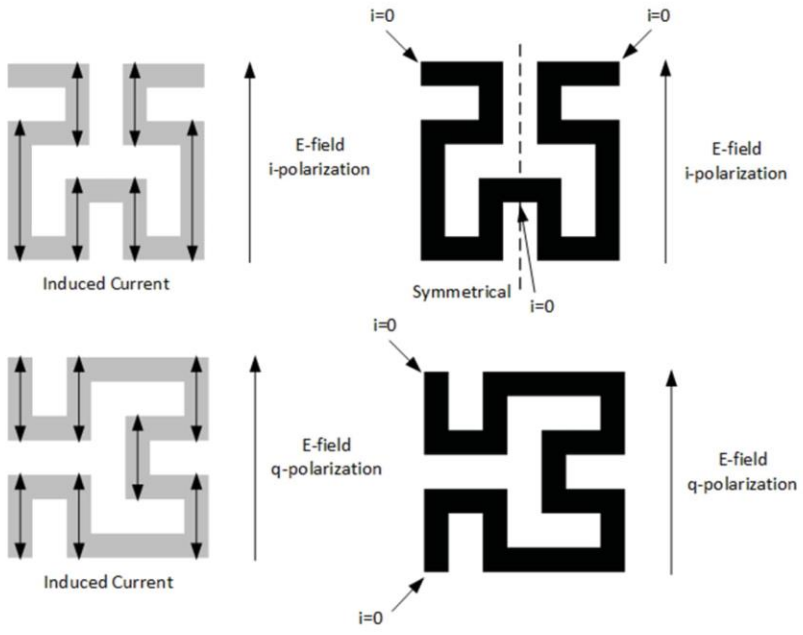

Figure 2.4: Resonance mechanism of a 2nd-order Hilbert curve

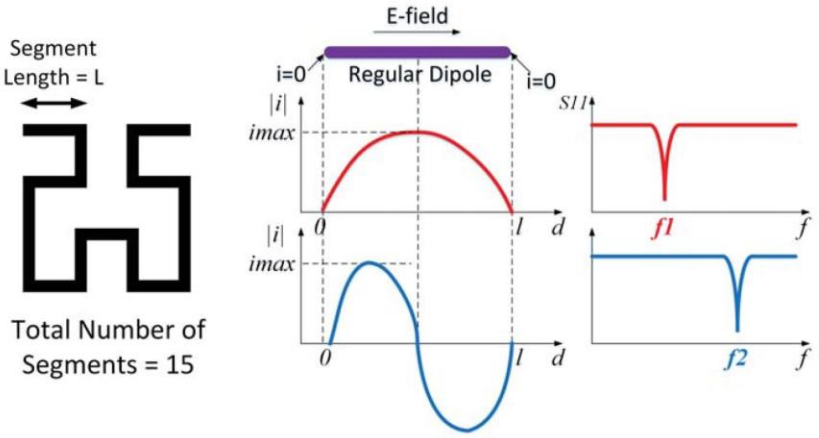

Figure 2.5: Resonance mechanism of a 2nd-order Hilbert curve

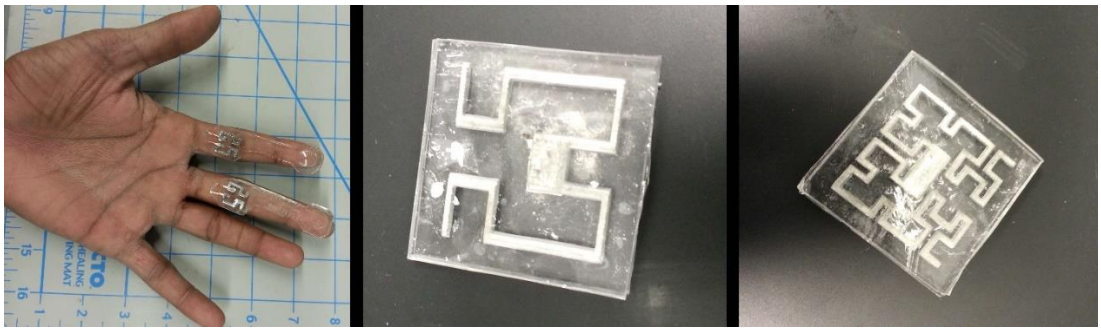

Figure 2.7: Force sensitive antenna prototypes

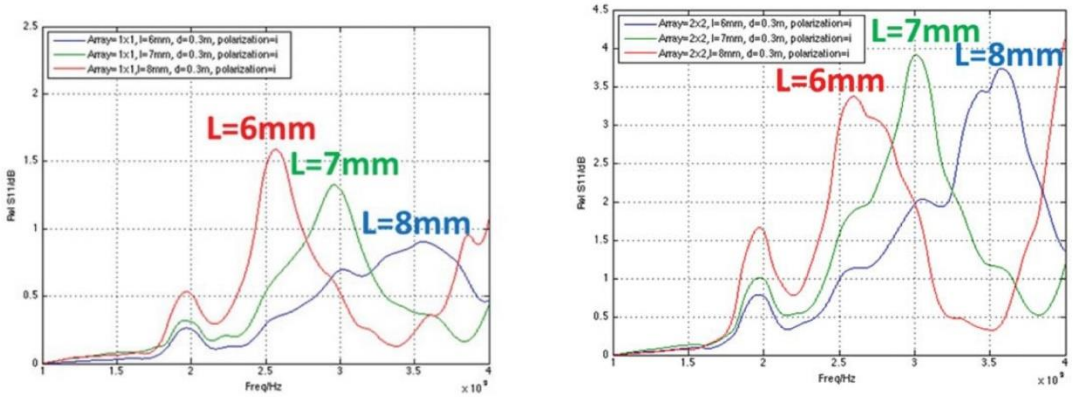

Figure 2.8: Measured responses of single 2nd-order Hilbert-curve tags with different sizes (left) and responses of 2×2 arrays of 2nd order Hilbert-curve tags with different sizes (right).

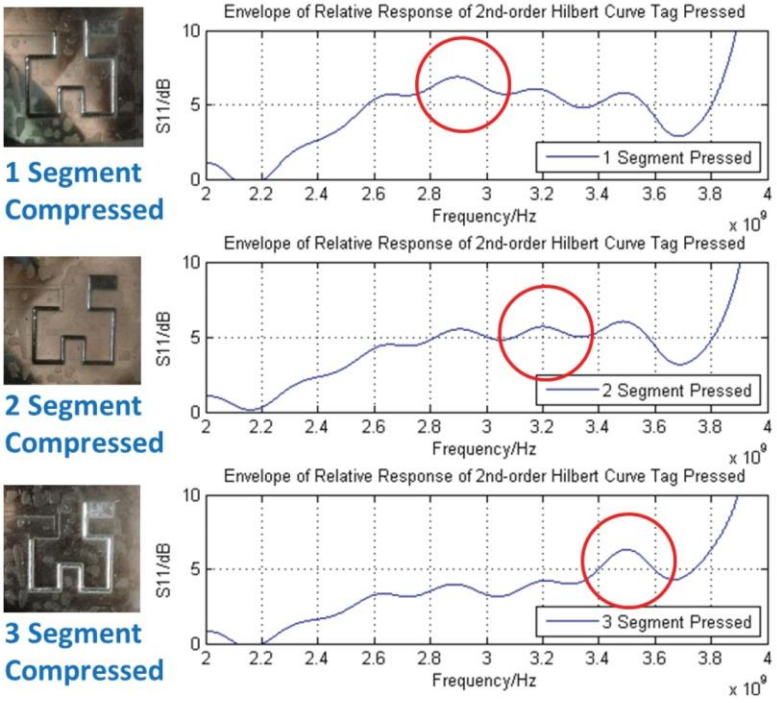

Figure 2.8: Frequency responses of the 2nd-order Hilbert-curve force sensor made of GaIn liquid metal

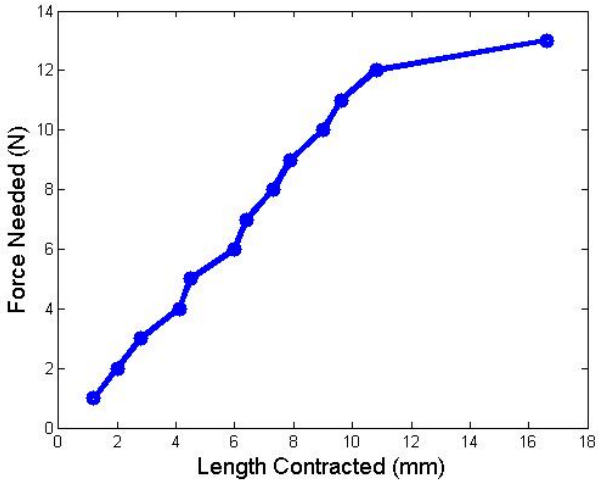

Figure 2.9: Quasilinear length response in relation to force applied to pressure well

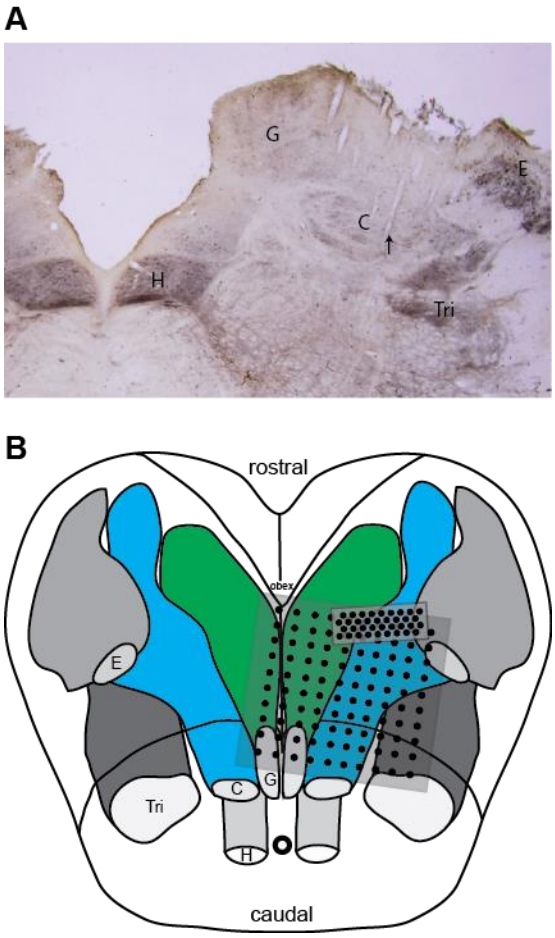

Figure 3.1. Anatomical location of the chronically-implanted electrode arrays. **A**, Example histological section of the brainstem stained with cytochrome oxidase. G = gracile nucleus, C = cuneate nucleus, E = external cuneate nucleus, H = hypoglossal nucleus, Tri = trigeminal nucleus. Electrode tracks can be seen in the dorsal column nuclei (arrow). **B**, Reconstruction of the location of the electrode arrays relative to the brainstem nuclei. Each black dot represents an electrode. The larger, 96-electrode array was implanted in monkey C. The smaller, denser, 32-electrode array was implanted in monkey B. The targeted gracile and cuneate nuclei are highlighted in green and blue, respectively.

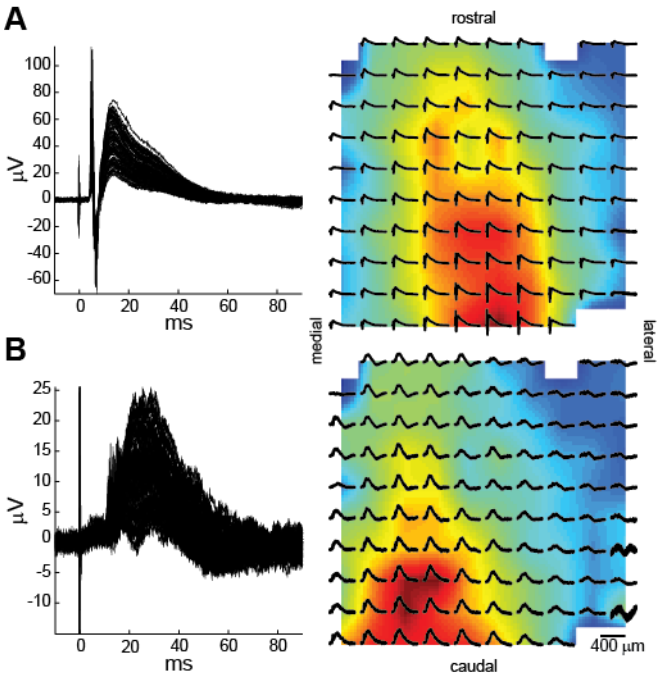

Figure 3.2. Responses recorded on the Utah array in monkey C to transcutaneous electrical stimulation of the ipsilateral median (**A**) and tibial (**B**) nerves. The temporal (**left**) and spatial (**right**) aspects of the response are shown for all 96 electrodes. For the latter, the color map indicates the relative size of the response interpolated across the array, with red regions having the largest response. Shown are the average responses to 100 stimulus pulses.

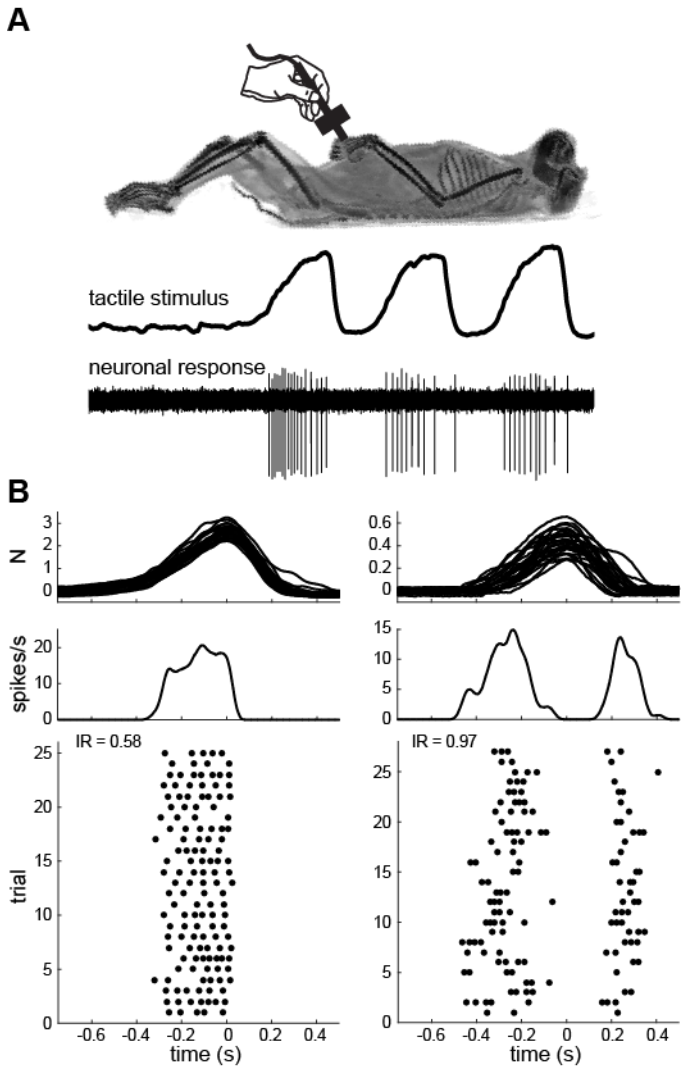

Figure 3.3. Single unit receptive field mapping: examples. **A**, Tactile stimuli were delivered to the skin with a hand-held, force-sensing probe and neuronal responses were recorded. **B**, Two stimulus-response examples showing the stimulus force traces (top; aligned on the peak force), instantaneous spike rate (middle), and spike raster (bottom). Stimuli were applied to the hairy skin of the upper back (left) and glabrous skin of digit 5 (right). The irregularity (IR) value for the spike train responses is shown.

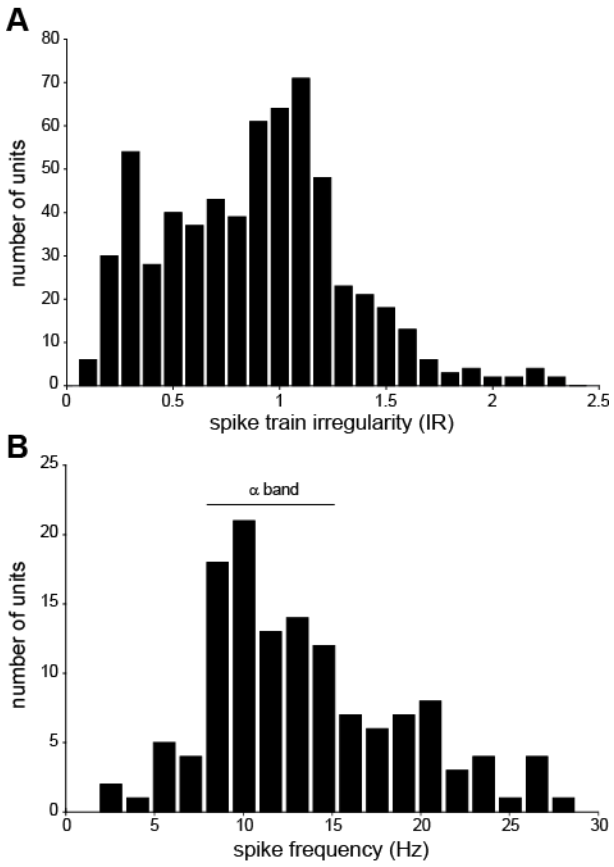

Figure 3.4. Summary of spike train irregularity. **A**, The distribution of IR for all 629 recorded units. **B**, The distribution of spike frequency for units with IR values less than 0.6. The typical frequency range of the alpha rhythm (8-14 Hz) is indicated.

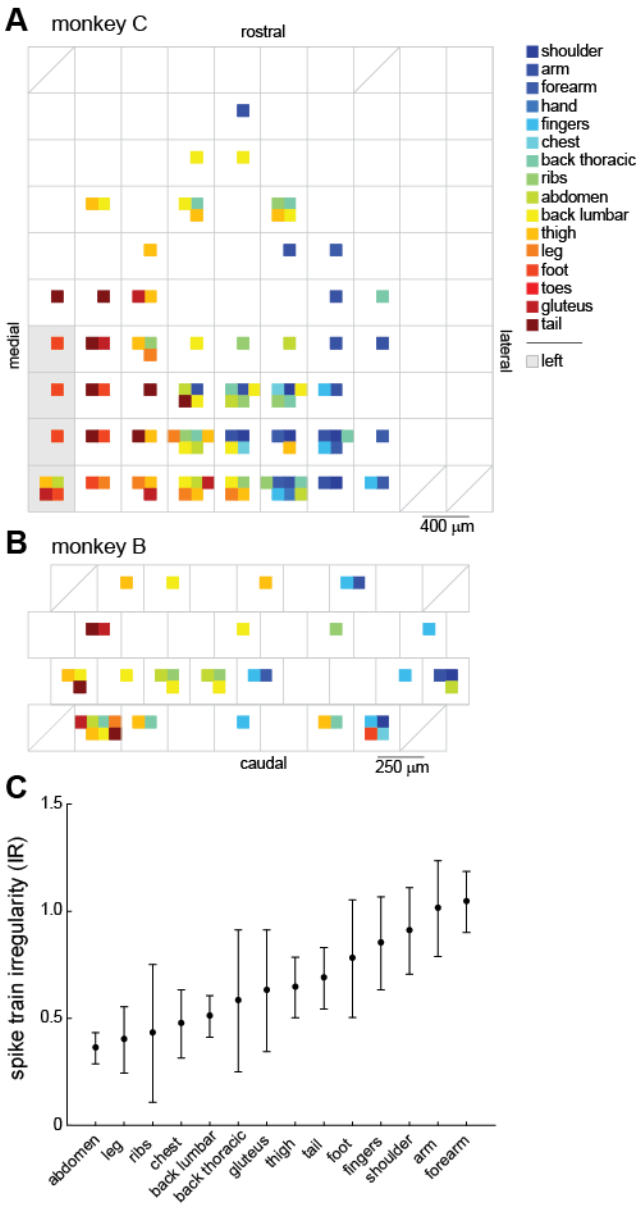

Figure 3.5. Single unit receptive field mapping summary for monkey C (**A**) and monkey B (**B**). The colored boxes indicate each unique receptive field identified at each electrode on the array. Shaded boxes in A indicate sites responsive to mechanical stimuli delivered to the left side of the body. Boxes with diagonal lines indicate the absence of a working electrode at that location. **C**, Average irregularity metric for units grouped by RF category (mean ± 95% confidence intervals;

category order sorted by mean IR value). Categories with two or less units were omitted (22.4 units/category on average).

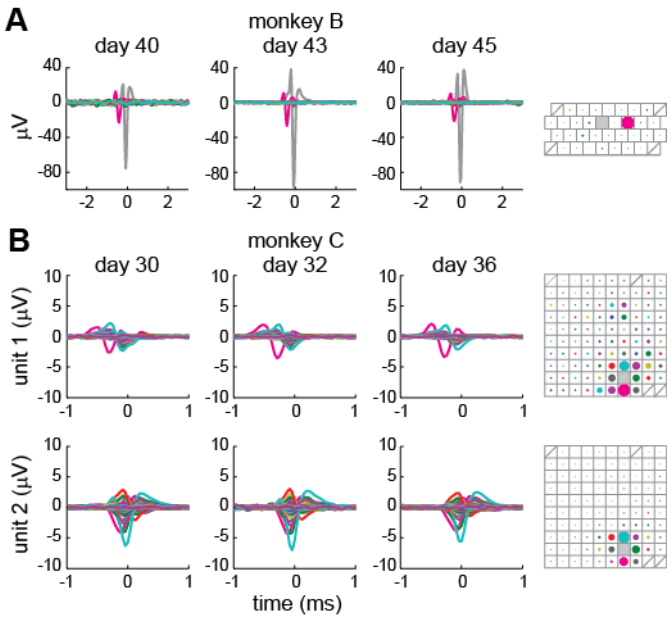

Figure 3.6. Spike-triggered field (STF) examples for monkey B (**A**) and monkey C (**B**). Gray traces show the mean spike waveform of the triggering spikes (omitted in B for clarity). Colored traces show the STF for all other electrodes on the array. 500 spikes were used to compute the triggered averages. The array diagrams on the right show the corresponding array locations of the STFs relative to the triggering electrode (gray box). The diameter of the colored circles at each electrode site in the array diagrams is proportional to the integral of the rectified STF from the first session, normalized to the largest observed value for that session.

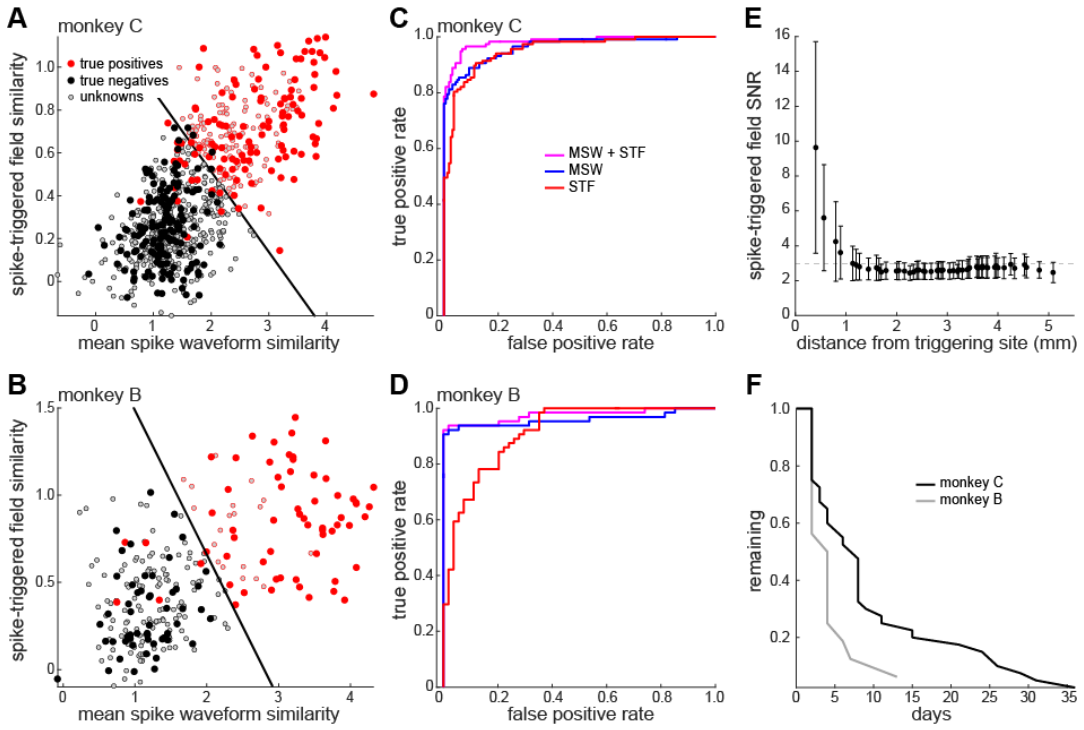

Figure 3.7. Neuronal stability analysis. **A**, For monkey C, MSW and STF similarity scores for pairs of units thought to be from the same neuron (red, "true positives"), pairs of units thought to be from different neurons (black, "true negatives"), and pairs of units recorded on the same electrode but different sessions (gray, "unknowns"). The decision boundary from a linear discriminant analysis classifier trained on the true positives and false positives is shown (black line). Markers for the unknown group are outlined red (same neuron) or black (different neurons) depending on which side of the boundary they fall. **B**, Same as A, but for monkey B. **C**, Classifier performance for monkey C. Receiver operating characteristic (ROC) curves are shown for classifiers using both the MSW and STF features, just the MSW, and just the STF. **D**, Same as C, but for monkey B. **E**, Signal-to-noise ratio (SNR) of the STFs as a function of distance from the triggering electrode (mean ± standard deviation). **F**, Fraction of the 40 (monkey C) or 16 (monkey B) stable neurons remaining as a function of the number of days over which the neurons were observed.

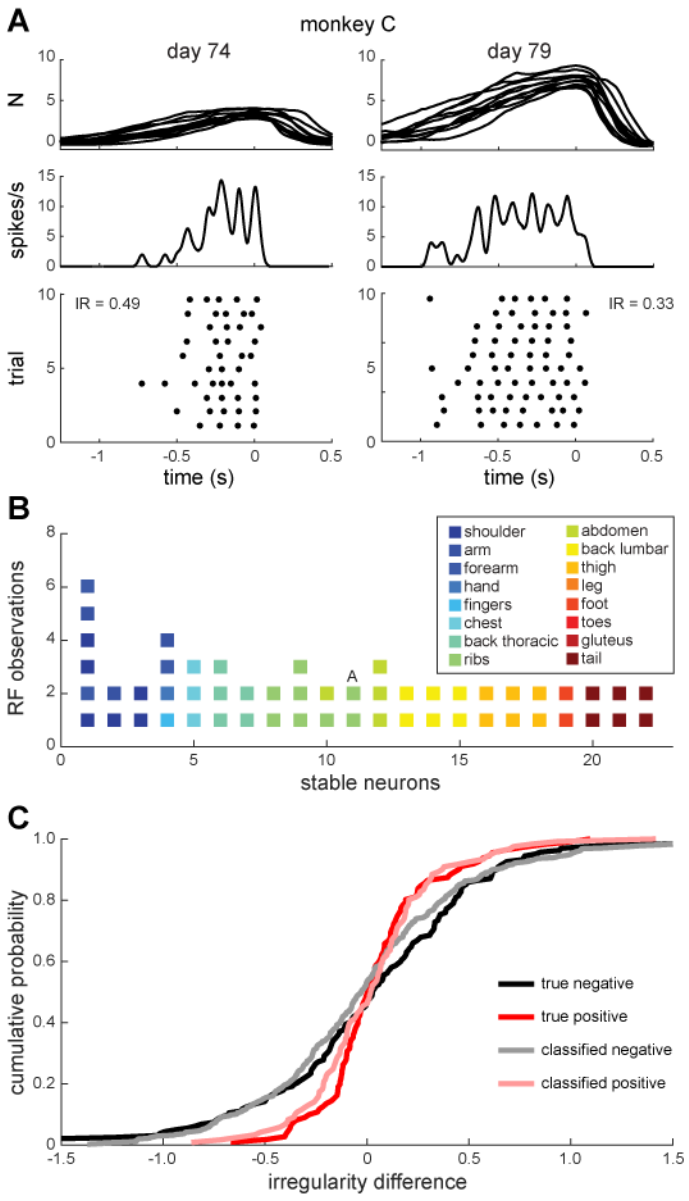

Figure 3.8. Receptive field stability. **A**, RFs of one example stable neuron on two different sessions, showing stimulus force traces (top; aligned on the peak force), instantaneous spike rate (middle), and spike raster (bottom). In both sessions, stimuli were applied to the skin of the 5th intercostal space. **B**, Summary of RF observations for 23 stable neurons. The color of the boxes indicates the location of the RF at each observation. Neuron 11 is the example shown in A. **C**, Stability of spiking response pattern for the 629 recorded units. The cumulative probability

distribution of IR differences between pairs of units is shown. Unit pairs were grouped into true negatives, true positives, and unknowns as in the neuronal stability analysis. The unknown pairs were further grouped into classified negative (i.e. from different neurons) and classified positive (i.e. from same neuron) based on the MSW+STF classifier output.

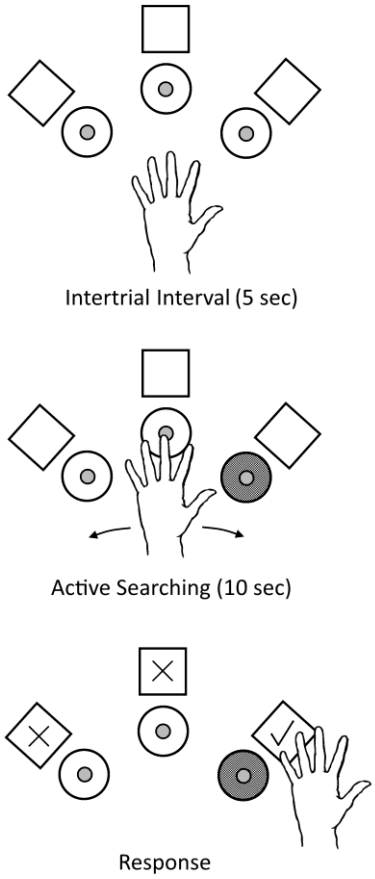

Figure 4.1. Active touch oddity task (ATOT). The task consisted of three vibrotactile actuators (circles) and three response sensors (squares). One actuator was chosen as the oddity on each trial (gray circle). The objective was to move the hand to find the active actuator and indicate this choice by pressing the corresponding response sensor (checked square).

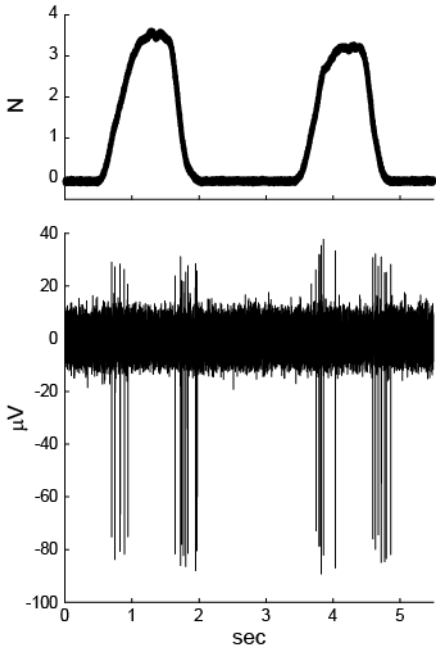

Figure 4.2. Stimulus-response data of one example CN neuron from monkey A. Force pulses were applied to the extensor surface of the forearm, near the elbow (top). The neuron responded with bursts of action potentials at the beginning and end of each pulse (bottom).

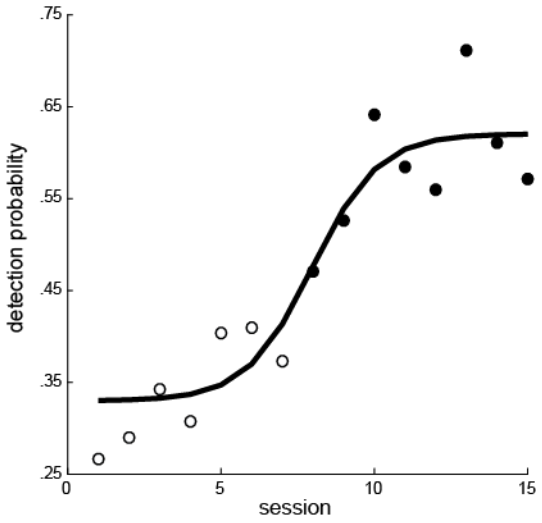

Figure 4.3. Performance of monkey E as he learned to detect CN microstimuli (80 µA, 100 Hz). Filled circles indicate the sessions in which the performance significantly differed from performance on catch trials (chi-squared tests, $p < .05$). A logistic function fit to the data is shown.

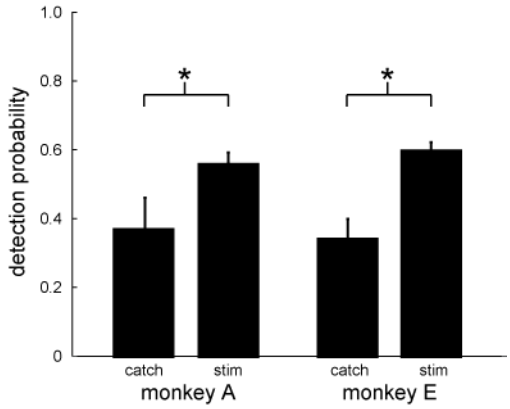

Figure 4.4. Summary of detection probability of CN microstimuli (80 µA, 100 Hz) across all post-learning sessions. Error bars indicate the 95% confidence interval on the mean. Significant differences were observed between stimulus and catch trials for both monkeys (chi-squared tests, $p<0.05$).

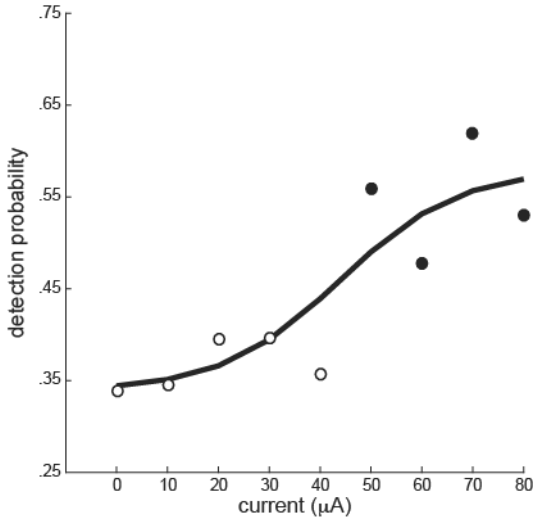

Figure 4.5. Detection probability as a function of current amplitude. Pulse frequency was 100 Hz for all amplitudes. Data for 0 μA were from catch trials. Filled circles indicate the amplitudes in which the performance significantly differed from performance on catch trials (chi-squared tests, $p < .05$). A logistic function fit to the data is shown.

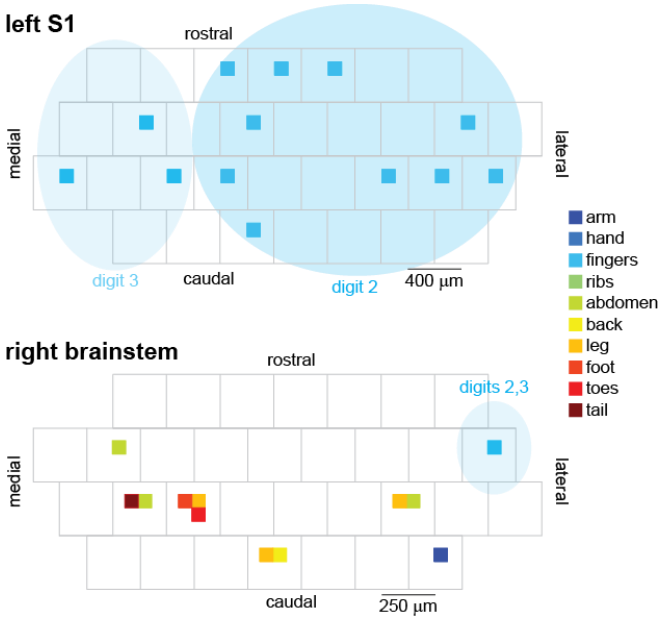

Figure 5.1.1. Receptive field (RF) maps of single unit activity recorded on the brainstem (bottom) and S1 (top) arrays. The gray-outlined boxes indicate the relative position of the electrodes within the arrays. The small, colored boxes indicate the array location and RF of each unit for which an RF was identified. The blue ovals highlight the electrodes on which units with finger representations were found.

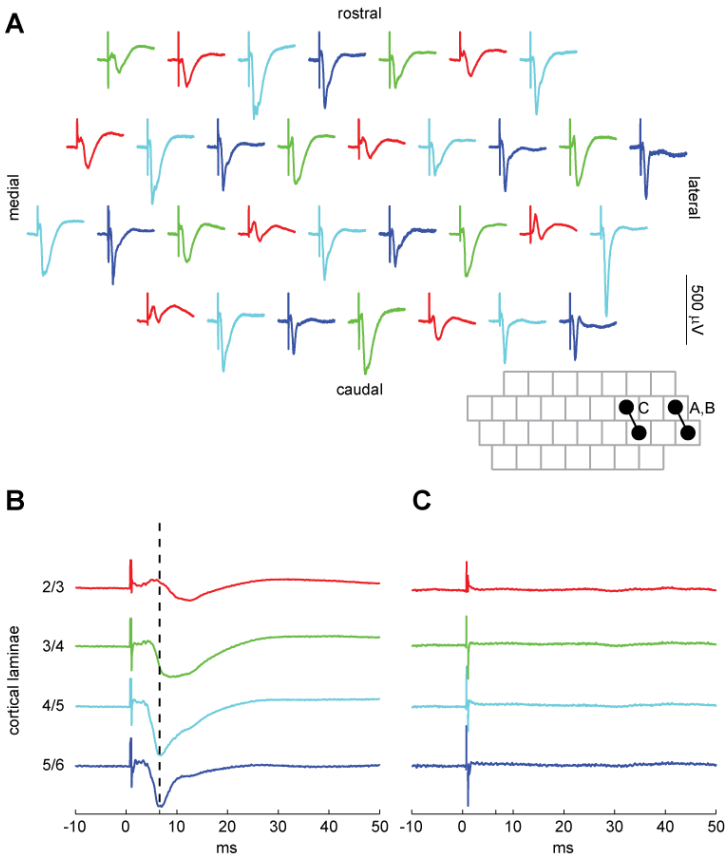

Figure 5.1.2. S1 field potentials evoked from brainstem stimulation. **A**, The field potential at each S1 electrode evoked from a single, 50-µA pulse delivered to the pair of electrodes on the brainstem array labeled 'A,B' in the inset. The four different colors label the four different electrode lengths present on the array. **B**, The evoked potentials shown in A averaged for each electrode length. The approximate laminar location of each length electrode is indicated. **C**, The field potentials evoked from a 50-uA pulse delivered to the pair labeled 'C' in the inset.

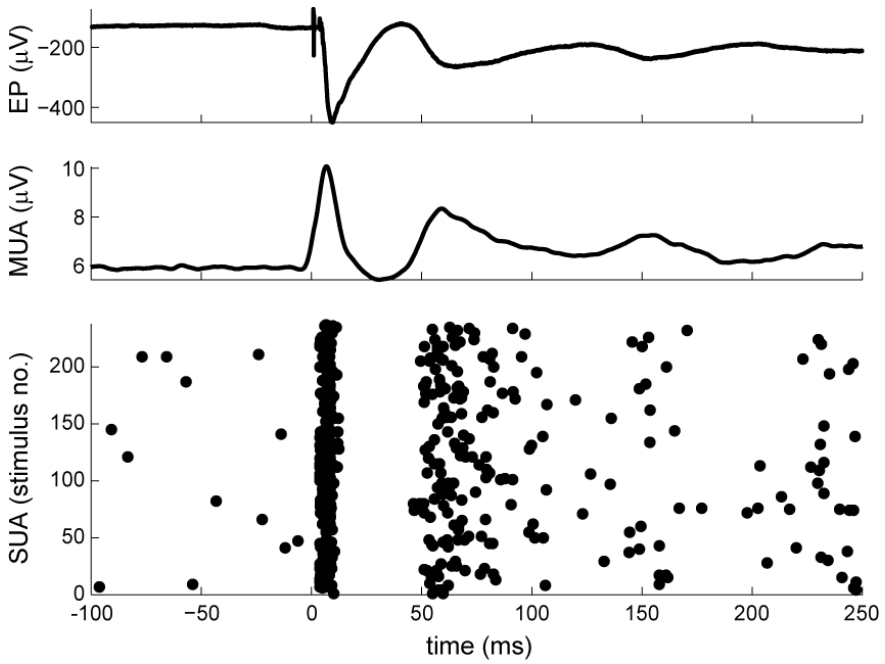

Figure 5.1.3. Evoked potential (EP, top), multiunit activity (MUA, middle), and single unit activity (SUA, bottom) recorded in S1 in response to a 50-μA stimulus pulse to the CN. Each dot in the SUA plot represents an action potential. Stimuli were delivered once every 5 s. The average response to the 237 stimuli is shown for the MUA and EP.

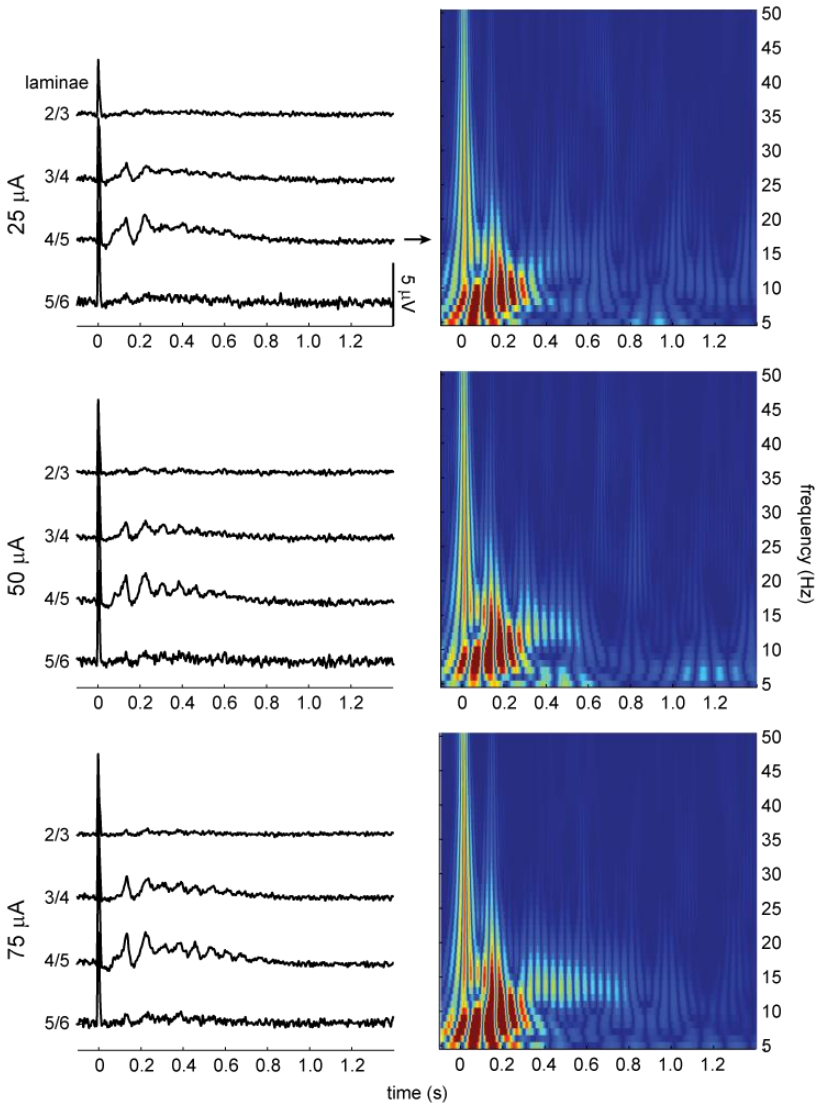

Figure 5.1.4. Laminar multiunit activity (MUA) recorded in S1 in response to a 25-µA (top row), 50-µA (middle row), and 75-µA (bottom row) stimulus pulse to CN. The wavelet scaleogram in the right column shows the frequency content of the lamina 4/5 MUA response.

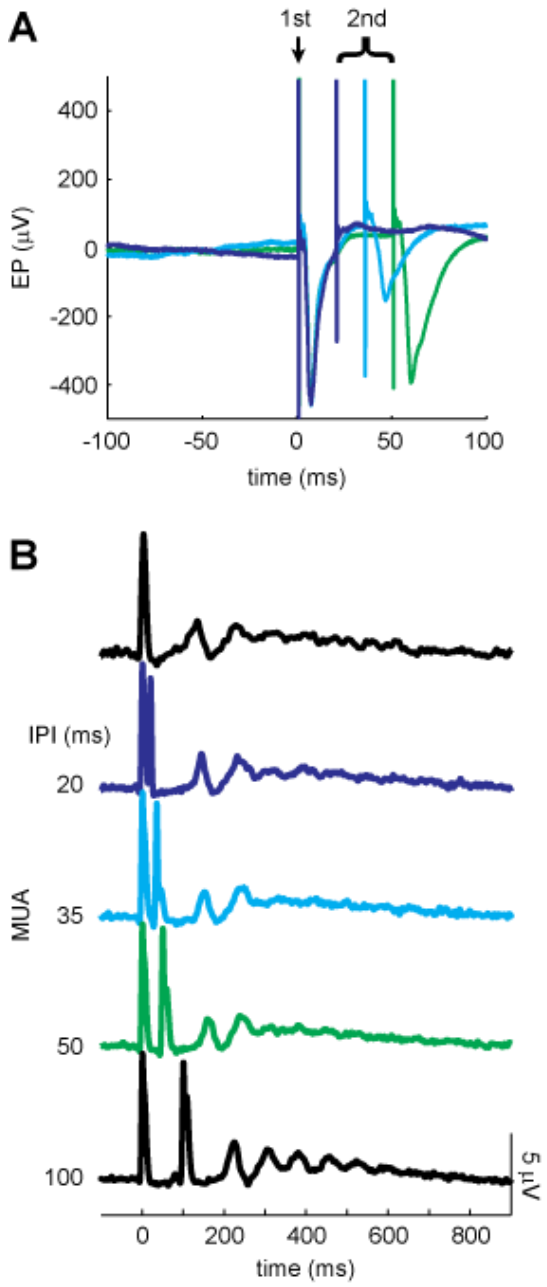

Figure 5.1.5. S1 response to pairs of stimuli delivered to the CN. **A**, S1 evoked potentials for three different interpulse intervals (IPI): 20 ms (blue), 35 ms (cyan), and 50 ms (Chung, Magland et al.). Stimulus artifacts of first and second pulses are indicated. **B**, S1 multiunit activity for a single, 25-μA pulse (top) and paired, 25-μA pulses with four different IPIs.

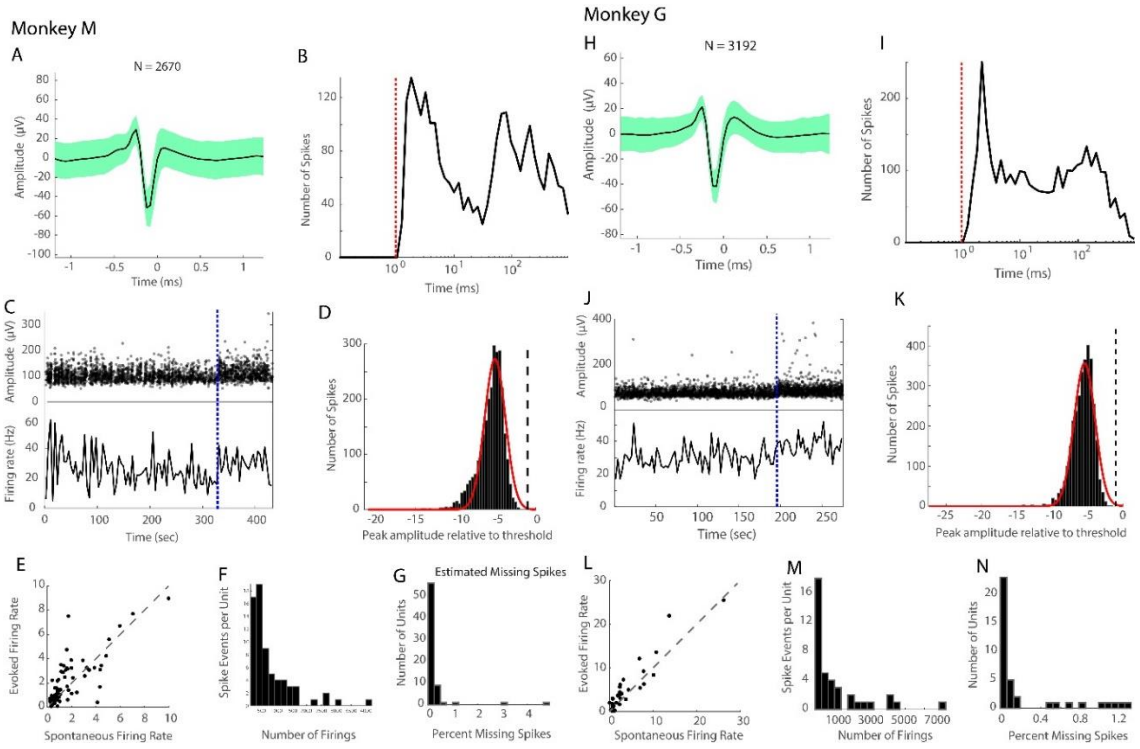

Supp. Figure 5.2.1. Quality metrics for S1 units recorded in Monkey M (*n*= 69) and Monkey G (*n*=39). (***A, H***) Spike waveform (mean ± standard deviation) of an example neuron. (***B, I***) Interspike interval histogram of the example neuron. Red dashed line indicates the absolute refractory period (1 ms). (***C, J***) Waveform amplitude (top) and firing rate (bottom) of the example neuron during the spontaneous activity block (before blue dashed line) and evoked activity block. Peripheral nerve stimulation was delivered in the latter. Firing rate bin width = 10 s. (***D, K***) Histogram of peak waveform amplitude for example neuron. Dashed black line indicates the spike detection threshold. Solid red line is a Gaussian fit of the histogram to estimate the number of subthreshold waveforms from this isolated unit (i.e. false negatives). (***E, L***) Scatter plot of the average firing rate in the spontaneous and evoked activity blocks for each unit in the population. Dashed black line displays line of unity. (***F, M***) Histogram of the number of spike events per unit in the population. During curation process, units with high firing rate and poor signal-to-noise ratio were manually removed

from the population. (***G, N***) Histogram of percent of missing (subthreshold) spikes for all units in the population, based on the analysis shown in D, K.

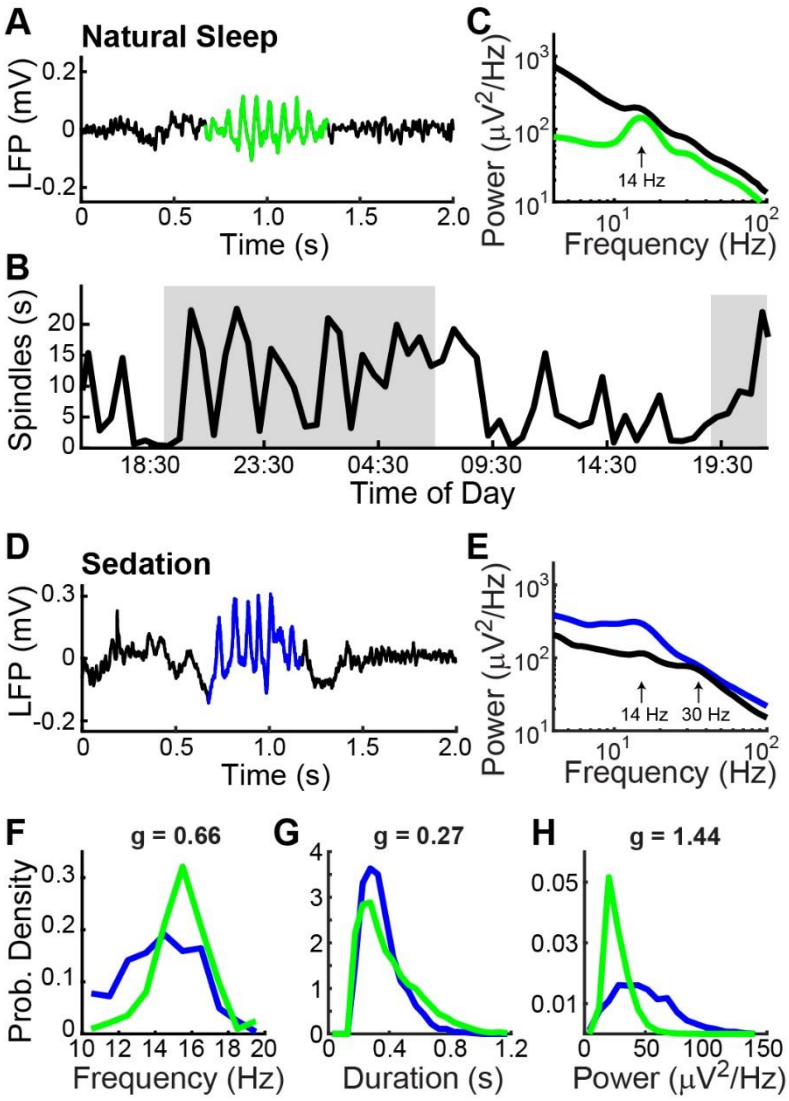

Figure 5.2.1. Spontaneous S1 spindles during sleep and sedation. (***A***) Example spindle recorded from one S1 electrode during natural sleep in monkey M. Green region highlights spindle activity as detected using $P_{episode}$ analysis [*Caplan et al, 2001*]. (***B***) Amount of spindle activity detected

by $P_{episode}$ analysis throughout a 34-h recording while monkey M was freely behaving in his home cage. Bin size = 1 h. Activity was highest during the 7 PM to 7 AM lights-off period (marked by dashed vertical lines) and exhibited a cyclic pattern putatively related to sleep cycles. (***C***) Power spectral density (PSD) computed from overnight recording. A physiological peak due to the spindle activity is seen around 14 Hz. PSD computed only from detected spindle episodes are plotted in green. (***D***) Example S1 recording in monkey M during ketamine-dexmedetomidine sedation. Spindle activity detected by $P_{episode}$ analysis is highlighted in blue. (***E***) PSD computed from entire sedated recording, with physiological peaks around 14 Hz for spindle activity and 30 Hz due to heightened gamma rhythms under sedation. PSD computed only from detected spindle episodes are plotted in blue. (***F,G,H***) Distribution of spindle peak frequency, duration, and peak power across sleep episodes (green) and sedation episodes (blue). Differences in each pair of distributions quantified by Hedges' g.

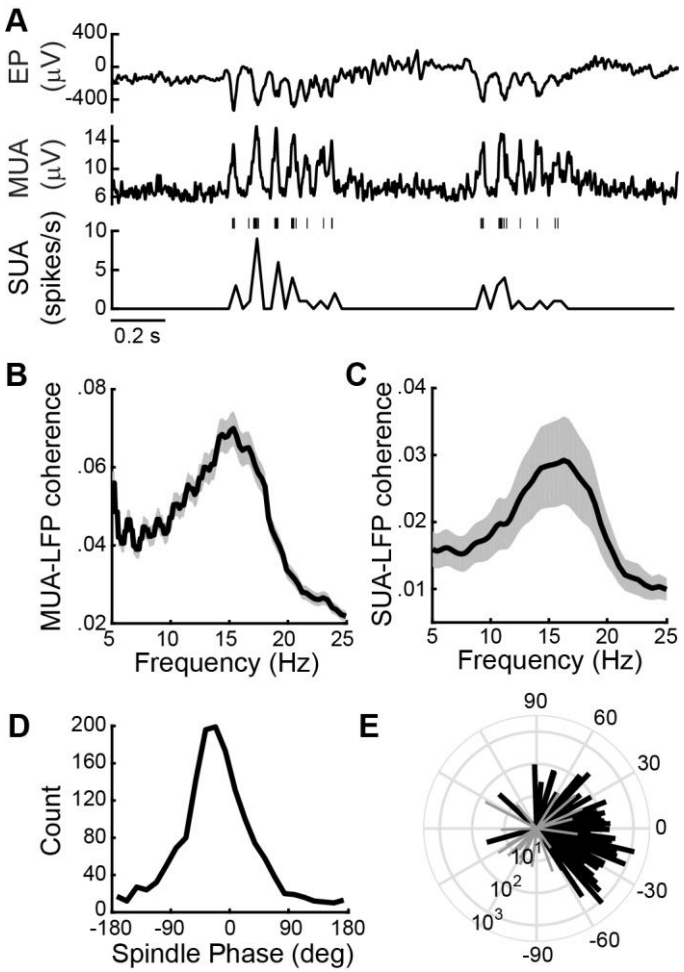

Figure 5.2.2. Entrainment of S1 unit activity to spontaneous spindles during sedation. (***A***) Local field potential (LFP), multi-unit activity (MUA), and single-unit activity (SUA) recorded in monkey M during example spontaneous spindle bursts detected in the LFP. For SUA, spike times are indicated by vertical lines and the firing rate was calculated in 25-ms bins. (***B***) Population MUA-LFP coherence spectrum (mean ± 95% CIM). Magnitude squared coherence estimated using Welch's averaged modified periodogram method and averaged across S1 channels. (***C***) Population SUA-LFP coherence spectrum (mean ± 95% CIM). Coherence was calculated as the ratio of the power spectrum of the spike-triggered LFP average over the spike-triggered LFP power spectrum [*Fries et al, 1997*]. (***D***) Distribution of LFP spindle phases at spike times for an

example unit. (***E***) Resultant vectors conveying the preferred phase (vector direction) and depth of tuning (vector magnitude) for all units. Vectors shown in black or grey correspond to units for which the spindle phase distribution was or was not significantly unimodal (Rayleigh test, $p < .05$), respectively. Negative preferred phase values correspond to spiking that on average preceded the spindle cycle peak.

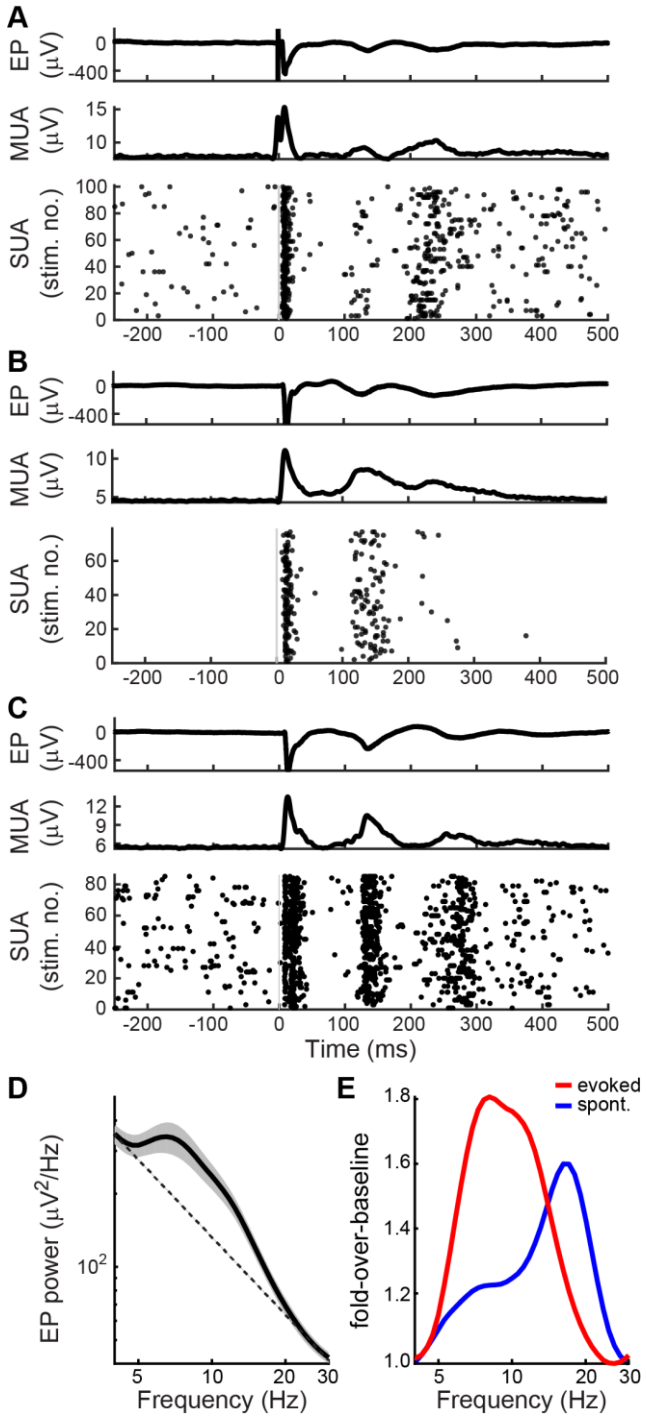

Figure 5.2.3. S1 spindles evoked by median nerve stimulation. Evoked potential (EP, top), MUA (middle), and SUA (bottom) recorded in S1 following 1-mA, 0.2-ms stimulus pulses delivered transcutaneously to the contralateral median nerve in monkey M (***A***) and monkey G (***B,C***).

Stimulus pulses were delivered at 1 Hz. Each dot in the SUA raster plot represents a spike of the isolated unit. The average response to the stimuli is shown for the EP and MUA. (***D***) Population PSD of the EP (mean ± 95% CIM). Dotted line shows fitted 1/f background noise level used for fold-over-baseline calculation. (***E***) Fold-over-baseline for mean PSD of evoked (red) and spontaneous (blue) spindles. Note difference in spindle frequency.

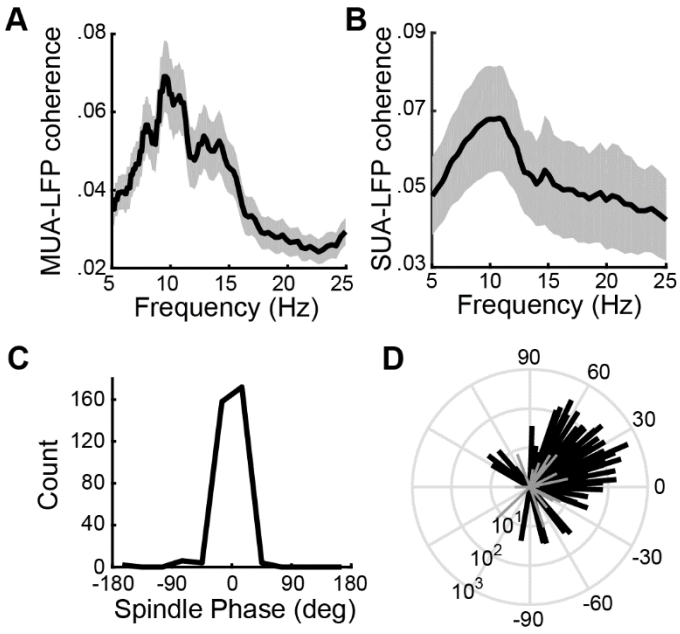

Figure 5.2.4. Entrainment of S1 unit activity to evoked spindles. (***A***) Population MUA-LFP coherence spectrum (mean ± 95% CIM) across all sedated sessions and electrodes. (***B***) Population SUA-LFP coherence spectrum (mean ± 95% CIM) across all single units from both animals (*n=108*). (***C***) Distribution of EP spindle phases at spike times of an example unit. (***D***) Resultant vectors conveying the preferred phase (vector direction) and depth of tuning (vector magnitude) for all single units. Vectors shown in black or gray correspond to units for which the spindle phase distribution was or was not significantly unimodal (Rayleigh test, $p < .05$). Positive

preferred phase values correspond to spiking that on average occurred after the spindle cycle peak.

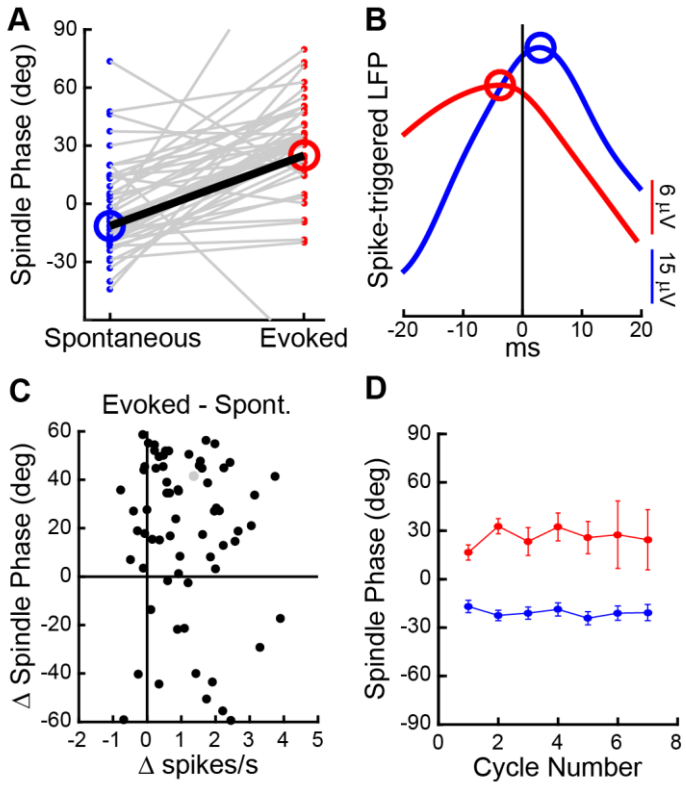

Figure 5.2.5. Comparison of S1 spike timing to spontaneous and evoked spindles. (***A***) Direct comparison of preferred phase of spontaneous spindles (blue dot) and evoked spindles (red dot) for each single unit (gray line). Bold line and colored circles indicate average preferred phase for the population. (***B***) Spike triggered average of the LFP for all spikes during spontaneous (blue) and evoked (red) spindles. Colored circles indicate the peak of each STA. (***C***) Change in preferred phase plotted against change in mean firing rate between spontaneous and evoked sessions within the same day. Each dot represents a single unit. Population

average changes indicated by gray dot. (***D***) Population preferred spindle phase (mean ± 95% CIM) across all units in each cycle of the evoked (red) and spontaneous (blue) spindle events.

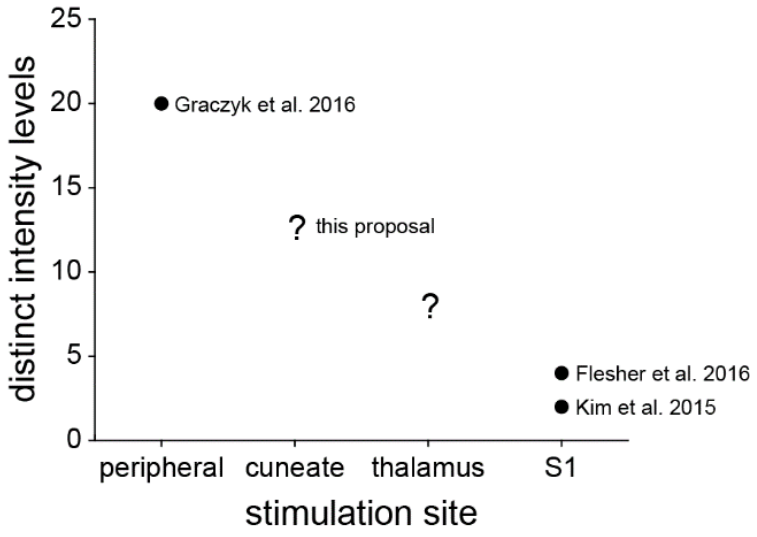

Figure 6.1. Summary of sensitivity to intensity of artificial stimulation applied at different nodes along the somatosensory neuraxis. Sensitivity in the cited papers was quantified as the number of intensity levels between the threshold current for detection and the maximum safe stimulus current. Question marks indicate hypothesized sensitivity at sites that have not yet been tested.

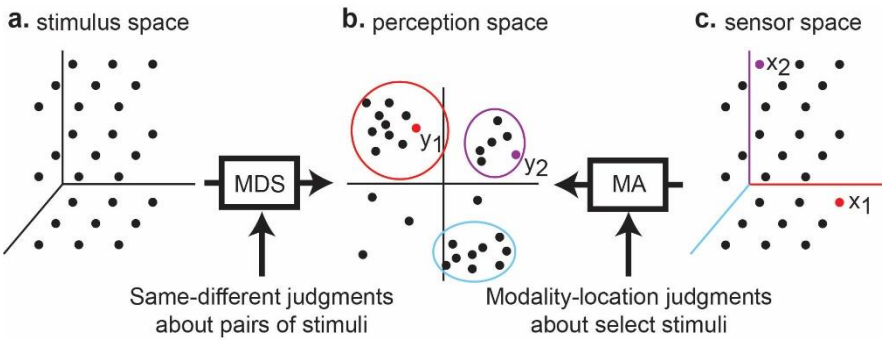

Figure 6.2. LIDES algorithm. Nerve stimuli (**a**) are mapped to a perception space (**b**) through multi-dimensional scaling (MDS) of pairwise same-different judgments. Manifold alignment (MA) is used to map sensor outputs (**c**) to stimuli yielding discriminable percepts.

Bibliography

(2009). One degree of separation: paralysis and spinal cord injury in the United States. Short Hills, NJ, Christopher & Dana Reeve Foundation.

Adrian, E. D. (1941). "Afferent discharges to the cerebral cortex from peripheral sense organs." J Physiol **100**(2): 159-191.

Aguilar, J., C. Rivadulla, C. Soto and A. Canedo (2003). "New corticocuneate cellular mechanisms underlying the modulation of cutaneous ascending transmission in anesthetized cats." J Neurophysiol **89**(6): 3328-3339.

Ai, L. and T. Ro (2014). "The phase of prestimulus alpha oscillations affects tactile perception." J Neurophysiol **111**(6): 1300-1307.

Aivazis, E., K. Siakavara and J. N. Sahalos (2012). Design and analysis of efficient fractal antennas for UHF RFID passive tags. 2012 6th European Conference on Antennas and Propagation (EUCAP).

Andersen, P., S. A. Andersson and T. Lomo (1968). "Thalamo-cortical relations during spontaneous barbiturate spindles." Electroencephalogr Clin Neurophysiol **24**(1): 90.

Anderson, K. D. (2004). "Targeting Recovery: Priorities of the Spinal Cord-Injured Population." Journal of Neurotrauma **21**(10): 1371-1383.

Bengtsson, F., R. Brasselet, R. S. Johansson, A. Arleo and H. Jorntell (2013). "Integration of sensory quanta in cuneate nucleus neurons in vivo." PLoS One **8**(2): e56630.

Bensmaia, S. J. and L. E. Miller (2014). "Restoring sensorimotor function through intracortical interfaces: progress and looming challenges." Nat Rev Neurosci **15**(5): 313-325.

Bentivoglio, M. and A. Rustioni (1986). "Corticospinal neurons with branching axons to the dorsal column nuclei in the monkey." J Comp Neurol **253**(2): 260-276.

Berg, J. A., J. F. Dammann, 3rd, F. V. Tenore, G. A. Tabot, J. L. Boback, L. R. Manfredi, M. L. Peterson, K. D. Katyal, M. S. Johannes, A. Makhlin, R. Wilcox, R. K. Franklin, R. J. Vogelstein, N. G. Hatsopoulos and S. J. Bensmaia (2013). "Behavioral demonstration of a somatosensory neuroprosthesis." IEEE Trans Neural Syst Rehabil Eng **21**(3): 500-507.

Biedenbach, M. A., S. J. Jabbur and A. L. Towe (1971). "Afferent inhibition in the cuneate nucleus of the rhesus monkey." Brain Res **27**(1): 179-183.

Birznieks, I., P. Jenmalm, A. W. Goodwin and R. S. Johansson (2001). "Encoding of direction of fingertip forces by human tactile afferents." Journal of Neuroscience **21**(20): 8222-8237.

Blabe, C. H., V. Gilja, C. A. Chestek, K. V. Shenoy, K. D. Anderson and J. M. Henderson (2015). "Assessment of brain-machine interfaces from the perspective of people with paralysis." J Neural Eng **12**(4): 043002.

Boivie, J. and K. Boman (1981). "Termination of a separate (proprioceptive?) cuneothalamic tract from external cuneate nucleus in monkey." Brain Res **224**(2): 235-246.

Borton, D. A., M. Yin, J. Aceros and A. Nurmikko (2013). "An implantable wireless neural interface for recording cortical circuit dynamics in moving primates." J Neural Eng **10**(2): 026010.

Buford, J. A. and A. G. Davidson (2004). "Movement-related and preparatory activity in the reticulospinal system of the monkey." Exp Brain Res **159**(3): 284-300.

Buzsaki, G. and A. Draguhn (2004). "Neuronal oscillations in cortical networks." Science **304**(5679): 1926-1929.

Buzsaki, G., N. Logothetis and W. Singer (2013). "Scaling brain size, keeping timing: evolutionary preservation of brain rhythms." Neuron **80**(3): 751-764.

Canolty, R. T., K. Ganguly, S. W. Kennerley, C. F. Cadieu, K. Koepsell, J. D. Wallis and J. M. Carmena (2010). "Oscillatory phase coupling coordinates anatomically dispersed functional cell assemblies." Proc Natl Acad Sci U S A **107**(40): 17356-17361.

Caplan, J. B., J. R. Madsen, S. Raghavachari and M. J. Kahana (2001). "Distinct patterns of brain oscillations underlie two basic parameters of human maze learning." J Neurophysiol **86**(1): 368-380.

Chandler, J. E., H. H. Messer and G. Ellender (1994). "Cytotoxicity of Gallium and Indium Ions Compared with Mercuric Ion." Journal of Dental Research **73**(9): 1554-1559.

Chapman, C. E., W. Jiang and Y. Lamarre (1988). "Modulation of lemniscal input during conditioned arm movements in the monkey." Exp Brain Res **72**(2): 316-334.

Cheema, S., A. Rustioni and B. L. Whitsel (1985). "Sensorimotor cortical projections to the primate cuneate nucleus." J Comp Neurol **240**(2): 196-211.

Cheng, S., A. Rydberg, K. Hjort, Z. Wu, B. A. J., A. J. -H., S. Y. G., M. M. A., M. E., K. H. -S., C. W. M., K. D. -H., H. Y. and R. J. A. (2009). "Liquid metal stretchable unbalanced loop antenna." Applied Physics Letters **94**(14): 144103.

Chung, J. E., J. F. Magland, A. H. Barnett, V. M. Tolosa, A. C. Tooker, K. Y. Lee, K. G. Shah, S. H. Felix, L. M. Frank and L. F. Greengard (2017). "A Fully Automated Approach to Spike Sorting." Neuron **95**(6): 1381-1394 e1386.

Collinger, J. L., B. Wodlinger, J. E. Downey, W. Wang, E. C. Tyler-Kabara, D. J. Weber, A. J. McMorland, M. Velliste, M. L. Boninger and A. B. Schwartz (2012). "High-performance neuroprosthetic control by an individual with tetraplegia." Lancet.

Contreras, D., A. Destexhe, T. J. Sejnowski and M. Steriade (1996). "Control of spatiotemporal coherence of a thalamic oscillation by corticothalamic feedback." Science **274**(5288): 771-774.

Contreras, D., A. Destexhe, T. J. Sejnowski and M. Steriade (1997). "Spatiotemporal patterns of spindle oscillations in cortex and thalamus." J Neurosci **17**(3): 1179-1196.

Contreras, D. and M. Steriade (1996). "Spindle oscillation in cats: the role of corticothalamic feedback in a thalamically generated rhythm." J Physiol **490 (Pt 1)**: 159-179.

Corey, D. M., W. P. Dunlap and M. J. Burke (1998). "Averaging correlations: Expected values and bias in combined Pearson rs and Fisher's z transformations." Journal of General Psychology **125**(3): 245-261.

Cunningham, J. P., P. Nuyujukian, V. Gilja, C. A. Chestek, S. I. Ryu and K. V. Shenoy (2011). "A closed-loop human simulator for investigating the role of feedback control in brain-machine interfaces." Journal of Neurophysiology **105**(4): 1932-1949.

Dadarlat, M. C., J. E. O'Doherty and P. N. Sabes (2015). "A learning-based approach to artificial sensory feedback leads to optimal integration." Nat Neurosci **18**(1): 138-144.

Dau-Chyrh, C., Z. Bing-Hao, L. Ji- Chyun, I. Chen, J. Lih-Guong and C. Chung-Chi (2008). A self-complementary Hilbert-curve fractal antenna for UHF RFID tag applications. 2008 IEEE Antennas and Propagation Society International Symposium.

Davceva, N., N. Basheska and J. Balazic (2015). "Diffuse Axonal Injury-A Distinct Clinicopathological Entity in Closed Head Injuries." Am J Forensic Med Pathol **36**(3): 127-133.

Davies, R. M., G. L. Gerstein and S. N. Baker (2006). "Measurement of time-dependent changes in the irregularity of neural spiking." J Neurophysiol **96**(2): 906-918.

Davis, T. S., H. A. Wark, D. T. Hutchinson, D. J. Warren, K. O'Neill, T. Scheinblum, G. A. Clark, R. A. Normann and B. Greger (2016). "Restoring motor control and sensory feedback in people with upper extremity amputations using arrays of 96 microelectrodes implanted in the median and ulnar nerves." J Neural Eng **13**(3): 036001.

Destexhe, A., D. Contreras, T. J. Sejnowski and M. Steriade (1994). "A model of spindle rhythmicity in the isolated thalamic reticular nucleus." J Neurophysiol **72**(2): 803-818.

Destexhe, A., D. Contreras and M. Steriade (1999). "Spatiotemporal analysis of local field potentials and unit discharges in cat cerebral cortex during natural wake and sleep states." J Neurosci **19**(11): 4595-4608.

Dhillon, G. S. and K. W. Horch (2005). "Direct neural sensory feedback and control of a prosthetic arm." IEEE Trans Neural Syst Rehabil Eng **13**(4): 468-472.

Dickey, A. S., A. Suminski, Y. Amit and N. G. Hatsopoulos (2009). "Single-unit stability using chronically implanted multielectrode arrays." J Neurophysiol **102**(2): 1331-1339.

Ethier, C., E. R. Oby, M. J. Bauman and L. E. Miller (2012). "Restoration of grasp following paralysis through brain-controlled stimulation of muscles." Nature **485**(7398): 368-371.

Ferrington, D. G., M. J. Rowe and R. P. Tarvin (1986). "High gain transmission of single impulses through dorsal column nuclei of the cat." Neurosci Lett **65**(3): 277-282.

Fitzsimmons, N. A., W. Drake, T. L. Hanson, M. A. Lebedev and M. A. Nicolelis (2007). "Primate reaching cued by multichannel spatiotemporal cortical microstimulation." J Neurosci **27**(21): 5593-5602.

Flesher, S. N., J. L. Collinger, S. T. Foldes, J. M. Weiss, J. E. Downey, E. C. Tyler-Kabara, S. J. Bensmaia, A. B. Schwartz, M. L. Boninger and R. A. Gaunt (2016). "Intracortical microstimulation of human somatosensory cortex." Science Translational Medicine.

Florence, S. L., J. T. Wall and J. H. Kaas (1989). "Somatotopic organization of inputs from the hand to the spinal gray and cuneate nucleus of monkeys with observations on the cuneate nucleus of humans." J Comp Neurol **286**(1): 48-70.

Fogel, S. M. and C. T. Smith (2011). "The function of the sleep spindle: a physiological index of intelligence and a mechanism for sleep-dependent memory consolidation." Neuroscience & Biobehavioral Reviews **35**(5): 1154-1165.

Fortier-Poisson, P., J.-S. Langlais and A. M. Smith (2015). "Correlation of fingertip shear force direction with somatosensory cortical activity in monkey." Journal of neurophysiology **115**(1): 100-111.

Fraser, G. W. and A. B. Schwartz (2012). "Recording from the same neurons chronically in motor cortex." J Neurophysiol **107**(7): 1970-1978.

Fries, P., P. R. Roelfsema, A. K. Engel, P. Konig and W. Singer (1997). "Synchronization of oscillatory responses in visual cortex correlates with perception in interocular rivalry." Proc Natl Acad Sci U S A **94**(23): 12699-12704.

Fuchs, A. F. and E. S. Luschei (1970). "Firing patterns of abducens neurons of alert monkeys in relationship to horizontal eye movement." J Neurophysiol **33**(3): 382-392.

Ganguly, K. and J. M. Carmena (2009). "Emergence of a stable cortical map for neuroprosthetic control." PLoS Biol **7**(7): e1000153.

Gardner, E. P., H. A. Hamalainen, S. Warren, J. Davis and W. Young (1984). "Somatosensory evoked potentials (SEPs) and cortical single unit responses elicited by

mechanical tactile stimuli in awake monkeys." Electroencephalogr Clin Neurophysiol **58**(6): 537-552.

Gaunt, R. A., J. A. Hokanson and D. J. Weber (2009). "Microstimulation of primary afferent neurons in the L7 dorsal root ganglia using multielectrode arrays in anesthetized cats: thresholds and recruitment properties." J Neural Eng **6**(5): 055009.

Gibney, J. M. and W. S. T. Rowe (2011). An investigation into the Practicality Of Using a stage four Hilbert Curve Fractal Antenna for electronic warfare applications. Asia-Pacific Microwave Conference 2011.

Gilja, V., C. A. Chestek, I. Diester, J. M. Henderson, K. Deisseroth and K. V. Shenoy (2011). "Challenges and opportunities for next-generation intracortically based neural prostheses." IEEE Trans Biomed Eng **58**(7): 1891-1899.

Graczyk, E. L., M. A. Schiefer, H. P. Saal, B. P. Delhaye, S. J. Bensmaia and D. J. Tyler (2016). "The neural basis of perceived intensity in natural and artificial touch." Science Translational Medicine **8**(362): 362ra142-362ra142.

Grenier, F., I. Timofeev and M. Steriade (1998). "Leading role of thalamic over cortical neurons during postinhibitory rebound excitation." Proc Natl Acad Sci U S A **95**(23): 13929-13934.

Haegens, S., B. F. Handel and O. Jensen (2011). "Top-down controlled alpha band activity in somatosensory areas determines behavioral performance in a discrimination task." J Neurosci **31**(14): 5197-5204.

Haegens, S., V. Nacher, R. Luna, R. Romo and O. Jensen (2011). "alpha-Oscillations in the monkey sensorimotor network influence discrimination performance by rhythmical inhibition of neuronal spiking." Proc Natl Acad Sci U S A **108**(48): 19377-19382.

Haegens, S., Y. Vazquez, A. Zainos, M. Alvarez, O. Jensen and R. Romo (2014). "Thalamocortical rhythms during a vibrotactile detection task." Proc Natl Acad Sci U S A **111**(17): E1797-1805.

Hafting, T., M. Fyhn, T. Bonnevie, M. B. Moser and E. I. Moser (2008). "Hippocampus-independent phase precession in entorhinal grid cells." Nature **453**(7199): 1248-1252.

Harris, F., S. J. Jabbur, R. W. Morse and A. L. Towe (1965). "Influence of the cerebral cortex on the cuneate nucleus of the monkey." Nature **208**(5016): 1215-1216.

Hedges, L. V. (1981). "Distribution Theory for Glass's Estimator of Effect Size and Related Estimators." Journal of Educational Statistics **6**(2): 107-128.

Heming, E. A., R. Choo, J. N. Davies and Z. H. Kiss (2011). "Designing a thalamic somatosensory neural prosthesis: consistency and persistence of percepts evoked by electrical stimulation." IEEE Trans Neural Syst Rehabil Eng **19**(5): 477-482.

Hill, D. N., S. B. Mehta and D. Kleinfeld (2011). "Quality metrics to accompany spike sorting of extracellular signals." J Neurosci **31**(24): 8699-8705.

Hochberg, L. R., D. Bacher, B. Jarosiewicz, N. Y. Masse, J. D. Simeral, J. Vogel, S. Haddadin, J. Liu, S. S. Cash, P. van der Smagt and J. P. Donoghue (2012). "Reach and grasp by people with tetraplegia using a neurally controlled robotic arm." Nature **485**(7398): 372-375.

Hoffman, D. S., R. Dubner, R. L. Hayes and T. P. Medlin (1981). "Neuronal activity in medullary dorsal horn of awake monkeys trained in a thermal discrimination task. I. Responses to innocuous and noxious thermal stimuli." J Neurophysiol **46**(3): 409-427.

Hoofnagle, A. N., J. R. Whiteaker, S. A. Carr, E. Kuhn, T. Liu, S. A. Massoni, S. N. Thomas, R. R. Townsend, L. J. Zimmerman, E. Boja, J. Chen, D. L. Crimmins, S. R.

Davies, Y. Gao, T. R. Hiltke, K. A. Ketchum, C. R. Kinsinger, M. Mesri, M. R. Meyer, W. J. Qian, R. M. Schoenherr, M. G. Scott, T. Shi, G. R. Whiteley, J. A. Wrobel, C. Wu, B. L. Ackermann, R. Aebersold, D. R. Barnidge, D. M. Bunk, N. Clarke, J. B. Fishman, R. P. Grant, U. Kusebauch, M. M. Kushnir, M. S. Lowenthal, R. L. Moritz, H. Neubert, S. D. Patterson, A. L. Rockwood, J. Rogers, R. J. Singh, J. E. Van Eyk, S. H. Wong, S. Zhang, D. W. Chan, X. Chen, M. J. Ellis, D. C. Liebler, K. D. Rodland, H. Rodriguez, R. D. Smith, Z. Zhang, H. Zhang and A. G. Paulovich (2016). "Recommendations for the Generation, Quantification, Storage, and Handling of Peptides Used for Mass Spectrometry-Based Assays." Clin Chem **62**(1): 48-69.

Hsiang-Tung, C. (1950). "The repetitive discharges of corticothalamic reverberating circuit." J Neurophysiol **13**(3): 235-257.

Huang, Y., Y. Wang, L. Xiao, H. Liu, W. Dong and Z. Yin (2014). "Microfluidic serpentine antennas with designed mechanical tunability." Lab on a Chip **14**(21): 4205-4212.

Hummelsheim, H. and M. Wiesendanger (1985). "Neuronal responses of medullary relay cells to controlled stretches of forearm muscles in the monkey." Neuroscience **16**(4): 989-996.

Jang, S. H. and H. D. Lee (2017). "Traumatic axonal injury despite clinical phenotype of mild traumatic brain injury: a case report." Brain Inj **31**(11): 1534-1537.

Jensen, O. and A. Mazaheri (2010). "Shaping functional architecture by oscillatory alpha activity: gating by inhibition." Front Hum Neurosci **4**: 186.

Johansson, R. S. and J. R. Flanagan (2009). "Coding and use of tactile signals from the fingertips in object manipulation tasks." Nat Rev Neurosci **10**(5): 345-359.

Johnson, L. A., J. D. Wander, D. Sarma, D. K. Su, E. E. Fetz and J. G. Ojemann (2013). "Direct electrical stimulation of the somatosensory cortex in humans using electrocorticography electrodes: a qualitative and quantitative report." J Neural Eng **10**(3): 036021.

Jones, S. J., T. Allison, G. McCarthy and C. C. Wood (1992). "Tactile interference differentiates sub-components of N20, P20 and P29 in the human cortical surface somatosensory evoked potential." Electroencephalogr Clin Neurophysiol **82**(2): 125-132.

Jorntell, H., F. Bengtsson, P. Geborek, A. Spanne, A. V. Terekhov and V. Hayward (2014). "Segregation of tactile input features in neurons of the cuneate nucleus." Neuron **83**(6): 1444-1452.

Ju-Hee, S., T. Jacob, Q. Amit, H. G. J., L. Gianluca and D. M. D. (2009). "Reversibly Deformable and Mechanically Tunable Fluidic Antennas." Advanced Functional Materials **19**(22): 3632-3637.

Kageyama, Y., M. Hirata, T. Yanagisawa, T. Shimokawa, J. Sawada, S. Morris, N. Mizushima, H. Kishima, O. Sakura and T. Yoshimine (2014). "Severely affected ALS patients have broad and high expectations for brain-machine interfaces." Amyotrophic Lateral Sclerosis and Frontotemporal Degeneration **15**(7-8): 513-519.

Kim, S., T. Callier, G. A. Tabot, R. A. Gaunt, F. V. Tenore and S. J. Bensmaia (2015). "Behavioral assessment of sensitivity to intracortical microstimulation of primate somatosensory cortex." Proc Natl Acad Sci U S A **112**(49): 15202-15207.

Klaes, C., Y. Shi, S. Kellis, J. Minxha, B. Revechkis and R. A. Andersen (2014). "A cognitive neuroprosthetic that uses cortical stimulation for somatosensory feedback." J Neural Eng **11**(5): 056024.

Koralek, A. C., X. Jin, J. D. Long, 2nd, R. M. Costa and J. M. Carmena (2012). "Corticostriatal plasticity is necessary for learning intentional neuroprosthetic skills." Nature **483**(7389): 331-335.

Kreiman, G., C. P. Hung, A. Kraskov, R. Q. Quiroga, T. Poggio and J. J. DiCarlo (2006). "Object selectivity of local field potentials and spikes in the macaque inferior temporal cortex." Neuron **49**(3): 433-445.

Kulics, A. T. and L. J. Cauller (1986). "Cerebral cortical somatosensory evoked responses, multiple unit activity and current source-densities: their interrelationships and significance to somatic sensation as revealed by stimulation of the awake monkey's hand." Exp Brain Res **62**(1): 46-60.

Laventure, S., S. Fogel, O. Lungu, G. Albouy, P. Sévigny-Dupont, C. Vien, C. Sayour, J. Carrier, H. Benali and J. Doyon (2016). "NREM2 and sleep spindles are instrumental to the consolidation of motor sequence memories." PLoS biology **14**(3): e1002429.

Lea-Carnall, C. A., M. A. Montemurro, N. J. Trujillo-Barreto, L. M. Parkes and W. El-Deredy (2016). "Cortical Resonance Frequencies Emerge from Network Size and Connectivity." PLoS Comput Biol **12**(2): e1004740.

Leiras, R., P. Velo, F. Martin-Cora and A. Canedo (2010). "Processing afferent proprioceptive information at the main cuneate nucleus of anesthetized cats." J Neurosci **30**(46): 15383-15399.

Leong, Y. P. and J. C. Doyle (2017). "Effects of Delays, Poles, and Zeros on Time Domain Waterbed Tradeoffs and Oscillations." IEEE Control Systems Letters **1**(1): 122-127.

Li, K., J. Patel, G. Purushothaman, R. T. Marion and V. A. Casagrande (2013). "Retinotopic maps in the pulvinar of bush baby (Otolemur garnettii)." J Comp Neurol **521**(15): 3432-3450.

Li, P. H., J. L. Gauthier, M. Schiff, A. Sher, D. Ahn, G. D. Field, M. Greschner, E. M. Callaway, A. M. Litke and E. J. Chichilnisky (2015). "Anatomical identification of extracellularly recorded cells in large-scale multielectrode recordings." J Neurosci **35**(11): 4663-4675.

Litke, A. M., N. Bezayiff, E. J. Chichilnisky, W. Cunningham, W. Dabrowski, A. A. Grillo, M. Grivich, P. Grybos, P. Hottowy, S. Kachiguine, R. S. Kalmar, K. Mathieson, D. Petrusca, A. Rahman and A. Sher (2004). "What does the eye tell the brain?: Development of a system for the large-scale recording of retinal output activity." IEEE Transactions on Nuclear Science **51**(4): 1434-1440.

Liu, X., M. Zhang, B. Subei, A. G. Richardson, T. H. Lucas and J. Van der Spiegel (2015). "The PennBMBI: Design of a General Purpose Wireless Brain-Machine-Brain Interface System." IEEE Trans Biomed Circuits Syst **9**(2): 248-258.

London, B. M., L. R. Jordan, C. R. Jackson and L. E. Miller (2008). "Electrical stimulation of the proprioceptive cortex (area 3a) used to instruct a behaving monkey." IEEE Trans Neural Syst Rehabil Eng **16**(1): 32-36.

Macmillan, N. and D. C Creelman (2004). Detection Theory: A User's Guide.

Masahiro, K., L. Xiaofeng, K. Choongik, H. Michinao, W. B. J., H. Donhee and W. G. M. (2010). "Stretchable Microfluidic Radiofrequency Antennas." Advanced Materials **22**(25): 2749-2752.

McVay, J., A. Hoorfar and N. Engheta (2006). Space-filling curve RFID tags. 2006 IEEE Radio and Wireless Symposium.

Miranda, R. A., W. D. Casebeer, A. M. Hein, J. W. Judy, E. P. Krotkov, T. L. Laabs, J. E. Manzo, K. G. Pankratz, G. A. Pratt, J. C. Sanchez, D. J. Weber, T. L. Wheeler and G. S. Ling (2015). "DARPA-funded efforts in the development of novel brain-computer interface technologies." J Neurosci Methods **244**: 52-67.

Moller, A. R., T. Sekiya and C. N. Sen (1989). "Responses from dorsal column nuclei (DCN) in the monkey to stimulation of upper and lower limbs and spinal cord." Electroencephalogr Clin Neurophysiol **73**(4): 353-361.

Monzée, J., Y. Lamarre and A. M. Smith (2003). "The Effects of Digital Anesthesia on Force Control Using a Precision Grip." Journal of Neurophysiology **89**(2): 672-683.

Moritz, C. T., S. I. Perlmutter and E. E. Fetz (2008). "Direct control of paralysed muscles by cortical neurons." Nature **456**(7222): 639-642.

Murad, N. A., M. Esa, M. F. M. Yusoff and S. H. A. Ali (2006). Hilbert Curve Fractal Antenna for RFID Application. 2006 International RF and Microwave Conference.

Niu, J., L. Ding, J. J. Li, H. Kim, J. Liu, H. Li, A. Moberly, T. C. Badea, I. D. Duncan, Y. J. Son, S. S. Scherer and W. Luo (2013). "Modality-based organization of ascending somatosensory axons in the direct dorsal column pathway." J Neurosci **33**(45): 17691-17709.

Nunez, A. and W. Buno (1999). "In vitro electrophysiological properties of rat dorsal column nuclei neurons." Eur J Neurosci **11**(6): 1865-1876.

Nunez, A., F. Panetsos and C. Avendano (2000). "Rhythmic neuronal interactions and synchronization in the rat dorsal column nuclei." Neuroscience **100**(3): 599-609.

O'Doherty, J. E., M. A. Lebedev, T. L. Hanson, N. A. Fitzsimmons and M. A. Nicolelis (2009). "A brain-machine interface instructed by direct intracortical microstimulation." Front Integr Neurosci **3**: 20.

O'Doherty, J. E., M. A. Lebedev, P. J. Ifft, K. Z. Zhuang, S. Shokur, H. Bleuler and M. A. Nicolelis (2011). "Active tactile exploration using a brain-machine-brain interface." Nature **479**(7372): 228-231.

O'Doherty, J. E., M. A. Lebedev, Z. Li and M. A. Nicolelis (2012). "Virtual active touch using randomly patterned intracortical microstimulation." IEEE Trans Neural Syst Rehabil Eng **20**(1): 85-93.

O'Keefe, J. and M. L. Recce (1993). "Phase relationship between hippocampal place units and the EEG theta rhythm." Hippocampus **3**(3): 317-330.

Panetsos, F., A. Nunez and C. Avendano (1998). "Sensory information processing in the dorsal column nuclei by neuronal oscillators." Neuroscience **84**(3): 635-639.

Park, S. I., D. S. Brenner, G. Shin, C. D. Morgan, B. A. Copits, H. U. Chung, M. Y. Pullen, K. N. Noh, S. Davidson, S. J. Oh, J. Yoon, K. I. Jang, V. K. Samineni, M. Norman, J. G. Grajales-Reyes, S. K. Vogt, S. S. Sundaram, K. M. Wilson, J. S. Ha, R. Xu, T. Pan, T. I. Kim, Y. Huang, M. C. Montana, J. P. Golden, M. R. Bruchas, R. W. t. Gereau and J. A. Rogers (2015). "Soft, stretchable, fully implantable miniaturized optoelectronic systems for wireless optogenetics." Nat Biotechnol **33**(12): 1280-1286.

Peterson, N. N., C. E. Schroeder and J. C. Arezzo (1995). "Neural generators of early cortical somatosensory evoked potentials in the awake monkey." Electroencephalogr Clin Neurophysiol **96**(3): 248-260.

Poggio, G. F. and V. B. Mountcastle (1963). "THE FUNCTIONAL PROPERTIES OF VENTROBASAL THALAMIC NEURONSSTUDIED IN UNANESTHETIZED MONKEYS." J Neurophysiol **26**: 775-806.

Purdon, P. L., A. Sampson, K. J. Pavone and E. N. Brown (2015). "Clinical Electroencephalography for Anesthesiologists: Part I: Background and Basic Signatures." Anesthesiology **123**(4): 937-960.

Qi, H. X. and J. H. Kaas (2006). "Organization of primary afferent projections to the gracile nucleus of the dorsal column system of primates." J Comp Neurol **499**(2): 183-217.

Radunovic, A., D. Annane, M. K. Rafiq and N. Mustfa (2013). Cochrane Database Syst Rev **3**(null): null.

Raspopovic, S., M. Capogrosso, F. M. Petrini, M. Bonizzato, J. Rigosa, G. Di Pino, J. Carpaneto, M. Controzzi, T. Boretius, E. Fernandez, G. Granata, C. M. Oddo, L. Citi, A. L. Ciancio, C. Cipriani, M. C. Carrozza, W. Jensen, E. Guglielmelli, T. Stieglitz, P. M. Rossini and S. Micera (2014). "Restoring Natural Sensory Feedback in Real-Time Bidirectional Hand Prostheses." Science Translational Medicine **6**(222): 222ra219-222ra219.

Reboreda, A., E. Sanchez, M. Romero and J. A. Lamas (2003). "Intrinsic spontaneous activity and subthreshold oscillations in neurones of the rat dorsal column nuclei in culture." J Physiol **551**(Pt 1): 191-205.

Richardson, A. G., M. A. Attiah, J. I. Berman, H. I. Chen, X. Liu, M. Zhang, J. Van der Spiegel and T. H. Lucas (2015). "The effects of acute cortical somatosensory deafferentation on grip force control." Cortex **74**: 1-8.

Richardson, A. G., T. Borghi and E. Bizzi (2012). "Activity of the same motor cortex neurons during repeated experience with perturbed movement dynamics." J Neurophysiol **107**(11): 3144-3154.

Richardson, A. G., P. K. Weigand, S. Y. Sritharan and T. H. Lucas (2014). A chronic neural interface to the macaque dorsal column nuclei. Society for Neuroscience Annual Meeting. Washington, DC. **339.09:** 339.309.

Richardson, A. G., P. K. Weigand, S. Y. Sritharan and T. H. Lucas (2014). A chronic neural interface to the macaque dorsal column nuclei. Program No. 339.09. 2014 Neuroscience Meeting Planner, Washington, DC, Society for Neuroscience.

Richardson, A. G., P. K. Weigand, S. Y. Sritharan and T. H. Lucas (2015). Somatosensory encoding with cuneate nucleus microstimulation: effects on downstream cortical activity. 7th International IEEE/EMBS Conference on Neural Engineering (NER), Montpellier, France, IEEE.

Richardson, A. G., P. K. Weigand, S. Y. Sritharan and T. H. Lucas (2016). "A chronic neural interface to the macaque dorsal column nuclei." J Neurophysiol.

Rogers, J. A. and Y. Huang (2009). "A curvy, stretchy future for electronics." Proceedings of the National Academy of Sciences **106**(27): 10875-10876.

Romo, R., A. Hernandez, A. Zainos and E. Salinas (1998). "Somatosensory discrimination based on cortical microstimulation." Nature **392**(6674): 387-390.

Rothwell, J. C., M. M. Traub, B. L. Day, J. A. Obeso, P. K. Thomas and C. D. Marsden (1982). "Manual motor performance in a deafferented man." Brain **105 (Pt 3)**: 515-542.

Rousche, P. J. and R. A. Normann (1998). "Chronic recording capability of the Utah Intracortical Electrode Array in cat sensory cortex." J Neurosci Methods **82**(1): 1-15.

Sagen, H. (1994). Space-Filling Curves. New York, Springer New York.

Salcman, M. and M. J. Bak (1973). "Design, fabrication, and in vivo behavior of chronic recording intracortical microelectrodes." IEEE Trans Biomed Eng **20**(4): 253-260.

Sanchez, E., A. Reboreda, M. Romero and J. A. Lamas (2006). "Spontaneous bursting and rhythmic activity in the cuneate nucleus of anaesthetized rats." Neuroscience **141**(1): 487-500.

Santhanam, G., S. I. Ryu, B. M. Yu, A. Afshar and K. V. Shenoy (2006). "A high-performance brain-computer interface." Nature **442**(7099): 195-198.

Sarlegna, F. R., N. Malfait, L. Bringoux, C. Bourdin and J. L. Vercher (2010). "Force-field adaptation without proprioception: can vision be used to model limb dynamics?" Neuropsychologia **48**(1): 60-67.

Serruya, M. D., N. G. Hatsopoulos, L. Paninski, M. R. Fellows and J. P. Donoghue (2002). "Instant neural control of a movement signal." Nature **416**(6877): 141-142.

Shanechi, M. M., A. L. Orsborn, H. G. Moorman, S. Gowda, S. Dangi and J. M. Carmena (2017). "Rapid control and feedback rates enhance neuroprosthetic control." Nature Communications **8**: 13825.

Shaw, A. D., N. Saxena, E. J. L, J. E. Hall, K. D. Singh and S. D. Muthukumaraswamy (2015). "Ketamine amplifies induced gamma frequency oscillations in the human cerebral cortex." Eur Neuropsychopharmacol **25**(8): 1136-1146.

Shi, Y., M. Manco, D. Moyal, G. Huppert, H. Araki, A. Banks, H. Joshi, R. McKenzie, A. Seewald, G. Griffin, E. Sen-Gupta, D. Wright, P. Bastien, F. Valceschini, S. Seite, J. A. Wright, R. Ghaffari, J. Rogers, G. Balooch and R. M. Pielak (2018). "Soft, stretchable,

epidermal sensor with integrated electronics and photochemistry for measuring personal UV exposures." PLoS One **13**(1): e0190233.

Singer, W. (2017). "Neuronal oscillations: unavoidable and useful?" Eur J Neurosci.

Song, W. and M. Semework (2015). "Tactile representation in somatosensory thalamus (VPL) and cortex (S1) of awake primate and the plasticity induced by VPL neuroprosthetic stimulation." Brain Res **1625**: 301-313.

Steriade, M. (1999). "Coherent oscillations and short-term plasticity in corticothalamic networks." Trends Neurosci **22**(8): 337-345.

Steriade, M., P. Gloor, R. R. Llinas, F. H. Lopes de Silva and M. M. Mesulam (1990). "Report of IFCN Committee on Basic Mechanisms. Basic mechanisms of cerebral rhythmic activities." Electroencephalogr Clin Neurophysiol **76**(6): 481-508.

Streit, W. J., Q. S. Xue, A. Prasad, V. Sankar, E. Knott, A. Dyer, J. R. Reynolds, T. Nishida, G. P. Shaw and J. C. Sanchez (2012). "Electrode Failure: Tissue, Electrical, and Material Responses." IEEE Pulse **3**(1): 30-33.

Swadlow, H. A. (2003). "Fast-spike interneurons and feedforward inhibition in awake sensory neocortex." Cereb Cortex **13**(1): 25-32.

Swadlow, H. A. and A. G. Gusev (2000). "The influence of single VB thalamocortical impulses on barrel columns of rabbit somatosensory cortex." J Neurophysiol **83**(5): 2802-2813.

Tabot, G. A., J. F. Dammann, J. A. Berg, F. V. Tenore, J. L. Boback, R. J. Vogelstein and S. J. Bensmaia (2013). "Restoring the sense of touch with a prosthetic hand through a brain interface." Proc Natl Acad Sci U S A **110**(45): 18279-18284.

Tan, D. W., M. A. Schiefer, M. W. Keith, J. R. Anderson, J. Tyler and D. J. Tyler (2014). "A neural interface provides long-term stable natural touch perception." Sci Transl Med **6**(257): 257ra138.

Thakor, N. V., M. S. Fifer, G. Hotson, H. L. Benz, G. I. Newman, G. W. Milsap and N. E. Crone (2014). "Neuroprosthetic limb control with electrocorticography: Approaches and challenges." Conf Proc IEEE Eng Med Biol Soc **2014**: 5212-5215.

Timofeev, I., D. Contreras and M. Steriade (1996). "Synaptic responsiveness of cortical and thalamic neurones during various phases of slow sleep oscillation in cat." J Physiol **494 (Pt 1)**: 265-278.

Tokimura, H., V. Di Lazzaro, Y. Tokimura, A. Oliviero, P. Profice, A. Insola, P. Mazzone, P. Tonali and J. C. Rothwell (2000). "Short latency inhibition of human hand motor cortex by somatosensory input from the hand." J Physiol **523 Pt 2**: 503-513.

Tomassini, A. and A. D'Ausilio (2018). "Passive sensorimotor stimulation triggers long lasting alpha-band fluctuations in visual perception." J Neurophysiol **119**(2): 380-388.

Velliste, M., S. Perel, M. C. Spalding, A. S. Whitford and A. B. Schwartz (2008). "Cortical control of a prosthetic arm for self-feeding." Nature **453**(7198): 1098-1101.

Vergara, I. A., T. Norambuena, E. Ferrada, A. W. Slater and F. Melo (2008). "StAR: a simple tool for the statistical comparison of ROC curves." BMC Bioinformatics **9**: 265.

W., B. (2001). "Biocompatibility of Dental Alloys." Advanced Engineering Materials **3**(10): 753-761.

Wang, S., Y. Huang and J. A. Rogers (2015). "Mechanical Designs for Inorganic Stretchable Circuits in Soft Electronics." IEEE Trans Compon Packaging Manuf Technol **5**(9): 1201-1218.

Weber, D. J., R. Friesen and L. E. Miller (2012). "Interfacing the somatosensory system to restore touch and proprioception: essential considerations." J Mot Behav **44**(6): 403-418.

Wettels, N., V. J. Santos, R. S. Johansson and G. E. Loeb (2008). "Biomimetic tactile sensor array." Advanced Robotics **22**(8): 829-849.

Witham, C. L. and S. N. Baker (2011). "Modulation and transmission of peripheral inputs in monkey cuneate and external cuneate nuclei." J Neurophysiol **106**(5): 2764-2775.

Xu, J. and J. T. Wall (1999). "Functional organization of tactile inputs from the hand in the cuneate nucleus and its relationship to organization in the somatosensory cortex." J Comp Neurol **411**(3): 369-389.

Zaaimi, B., R. Ruiz-Torres, S. A. Solla and L. E. Miller (2013). "Multi-electrode stimulation in somatosensory cortex increases probability of detection." J Neural Eng **10**(5): 056013.